The Science and Function of Nanomaterials: From Synthesis to Application

In The Science and Function of Nanomaterials: From Synthesis to Application; Harper-Leatherman, et al.;

ACS SYMPOSIUM SERIES **1183**

The Science and Function of Nanomaterials: From Synthesis to Application

Amanda S. Harper-Leatherman, Editor
Fairfield University
Fairfield, Connecticut

Camille M. Solbrig, Editor
Southern Connecticut State University
New Haven, Connecticut

American Chemical Society, Washington, DC

Distributed in print by Oxford University Press

Library of Congress Cataloging-in-Publication Data

The science and function of nanomaterials : from synthesis to application / Amanda S. Harper-Leatherman, editor, Fairfield University, Fairfield, Connecticut, Camille M. Solbrig, editor, Southern Connecticut State University, New Haven, Connecticut.
pages cm. -- (ACS symposium series ; 1183)
Includes bibliographical references and index.
ISBN 978-0-8412-3016-3 (alk. paper)
1. Nanostructured materials. 2. Carbon nanotubes. I. Harper-Leatherman, Amanda S., editor. II. Solbrig, Camille M., editor.
TA418.9.N35S3515 2014
620.1′15--dc23
2014041945

The paper used in this publication meets the minimum requirements of American National Standard for Information Sciences—Permanence of Paper for Printed Library Materials, ANSI Z39.48n1984.

Distributed in print by Oxford University Press

PRINTED IN THE UNITED STATES OF AMERICA

Foreword

The ACS Symposium Series was first published in 1974 to provide a mechanism for publishing symposia quickly in book form. The purpose of the series is to publish timely, comprehensive books developed from the ACS sponsored symposia based on current scientific research. Occasionally, books are developed from symposia sponsored by other organizations when the topic is of keen interest to the chemistry audience.

Before agreeing to publish a book, the proposed table of contents is reviewed for appropriate and comprehensive coverage and for interest to the audience. Some papers may be excluded to better focus the book; others may be added to provide comprehensiveness. When appropriate, overview or introductory chapters are added. Drafts of chapters are peer-reviewed prior to final acceptance or rejection, and manuscripts are prepared in camera-ready format.

As a rule, only original research papers and original review papers are included in the volumes. Verbatim reproductions of previous published papers are not accepted.

ACS Books Department

Preface

Nanoscience and nanotechnology have functioned as effective "buzzwords" for at least a decade due to the unique properties that materials possess on the nanometer scale. The interest in nanoscience and nanotechnology is so great and so widespread that these topics are even being introduced at the K-12 level in some school districts. Nanoscience and nanotechnology have already improved many applications and have the potential to continue to do so, making it important for all types of scientists to stay up-to-date on research related to nanomaterials. Due to the power, popularity and promise of nanoscience and nanotechnology, a symposium on these topics was included in the 2013 Northeast Regional Meeting of the American Chemical Society (NERM) with the idea of bringing together researchers in the broad areas of nanotechnology and nanoscience that were also located in the Northeastern region of the United States.

The Nanoscience Symposium held at NERM 2013 consisted of three sessions on nanoscience research entitled, Biology, Carbon and Catalytically Relevant Materials, and Properties and Applications of Non-Carbon Materials. These sessions were well attended and received, and featured a great variety of presenters representing institutions located in the Northeast USA, although international scholars and those from across the USA were also represented. Titles of papers from the symposium indicated that scientists are working on a broad range of nanoscience topics representing many disciplines. While the symposium was organized in sessions based on type of material studied, we organized the chapters in this book into two sections, one on synthetic studies of nanomaterials and one on applications of nanomaterials. In one book, we cannot possibly present a comprehensive overview of ongoing research in all areas. In addition, unfortunately not all symposium speakers were able to contribute to this symposium series volume. However, this book does include many symposium speakers as well as some researchers from the Northeast USA invited to contribute chapters. The chapters present a sampling of fundamental research and application-based research. We are hopeful that those entering the field can use this book to get an overview of some current research going on in these two main research areas in the nanoscience field.

In the first section of this book, a variety of synthetic methods used to make or functionalize nanomaterials are presented with work related to mesoporous materials, semiconductor nanowires, graphene, and carbon nanotubes included. Weinberger et al. present a new method for creating ordered mesoporous carbon (OMC) from a fructose precursor simplifying the standard process for making OMC. Munden and Reed outline the chemical beam epitaxy technique for growing gallium nitride nanowires with precisely controlled nanowire electronic

In The Science and Function of Nanomaterials: From Synthesis to Application; Harper-Leatherman, et al.;

properties. Whitener reviews the reversible reactivity of graphene from oxidation and hydrogenation reactions to Diels-Alder reactivity. Finally, Hemraj-Benny reviews recent research on functionalizing single-walled carbon nanotube surfaces with metal nanoparticles resulting in composite nanomaterials with enhanced properties compared to each individual nanomaterial. While all of these nanomaterials have applicability, the main focus of these chapters is on the details of the synthetic procedures and techniques used to make the nanomaterials.

The second section of the book presents accounts of using nanotechnology and nanoscience in a variety of ways. Interestingly, most of these chapters represent the current state of nanoscience research in that many are by authors from fields outside of the materials field, such as art conservation science or separation science, who are using nanoscience to move these other fields forward. Belz et al. are an interdisciplinary group of authors from multiple institutions with ties to both medicine and physics who comprehensively review the many types of nanoparticle-based formulations that can be used to improve radiation cancer therapy. Chen and Whitmore from the Institute for the Preservation of Cultural Heritage at Yale University review their work on studying silver nanoparticle-based sensors for the detection of hydrogen sulfide gas with applications in art conservation. He, Lin, and Zou outline the work they did to synthesis and characterize calcium carbonate particles with antibacterial properties for use as fillers in plastics. Finally, Freyer and Savage report the effects of various synthetic variations on producing electrospun nanofiber mats that were also evaluated for use as a stationary phase for thin layer chromatography.

Overall, this book presents a snapshot of research covering synthetic studies of nanomaterials to applications of nanomaterials. We hope that students and those entering the field will learn from the range of studies presented in this book and will be inspired by the many possible applications of nanomaterials. We are grateful to the authors for contributing chapters and to the numerous reviewers who carefully read and commented on the chapters of this book to help improve the quality. We would also like to very gratefully acknowledge the wonderful help and support from the staff at the ACS Books Editorial Office, especially Tim Marney and Chloe Tuck.

Amanda S. Harper-Leatherman
Associate Professor
Chemistry & Biochemistry Department
Fairfield University
1073 North Benson Road, Bannow 306
Fairfield, Connecticut 06824, United States

Camille M. Solbrig
Assistant Professor
Chemistry Department
Southern Connecticut State University
434A Jennings Hall
New Haven, Connecticut 06515, United States

Editors' Biographies

Amanda S. Harper-Leatherman

Amanda S. Harper-Leatherman received her bachelor's degree in Chemistry from St. Olaf College in Northfield, MN and her Ph.D. in Analytical Chemistry from the University of North Carolina at Chapel Hill. In graduate school she was involved in research studying the size-dependent electrochemical and spectroscopic properties of gold nanoparticles. After a post-doctoral position at the Naval Research Laboratory in Washington, DC, she joined the faculty of Fairfield University in 2006 as an Assistant Professor. She was promoted to Associate Professor and awarded tenure in 2013. Her current research involves studying protein interactions with nanomaterials and highly porous aerogels.

Camille M. Solbrig

Camille M. Solbrig's interest in nanoscience and surface chemistry originated from her summer research experiences at IBM's central research facility in Yorktown Heights, NY while still an undergraduate in chemistry at Penn State. Training in SEM and X-ray analysis followed, leading to a MS in Textile Science and a Ph.D. in Polymer Science elucidating polymer surface chemistry from Cornell. She then held industrial positions in research and development around the USA, before an interest in the intersection of biotechnology and polymeric materials led to research in degradable electro-spun scaffolding for tissue engineering and polymeric nanoparticles at Yale University. Her latest challenge has been teaching undergraduate chemistry at Southern Connecticut State University in New Haven, CT.

In The Science and Function of Nanomaterials: From Synthesis to Application; Harper-Leatherman, et al.;

Chapter 1

Fructose as a Precursor for Mesoporous Carbon: Straightforward Solvent-Free Synthesis by Nanocasting

C. Weinberger, S. Haffer, T. Wagner, and M. Tiemann*

Faculty of Science, Department of Chemistry, University of Paderborn, Warburger Str. 100, D-33098 Paderborn, Germany
***E-mail: michael.tiemann@upb.de**

Due to their unique properties, ordered mesoporous carbon (OMC) materials prepared by nanocasting have raised great attention in recent years. Their synthesis usually comprises multiple cycles of impregnating a porous structure matrix with an aqueous solution of a suitable precursor, such as sucrose or other, often hazardous, compound. We present a more straightforward variation of this method by using fructose as the precursor compound. By using a solvent-free melt of the precursor, the impregnation requires only a single step. After carbonization by thermal decomposition and removal of the mesoporous silica structure matrix (SBA-15), ordered mesoporous carbon with one (CMK-3) or two (CMK-5) pore modes in two-dimensional, hexagonal symmetry (p6*mm*) is obtained.

In The Science and Function of Nanomaterials: From Synthesis to Application; Harper-Leatherman, et al.;

Introduction

Ordered mesoporous carbon (OMC) materials have raised great attention due to their unique properties such as a large surface area up to 2500 $m^2\ g^{-1}$ and large pore volumes up to about 2 mL g^{-1} (*1*). Their unique properties make them desirable as adsorbents (*2*, *3*), catalysts/catalyst supports (*4–6*), gas storage systems (*7*, *8*), electrode materials (*9–12*), electrochemical sensors (*13*) and drug delivery systems (*14*, *15*). In addition, OMC materials can be used as structure matrices for the synthesis of other mesoporous materials by nanocasting (*16–27*), as summarized in recent review articles (*28–31*).

In general, the synthesis of OMC materials relies on two different synthesis approaches, namely direct "soft templating (*32–37*)" or structure replication (nanocasting) which uses ordered mesoporous silica materials as matrices (*38–43*). The pores of the matrix are filled with a precursor compound which is subsequently carbonized. To fill the pores with a sufficient amount of the precursor and, hence, to retain the structure after removal of the matrix, usually two or more consecutive cycles of impregnation/carbonization are necessary (*39*). To avoid several impregnation steps, toxic precursors like furfuryl alcohol are sometimes used (*1*, *44*). Alternatively, propylene (*45*, *46*), CH_4 (*47*) or styrene (*48*) can be used for an infiltration by more elaborate chemical vapour deposition (CVD) techniques. To overcome the disadvantages of repeated impregnation cycles, toxic precursors, or advanced set-up, solvent-free melts of precursors can be used to efficiently fill the pores of the structure matrix. This has been proven to be an economical way of increasing the loading of the structure matrix in a single impregnation cycle for the synthesis of ordered mesoporous metal oxides (*23*, *49–53*) and, very recently, for carbon (*54*, *55*).

The basic principle of the structure replication by nanocasting is depicted in Figure 1. The pores of an ordered mesoporous silica (SBA-15) with a two-dimensional hexagonal p6*mm* symmetry, can be infiltrated with the precursor by different techniques (*30*). By conversion of the precursor, a composite material consisting of silica and carbon is obtained (CMK-3@SBA-15). If an insufficient amount of precursor is used to fill the pores completely, only the pore walls of the SBA-15 silica matrix are covered with carbon (CMK-5@SBA-15) (*1*). The silica matrix can be selectively removed by etching with hydrofluoric acid or alkali hydroxides (*38*, *39*, *56*). Depending on the volume fraction of carbon within the silica matrix, it is possible to synthesize two-dimensional ordered arrays of carbon rods (CMK-3 (*39*)) or hollow carbon tubes (CMK-5 (*6*)), respectively, both with hexagonal p6*mm* symmetry, corresponding to the SBA-15 silica pore system symmetry. CMK-3 carbon exhibits slit-like mesopores (the voids between the carbon rods), while CMK-5 contains two distinct pore systems: in addition to the inter-tubular slit-like pores, the carbon rods are hollow, constituting a second, intra-tubular pore mode. The size of the inter-tubular pores depends on the choice of the silica host (SBA-15), whereas the intra-tubular pore size depends on the amount of precursor used (*1*).

Apart from the mesopores that result from the structure replication process, the carbon materials also exhibit microporosity which originates from the decomposition (carbonization) of the precursor. Depending on the synthesis

conditions and the type of precursor, the micropores may contribute a lot to the total Brunaer-Emmet-Teller (BET) surface area (*57*, *58*).

Here we present the utilization of fructose as a precursor for the nanocasting synthesis of ordered mesoporous carbon materials. The choice of fructose offers the advantage of a substantially improved efficiency of infiltrating the precursor into the pores of the silica matrix. This is because fructose, unlike most other simple sugars, easily melts without premature decomposition, facilitating a solvent-free infiltration procedure. Consequently, only a single step of impregnation and subsequent carbonization is necessary to sufficiently fill the pores of the silica matrix. Through variation of the precursor amount it is possible to synthesize both CMK-3- and CMK-5-type carbon.

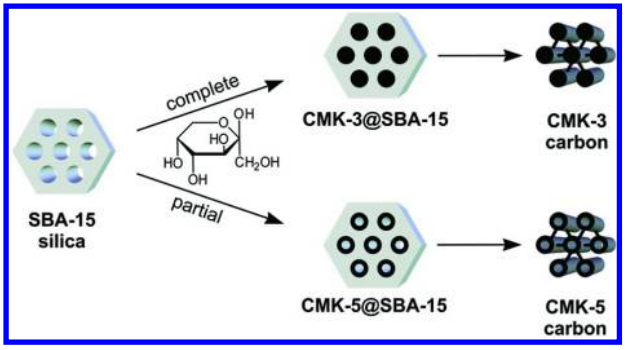

Figure 1. Schematic illustration of the nanocasting procedure for the synthesis of CMK-3 (39) and CMK-5 (6) carbon.

Experimental Section

Ordered mesoporous SBA-15 silica was utilized as template matrix for the synthesis of CMK-3 and CMK-5 carbon. In a typical synthesis (*59*) triblock copolymer Pluronic P-123 (M_n~5800, Sigma-Aldrich) was dissolved at 308 K in a mixture of deionized water (480 mL) and hydrochloric acid (24.0 mL, 35 %, Stockmeier). After addition of tetraethyl orthosilicate (TEOS, 37.0 mL, Sigma-Aldrich, 98 %) the mixture was stirred for 24 h at 308 K. The dispersion was transferred into a glass-lined autoclave and treated at 413 K, for another 24 h. After cooling down to room temperature, the white precipitate was separated by filtration and washed with deionized water. The white solid was dried at 393 K overnight and calcined in a tube furnace for 6 h at 823 K with a heating ramp of 2.5 K min^{-1} under flowing air.

For the synthesis of ordered mesoporous CMK-3- and CMK-5-type carbon SBA-15 silica was placed in a mortar and ground with an appropriate amount (see below) of D-(-)fructose (ABCR, 99 %). For 1.0 g silica with a pore volume of 1.32 ml g^{-1}, 2.1 g fructose (density = 1.6 g mL^{-1}) was used to fill the pores nearly completely and, thus, to obtain CMK-3-type carbon. For CMK-5-type carbon, the amount of fructose was multiplied by 0.7. The respective mixture of silica fructose was heated to 393 K in a drying cabinet for 2 h. The resulting brown material was

then heated in a tube furnace under N_2 flow to 1173 K (heating to 573 K at a rate of 10 K/min; further heating to 633 K at 1 K/min; further heating to 1173 K at 5 K/min; constant heating at 1173 K for 4 h). After cooling, the resulting black solid was dispersed in hydrofluoric acid (Aldrich, 5 %) overnight twice. After recovering the carbon by filtration and repeated washing with deionized water and ethanol, it was dried over night at 393 K.

Characterization

All samples were analyzed by powder X-ray diffraction on a Bruker D8 AXS Advance diffractometer with a step size of 0.0075° (Cu-K_α, 40 kV, 40 mA). N_2 physisorption analysis was conducted on a Quantachrome Autosorb 6 at 77 K. Samples were degassed for 12 h at 393 K in vacuum prior to measurement. Average pore diameters were evaluated by using a non local density functional theory (NLDFT) data kernel (equilibrium model) for silica with cylindrical pores and for carbon with slit pore geometry, respectively. BET surface areas were calculated by the 5-point method (*60*) in the pressure region p/p_0 = 0.1-0.3. Micropore surface areas and pore volumes were calculated from a linear plot by the de Boer method at p/p_0 = 0.05-0.25 for SBA-15 silica and at p/p_0 = 0.05-0.6 for CMK-3 and CMK-5 carbon, respectively (*61*). Total pore volumes were determined by the adsorbed amount of N_2 at p/p_0 = 0.99. Transmission electron microscopy images were taken on a Philips CM30-ST microscope. Elemental analysis was carried out with an Elementar Vario MicroCube instrument, through thermal combustion followed by gas separation on a coloumn and quantitative detection with a thermal conductivity detector.

Results and Discussion

SBA-15 silica was synthesized by sol-gel synthesis with triblock copolymer Pluronic P-123 as structure directing agent, as described in the Experimental section. As depicted in Figure 2 the low-angle powder X-ray diffraction pattern of SBA-15 silica shows three well-resolved peaks (10, 11 and 20) associated with the two-dimensional hexagonal p6*mm* pore system symmetry. The d value (which is the d_{10} lattice spacing in the two-dimensional hexagonal pore arrangement and can be calculated from the respective scattering angle θ by Bragg´s law) corresponding to the 10 reflection is 9.7 nm. CMK-3-type carbon is obtained as the negative replica of SBA-15. In contrast to the low-angle diffraction signature of the SBA-15 silica matrix, CMK-3-type carbon shows weaker resolved reflections (10 and 11) due to lower structural order, as frequently observed for this type of carbon synthesis. However, CMK-5-type carbon exhibits three distinguishable peaks (10, 11, and 20). The relative intensity of the 10 reflection is decreased in comparison to SBA-15 silica and CMK-3 carbon due to negative interferences, which is typical of this structure and well-discussed in the literature (*1*, *62*). The *d* value for both carbon materials is 9.1 nm for CMK-3 and 9.6 nm for CMK-5 respectively, comparable to the SBA-15 silica matrix within experimental error.

Porous materials can be analyzed by N_2 physisorption measurements. The adsorbed amount of N_2 as a function of relative N_2 pressure (p/p_0) is recorded at constant temperature (77 K). The form of the plot ('isotherm') helps to distinguish between different types of pore shapes and to calculate pore size distributions. The occurrence of hysteresis between the adsorption and the desorption isotherm offers further insight into the respective pore geometry (*63*). Figure 3a shows N_2 physisorption isotherms for CMK-3, CMK-5, and SBA-15 materials. All three materials exhibit type-IV shape as typical of uniform, cylindrical mesopores. The corresponding pore size distribution curves are shown in Figure 3b. SBA-15 silica has an average pore diameter of 10.5 nm and a specific BET surface area of 482 m^2 g^{-1}, the specific pore volume is 1.32 ml g^{-1}. Micropores contribute to the specific surface area by 73 m^2 g^{-1}, as calculated by the thickness-plot (t-plot) method (*61*).

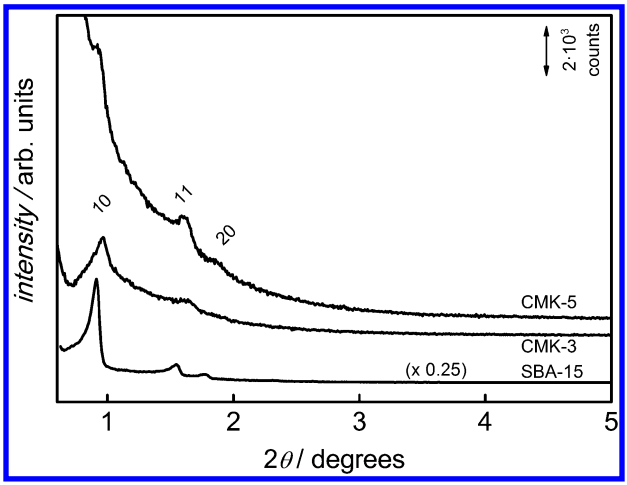

Figure 2. Low-angle powder X-ray diffraction patterns of mesoporous CMK-3 and CMK-5 carbon materials as well as SBA-15 silica which served as the structure matrix in both cases. Data are vertically shifted for clarity.

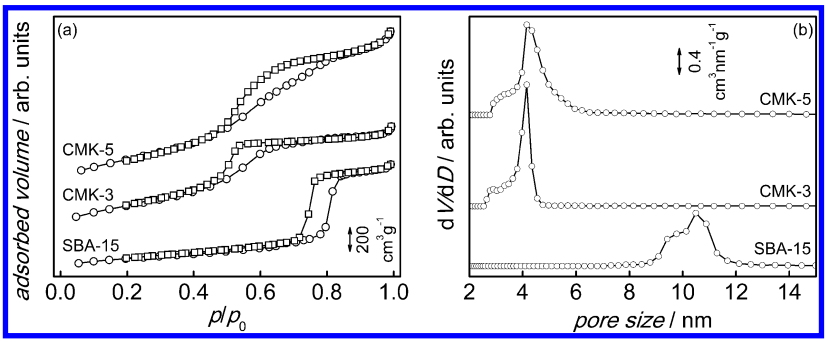

Figure 3. N_2 physisorption isotherms (a) and pore size distribution curves (b) of the same samples as shown in Figure 2. Data are vertically shifted for clarity.

The sorption isotherm of SBA-15 silica shows pronounced H1-type hysteresis, as expected for uniform, cylindrical mesopores. In contrast, both carbon samples exhibit less well-defined hysteresis behavior, indicating less uniform pore shape and width. This, too, confirms the pore shape that is to be expected for a replica structure obtained from SBA-15 silica, namely an intermediate between tubular and slit-like pores. The CMK-3-type carbon material has a specific BET surface area of 1219 m^2 g^{-1}, which is remarkably higher than for SBA-15 silica. This is explained by the lower density of carbon (bulk density of amorphous carbon (*64*): 1.8 mL g ^{1}) as compared to silica (bulk density of amorphous silica (*64*): 2.2 mL g^{-1}) and by a higher degree of microporosity (89 m^2 g^{-1}); the total pore volume is 1.45 mL g^{-1}.

The CMK-5-type carbon exhibits an even larger specific surface area of 1420 m^2 g^{-1} and a total pore volume of 2.10 mL g^{-1}. This can be explained by the occurrence of the additional pore system, *i.e.* the hollow nature of the carbon rods. Here micropores contribute to the specific surface area by 118 m^2 g^{-1}. Both carbon materials have the same average pore size of 4.2 nm, which indicates that the second type of pore in CMK-5 happens to have the same dimension as the first type occurring in both carbon materials (*1*). Nevertheless, the pore size distribution is slightly broader for CMK-5 than for CMK-3 which may be explained by the additional pore system.

Figure 4 shows representative transmission electron microscopy (TEM) images of SBA-15 silica (a) along the pore axis, where bright parts represent the pores and the dark areas the silica (pore walls). Figure 2b shows a TEM image of CMK-3 along the same axis, illustrating that this material is a negative replica of the SBA-15 silica structure matrix. The hexagonal geometry is clearly visible, where the dark parts represent the carbon material and the bright parts the pores, i.e. the space between the carbon rods. The view perpendicular to the pore axis in the same sample is shown in Figure 3c. Finally, Figure 4d displays CMK-5 carbon along the pore axis, clearly showing that the carbon rods (seen in cross section) are hollow.

The structural parameters for the SBA-15 silica structure matrix and for the CMK-3- and CMK-5-type carbon materials are summarized in Table 1.

Elemental analysis of the carbon materials, reveals a composition of 91.6 wt-% C, 1.2 wt-% H, and 6.4 wt-% O, indicating a 0.8 wt-% fraction of unknown element(s), most likely residual silicon due to incomplete removal of silica by etching with hydrofluoric acid. These results are comparable with those reported for ordered mesoporous carbon from acidic sucrose solution (*65*).

The degree of ‘graphitization’ can be influenced by the addition of heteroatoms, such as nitrogen and oxygen. The resulting surface hydrophilicity is discussed in detail in recent literature and makes these materials interesting for the adsorption of heavy metal ions or for general waste water cleaning (*55*).

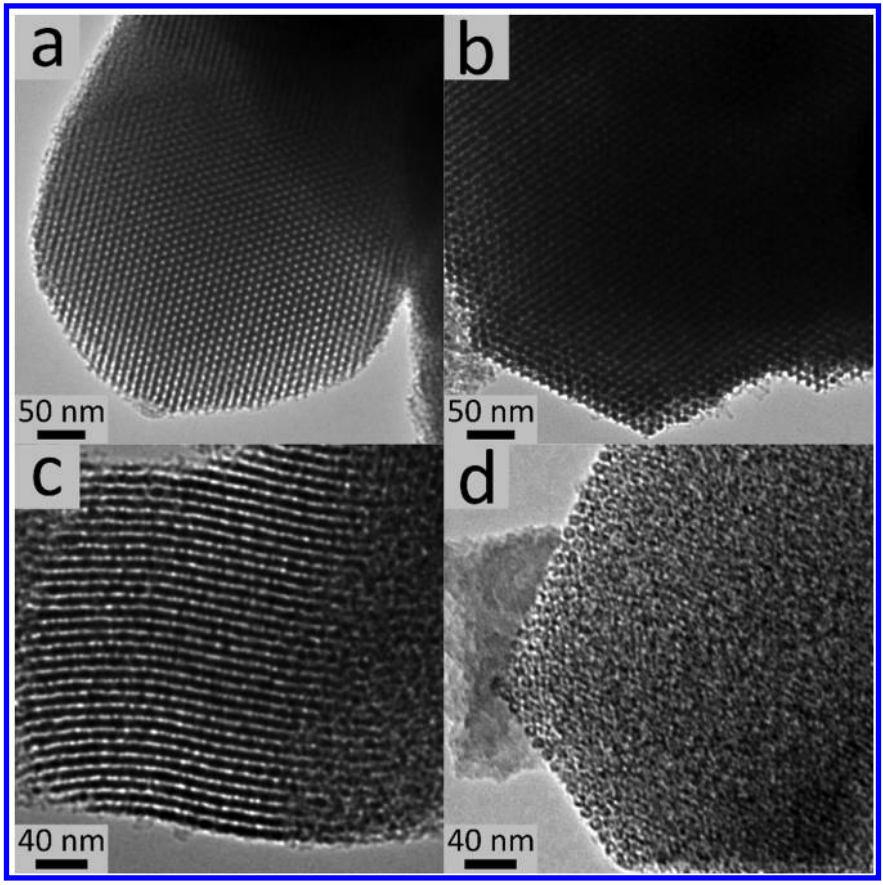

Figure 4. Representative transmission electron microscopy (TEM) images of SBA-15 silica (a), CMK-3-type carbon (b, c), and CMK-5-type carbon (d). (Image b and d are reproduced with permission from reference (54). Copyright (2012) John Wiley and Sons.)

Table 1. Structural parameters (from X-ray diffraction and N^2 physisorption) of ordered mesoporous carbon materials, as well as their structure matrix

	d (nm)	*pore diameter (nm)*[a]	*BET* $(m^2\ g^{-1})$[b]	*micropore area* $(m^2\ g^{-1})$[c]	*pore volume* $(cm^3\ g^{-1})$[d]
SBA-15	9.7	10.5	482	73.3	1.32
CMK-3	9.1	4.2	1219	89.0	1.45
CMK-5	9.6	4.2	1425	118.4	2.10

[a] Calculated with NLDFT (equilibrium model) kernel for silica with cylindrical pore or carbon with slit pore geometry, respectively. [b] BET surface (5-point method, $0.1 \leq p/p_0 \leq 0.3$). [c] Estimated from t-plot method (de Boer). [d] Total pore volume (from adsorbed amount of N_2 at $p/p_0 = 0.99$).

Conclusion

Ordered mesoporous carbon materials were synthesized from fructose by structure replication (nanocasting) utilizing SBA-15 silica as a structure matrix. By using a melt rather than a solution of fructose, only a single step of impregnating the silica matrix is necessary. Varying the relative amount of fructose within the pores of the matrix facilitates the synthesis of either CMK-3-type or CMK-5-type carbon. The synthesized products possess large surface areas up to 1420 $m^2\ g^{-1}$ and pore volumes up to 2.1 mL g^{-1}.

Acknowledgments

C. Weinberger thanks the Fonds der Chemischen Industrie for a Ph.D. Fellowship.

References

1. Lu, A. H.; Li, W. C.; Schmidt, W.; Kiefer, W.; Schüth, F. *Carbon* **2004**, *42*, 2939–2948.
2. Ohkubo, T.; Miyawaki, J.; Kaneko, K.; Ryoo, R.; Seaton, N. A. *J. Phys. Chem. B* **2002**, *106*, 6523–6528.
3. He, J.; Ma, K.; Jin, J.; Dong, Z.; Wang, J.; Li, R. *Microporous Mesoporous Mater.* **2009**, *121*, 173–177.
4. Taguchi, A.; Schüth, F. *Microporous Mesoporous Mater.* **2005**, *77*, 1–45.
5. Lu, A. H.; Nitz, J. J.; Comotti, M.; Weidenthaler, C.; Schlichte, K.; Lehmann, C. W.; Terasaki, O.; Schüth, F. *J. Am. Chem. Soc.* **2010**, *132*, 14152–14162.
6. Joo, S. H.; Choi, S. J.; Oh, I.; Kwak, J.; Liu, Z.; Terasaki, O.; Ryoo, R. *Nature* **2001**, *412*, 169–172.
7. Zhou, H.; Zhu, S.; Honma, I.; Seki, K. *Chem. Phys. Let.* **2004**, *396*, 252–255.

8. Makal, T. A.; Li, J. R.; Lu, W.; Zhou, H. C. *Chem. Soc. Rev.* **2012**, *41*, 7761–7779.
9. Sun, B.; Liu, H.; Munroe, P.; Ahn, H.; Wang, G. *Nano Res.* **2012**, *5*, 460–469.
10. Han, F.; Li, W. C.; Li, M. R.; Lu, A. H. *J. Mater. Chem.* **2012**, *22*, 9645–9651.
11. Huang, C. C.; He, J. C. *Chem. Eng. J.* **2013**, *221*, 469–475.
12. Xing, W.; Qiao, S. Z.; Ding, R. G.; Li, F.; Lu, G. Q.; Yan, Z. F.; Cheng, H. M. *Carbon* **2006**, *44*, 216–224.
13. Ndamanisha, J. C.; Guo, L. p. *Anal. Chim. Acta* **2012**, *747*, 19–28.
14. Zhang, C.; Zhao, Q.; Wan, L.; Wang, T.; Sun, J.; Gao, Y.; Jiang, T.; Wang, S. *Int. J. Pharm.* **2014**, *461*, 171–180.
15. Wang, S. *Microporous Mesoporous Mater.* **2009**, *117*, 1–9.
16. Lu, A. H.; Schmidt, W.; Spliethoff, B.; Schth, F. *Chem. Eur. J.* **2004**, *10*, 6085–6092.
17. Lu, A. H.; Schmidt, W.; Taguchi, A.; Spliethoff, B.; Tesche, B.; Schüth, F. *Angew. Chem., Int. Ed.* **2002**, *41*, 3489–3492.
18. Roggenbuck, J.; Tiemann, M. *J. Am. Chem. Soc.* **2005**, *127*, 1096–1097.
19. Roggenbuck, J.; Koch, G.; Tiemann, M. *Chem. Mater.* **2006**, *18*, 4151–4156.
20. Wagner, T.; Waitz, T.; Roggenbuck, J.; Fröba, M.; Kohl, C. D.; Tiemann, M. *Thin Solid Films* **2007**, *515*, 8360–8363.
21. Waitz, T.; Tiemann, M.; Klar, P. J.; Sann, J.; Stehr, J.; Meyer, B. K. *Appl. Phys. Lett.* **2007**, *90*, 123108–3.
22. Roggenbuck, J.; Waitz, T.; Tiemann, M. *Microporous Mesoporous Mater.* **2008**, *113*, 575–582.
23. Haffer, S.; Weinberger, C.; Tiemann, M. *Eur. J. Inorg. Chem.* **2012**, 3283–3288.
24. Haffer, S.; Weinberger, C.; Tiemann, M. *Z. Anorg. Allg. Chem.* **2012**, *638*, 1578–1578.
25. Haffer, S.; Lüder, C.; Ebbinghaus, S.; Köferstein, R.; Walther, T.; Tiemann, M. *Z. Anorg. Allg. Chem.* **2012**, *638*, 1577–1577.
26. Roggenbuck, J.; Schäfer, H.; Tsoncheva, T.; Minchev, C.; Hanss, J.; Tiemann, M. *Microporous Mesoporous Mater.* **2007**, *101*, 335–341.
27. Lu, A. H.; Schüth, F. *Adv. Mater.* **2006**, *18*, 1793–1805.
28. Tiemann, M. *Chem. Mater.* **2007**, *20*, 961–971.
29. Tiemann, M. *Chem. Eur. J.* **2007**, *13*, 8376–8388.
30. Wagner, T.; Haffer, S.; Weinberger, C.; Klaus, D.; Tiemann, M. *Chem. Soc. Rev.* **2013**, *42*, 4036–4053.
31. Gu, D.; Schüth, F. *Chem. Soc. Rev.* **2014**, *43*, 313–344.
32. Liang, C.; Hong, K.; Guiochon, G. A.; Mays, J. W.; Dai, S. *Angew. Chem. Int. Ed.* **2004**, *43*, 5785–5789.
33. Liang, C.; Dai, S. *J. Am. Chem. Soc.* **2006**, *128*, 5316–5317.
34. Tanaka, S.; Nishiyama, N.; Egashira, Y.; Ueyama, K. *Chem. Commun.* **2005**, 2125–2127.
35. Meng, Y.; Gu, D.; Zhang, F.; Shi, Y.; Yang, H.; Li, Z.; Yu, C.; Tu, B.; Zhao, D. *Angew. Chem., Int. Ed.* **2005**, *44*, 7053–7059.
36. Zhang, F.; Meng, Y.; Gu, D.; Yan, ; Yu, C.; Tu, B.; Zhao, D. *J. Am. Chem. Soc.* **2005**, *127*, 13508–13509.
37. Ma, T. Y.; Liu, L.; Yuan, Z. Y. *Chem. Soc. Rev.* **2013**, *42*, 3977–4003.

38. Ryoo, R.; Joo, S. H.; Jun, S. *J. Phys. Chem. B* **1999**, *103*, 7743–7746.
39. Jun, S.; Joo, S. H.; Ryoo, R.; Kruk, M.; Jaroniec, M.; Liu, Z.; Ohsuna, T.; Terasaki, O. *J. Am. Chem. Soc.* **2000**, *122*, 10712–10713.
40. Kleitz, F.; Hei Choi, S.; Ryoo, R. *Chem. Commun.* **2003**, 2136–2137.
41. Liang, C.; Li, Z.; Dai, S. *Angew. Chem., Int. Ed.* **2008**, *47*, 3696–3717.
42. Kyotani, T.; Nagai, T.; Inoue, S.; Tomita, A. *Chem. Mater.* **1997**, *9*, 609–615.
43. Rodriguez-Mirasol, J.; Cordero, T.; Radovic, L. R.; Rodriguez, J. J. *Chem. Mater.* **1998**, *10*, 550–558.
44. Niebrzydowska, P.; Janus, R.; Kustrowski, P.; Jarczewski, S.; Wach, A.; Silvestre-Albero, A. M.; Rodríguez-Reinoso, F. *Carbon* **2013**, *64*, 252–261.
45. Parmentier, J.; Patarin, J.; Dentzer, J.; Vix-Guterl, C. *Ceram. Int.* **2002**, *28*, 1–7.
46. Parmentier, J.; Saadhallah, S.; Reda, M.; Gibot, P.; Roux, M.; Vidal, L.; Vix-Guterl, C.; Patarin, J. *J. Phys. Chem. Solids* **2004**, *65*, 139–146.
47. Wang, B.; Ang, T. P.; Borgna, A. *Microporous Mesoporous Mater.* **2012**, *158*, 99–107.
48. Xia, Y.; Mokaya, R. *Adv. Mater.* **2004**, *16*, 1553–1558.
49. Yue; Zhou *Chem. Mater.* **2007**, *19*, 2359–2363.
50. Wang, Y. M.; Wu, Z. Y.; Shi, L. Y.; Zhu, J. H. *Adv. Mater.* **2005**, *17*, 323–327.
51. Yue, W.; Hill, A. H.; Harrison, A.; Zhou, W. *Chem. Commun.* **2007**, 2518–2520.
52. Shon, J. K.; Kong, S. S.; Kim, Y. S.; Lee, J. H.; Park, W. K.; Park, S. C.; Kim, J. M. *Microporous Mesoporous Mater.* **2009**, *120*, 441–446.
53. Klaus, D.; Amrehn, S.; Tiemann, M.; Wagner, T. *Microporous Mesoporous Mater.* **2014**, *188*, 133–139.
54. Weinberger, C.; Haffer, S.; Tiemann, M.; Wagner, T. *Z. Anorg. Allg. Chem.* **2012**, *638*, 1578–1578.
55. Weinberger, C.; Haffer, S.; Wagner, T.; Tiemann, M. *Eur. J. Inorg. Chem.* **2014**, *2014*, 2787–2792.
56. Grano, A. J.; Sayler, F. D.; Smått, J.-H.; Bakker, M. G. *J. Mater. Res.* **2013**, *28*, 2483–2489.
57. Xia, K.; Gao, Q.; Wu, C.; Song, S.; Ruan, M. *Carbon* **2007**, *45*, 1989–1996.
58. Wu, Z.; Zhao, D. *Chem. Commun.* **2011**, *47*, 3332–3338.
59. Zhao, D.; Feng, J.; Huo, Q.; Melosh, N.; Fredrickson, G. H.; Chmelka, B. F.; Stucky, G. D. *Science* **1998**, *279*, 548–552.
60. Brunauer, S.; Emmett, P. H.; Teller, E. *J. Am. Chem. Soc.* **1938**, *60*, 309–319.
61. Lippens, B. C.; de Boer, J. H. *Journal of Catalysis* **1965**, *4*, 319–323.
62. Schmidt, W. *Microporous Mesoporous Mater.* **2009**, *117*, 372–379.
63. Sing, K. S. W. *Pure Appl. Chem.* **1985**, *57*, 603–619.
64. *CRC Handbook of Chemistry and Physics*, 87th ed.; Lide, D. R., Ed.; CRC Press/Taylor and Francis Group: Boca Raton, FL, 2006.
65. He, C.; Hu, X. *Adsorption* **2012**, *18*, 337–348.

Chapter 2

Chemical Beam Epitaxy of Gallium Nitride Nanowires

Ryan A. Munden*,[1] and Mark A. Reed[2]

[1]Electrical Engineering, Fairfield University, 1073 N. Benson Rd., Fairfield, Connecticut 06824, United States
[2]Electrical Engineering and Applied Physics, Yale University, 15 Prospect St., New Haven, Connecticut 06520, United States
***E-mail: rmunden@fairfield.edu**

Semiconductor nanowires have become a field of intense investigation in the pursuit of bottom-up materials and their devices; they will continue to scale in size, while offering new capabilities in fields such as computation, optoelectronics, biosensing, and photovoltaics. Semiconducting nanowires have been grown using a variety of techniques. The most common method, hot-wall chemical vapor deposition (CVD), has been successfully used to grow a variety of semiconductor nanowire materials. Extensive investigation of statistically significant numbers of gallium nitride (GaN) nanowires grown by hot-wall CVD has shown that these nanowires have low mobilities (~1 $cm^2V^{-1}s^{-1}$) and high carrier concentrations (~10^{18} cm^{-3}). In essence, hot-wall CVD growth occurs near equilibrium conditions and does not permit easy tuning of the parameters of the nanowire growth to achieve the desired electronic characteristics. Growth of GaN nanowires has been achieved using the chemical beam epitaxy method (CBE). CBE is a non-equilibrium growth technique that grows material in a high vacuum with all gas-source precursors. This enables control of precursor delivery, independent of the growth temperature. Initial results demonstrate aligned nanowire growth, but that is dominated by self-catalyzed growth of nanowires, as opposed to metal catalyst mediated growth via the Vapor-Liquid-Solid (VLS) method. The CBE opens up the possibility of growing

In The Science and Function of Nanomaterials: From Synthesis to Application; Harper-Leatherman, et al.;

compound semiconductor nanowires with repeatable and controllable characteristics.

Introduction

One of the aims of nanoscience and technology is to create low-dimensional structures with electronic and photonic properties that replicate those of conventionally fabricated systems, but to do so in ultra-small structures created by alternative synthetic means. In this way we hope to create circuit elements that display interesting physical properties or have utility either in their own right or as components when integrated with more conventionally fabricated systems. There are also many interesting properties that arise from the small-scale of these nanostructures. Quantum and low-dimensionality effects produce unique benefits for both devices and basic investigation of physical principles, while simultaneously making those investigations very difficult to carry out. Hopes are bright for using nanostructures or even individual molecules as sensors (*1*), ultrahigh density data storage (*2*), logic gates (*3*), sub-wavelength light guides (*4*), or other light-management circuitry (*5*).

Semiconductor nanowires are making progress toward these goals. Semiconductor nanowires offer the possibility of tailoring the electronic properties in a very controlled way, using methods and theory similar to that used in more conventional bulk and thin-film semiconductor growth. Nanowires may also provide a unique test bed for accessing low dimensionality effects (*6*). The possibility exists for modulation doping and heterojunction, or "superlattice (*7*)," nanowires, allowing materials to be grown along the axis of the nanowire and even along the radial direction (*8*). Rectification has been demonstrated in junctions formed by crossing single-walled metallic carbon nanotubes with semiconducting ones (*9*), in *p*-type InP nanowires crossed with *n*-type InP nanowires (*10*), in *p*-type InP nanowires crossed with *n*-type GaN nanowires (*11*), and in "heterojunctions" created by crossing a *p*-type Si nanowire with an *n*-GaN nanowire (*3*, *12*). A *p*–*n* junction was reported in a single piecewise-doped silicon nanowire produced by modulation doping (*13*). GaN nanowires with internal *p*–*n* junctions (*14*) have also been synthesized using vapor–liquid–solid (VLS) synthesis (*15*, *16*).

Growth of semiconductor nanowires can be achieved using a variety of techniques, building off of existing semiconductor materials growth methods for bulk materials. Nanowires have been successfully grown by hot-wall tube furnace chemical vapor deposition (HW-CVD) (*17*), Pulsed Laser Deposition (PLD) (*18*), Metalorganic Chemical Vapor Deposition (MOCVD) (*19*), Molecular Beam Epitaxy (MBE) (*20*), Chemical Beam Epitaxy (CBE) (*21*), and solution growth methods (*22*). Each method has its advantages and disadvantages. HWCVD and Solution techniques typically require lower cost equipment and have high throughput, while techniques like MOCVD, CBE, and MBE require costly vacuum systems, and toxic gas handling systems to operate. However, the more complicated systems usually provide better control over growth parameters enabling more complex and pure nanowires to be grown.

Nanowire Similarities to Bulk Materials

Nanowires can be grown from a variety of materials and using a variety of methods. Nanowires typically have diameters in the 10-100 nm range, even achieving lengths up to tens of microns, as shown in an example GaN nanowire in Figure 1. However, it is well supported in the literature that nanowires can be grown with a wide range of sizes, including much smaller diameters, and much shorter in length than one micron (*23*). They can be grown as single crystal materials, as shown by the example transmission electron microscope (TEM) image in Figure 2. Nanowires have a very high aspect ratio, but many properties remain similar to the bulk material properties.

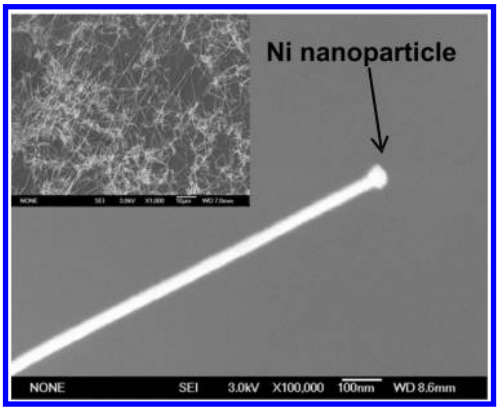

Figure 1. A single GaN nanowire shows the metallic Ni nanoparticle catalyst at the tip. Inset shows an SEM of many nanowires as grown on the surface of a crystalline substrate. (Reproduced with permission from reference (14). Copyright (2003) American Institute of Physics.)

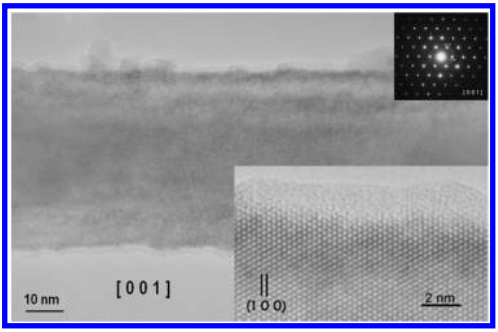

Figure 2. Close-up imaging of a GaN nanowire by TEM shows the small diameter of the nanowire clearly. The lower inset shows the crystalline nature of the nanowire by the regular arrangement of lattice planes and atoms. The upper inset shows the diffraction pattern which shows the hexagonal wurtzite crystal structure of the GaN nanowire. (Reproduced with permission from reference (14). Copyright (2003) American Institute of Physics.)

Nanowires' similarities to bulk materials allow application of more of the knowledge, methods, and fabrication techniques applicable to the semiconductor industry. The power of this large body of knowledge developed over many decades of research can be brought to bear on the research problems of semiconductor nanowires.

Nanowire chemistry can be better controlled. The material compositions can be as varied as the entire range of crystal structures we are familiar with and can even permit combinations that are difficult to achieve in the bulk state. This allows parameters to be tailored in a controlled and repeatable way to achieve the desired electrical or chemical characteristics. By controlling the chemical precursors used in the growth of the nanowire, the composition can be controlled to great extent to achieve the desired doping (n or p type) to allow enhanced control over the electronic properties. Thus, nanowires with semiconductor, insulator, or metallic natures can be grown at will, instead of relying on the uncontrollable chirality of a nanotube. Control over the chemistry of nanowires allows the potential to further engineer the electronic properties by creating novel heterostructures through interfacing two or more different chemical make ups within the same nanowire (*24*). These heterostructures can be grown either axially or radially, offering the potential for controlling the band gap, controlling the optical properties, enhancing the mobility, and optimizing nanowires for any specific function.

Figure 3. Heterojunction nanowires such as this Si/SiGe superlattice from P. Yang's research open up the possibility of growing devices with unique engineered structure, bandgap, and optical properties. The light and dark bandsalong the nanowire in this TEM image show the presence of SiGe alloy. Due to the larger electron scattering cross section of the Ge atoms, SiGe appears darker than Si. (Reproduced with permission from reference (7). Copyright (2002) American Chemical Society.)

In The Science and Function of Nanomaterials: From Synthesis to Application; Harper-Leatherman, et al.;

Nanowires offer one very desirable advantage over traditional thin-film technologies when developing heterostructures; strain-relief. Thin-film heterostructures are always battling the presence of defects formed because of the lattice mismatch between the materials. Different strategies are used for strain accommodation to minimize the number of defects over large areas of the film. Often this requires complex growth of buffer layers and intricate transitions between materials to gradually relieve the strain inherent in the systems. Nanowires can naturally accommodate the strain by releasing it at the surface, which prevents the crystal defects from dominating the interior of the nanowire. In the realm of nanowires, heterostructures are generally classified into two broad groups regardless of the actual materials involved. These are axial heterostructures, where the material changes occur along the length of the nanowire, and radial heterostructures, where the material changes occur in a core-shell configuration. An example of a heterostructured nanowire, of the axial variety, is shown in Figure 3.

Application Areas

Nanowires hold the promise of being grown to meet the demands of many application areas. In the spirit of Moore's law, nanowires can function as very small active devices, to continue to scale down the size and increase the speed of integrated circuits. Nanowires have been shown to act like Field Effect Transistors (FETs), bipolar transistors, and rectifiers very early in their development. Though they do not yet have the scale of bulk silicon for traditional computational needs, they may prove a key element in future generations of ICs, either as stand-alone or hybrid computational devices.

The controllable chemistry and ability to create low-defect density crystal structures with engineered band gaps and heterostructures has opened the field of nanoscale optoelectronics. Nanowires have been shown to lase under optical pumping (*25*), to emit light as a Light-Emitting Diode (LED) (*26*), and to potentially act as very efficient photovoltaic energy converters (*27–30*).

The high surface to volume ratio of nanowires due to their high aspect ratio coupled with their controllable chemistry has made them especially attractive for biological and chemical sensing applications. Nanowires can readily be made into a highly sensitive chemFET by functionalizing the surface appropriately and detecting changes in the conductivity of the nanowire due to chemical reaction. Very little surface charge variation is needed to cause detectable changes in the current in the nanowire. Results have shown femto-molar sensitivities (*31*, *32*).

Mechanically, nanowires also present themselves as candidates for small-scale mechanical applications. Nanowire cantilevers have been used as picogram mass detectors (*33*). Super sharp Atomic Force Microscope (AFM) tips can also be made using a nanowire as the probe tip (*34*). Nanowires made of piezoelectric materials can even be used as tiny generators by bending them back and forth (*35*).

Though many practical applications for nanowires have been envisioned, their development hinges on finding ways to accurately control the properties to tune them for specific purposes. Understanding and controlling the growth of

In The Science and Function of Nanomaterials: From Synthesis to Application; Harper-Leatherman, et al.;

nanowires is a key component in developing these applications. Though much progress has been made, there is much yet to do. Chemical beam epitaxy (CBE) is one of various attempts to gain further control over nanowire composition, purity, structure, and repeatability.

VLS Model of Nanowire Synthesis

VLS Growth Model

The most widely used method for nanowire growth is commonly known by the acronym VLS, which stands for Vapor, Liquid, Solid. This method, pioneered in the 1960's by Wagner (*36*), paved the way for a boom in nanowire growth during the past two decades. VLS incorporates the three material phases to collect vapor precursors by alloying with a liquid catalyst near the eutectic point, which supersaturates, nucleates, and grows a crystal on a solid substrate. Growth generally takes place at very high temperatures, between 400-1100 °C. This method is roughly illustrated in Figure 4, where, moving left to right in the figure the change in precursor is illustrated as time advances from left to right.

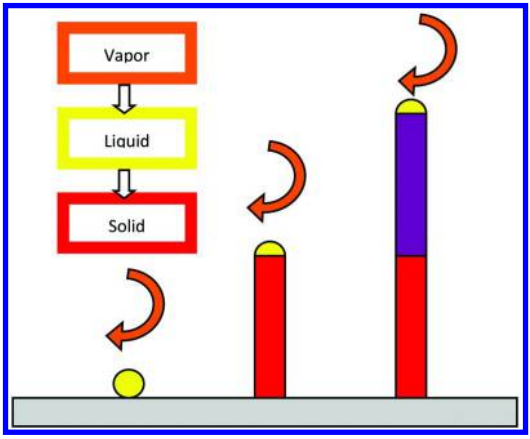

Figure 4. VLS growth mechanism. From left to right the figure represents the time ordered growth of a nanowire from vapor precursor deposited through a supersaturated liquid metallic catalyst droplet (yellow dot, left) into a solid crystal formation on the growth substrate. As time progresses the nanowire lenghthens (center). Changing the precursor gas changes the growing nanowire composition being deposited from catalyst tip (right).

Kinetics of Growth

The exact kinetics of growth in the VLS mechanism are still somewhat debatable. Current research is attempting to determine answers to questions about catalyst incorporation during growth, phase separation when growing compound semiconductor alloys, dopant incorporation, and the exact role played by the catalyst. Some materials show that a solid catalyst particle may remain during growth (a Vapor-Solid-Solid, or VSS model). There are also questions about how to control the crystal orientation and position of the growing NWs (*37*, *38*). Even so, there are empirical models that can adequately describe the growth for these discussions. A variation of the primary model used is shown in Equation 1.

$$J_{L-S} \propto \frac{P_{In} - P_{Surface}}{\sqrt{2\pi mkT}} \left[\alpha_1 + \alpha_2 \frac{L}{r} + \alpha_3 \left(\frac{\lambda}{r} \right)^2 \right]$$

Equation 1: Growth rate of nanowires (*39*)

The growth rate $J_{L\text{-}S}$ depends on the incoming gas pressure, P_{In}, the surface vapor pressure, $P_{Surface}$, and the empirically determined constants α_1, α_2, and α_3 that are related respectively to the gas molecules adsorbing at the tip, on the side-walls (of length L, and radius r), and the substrate surface (with surface diffusion length, λ) near the nanowire. These parameters are illustrated in Figure 5.

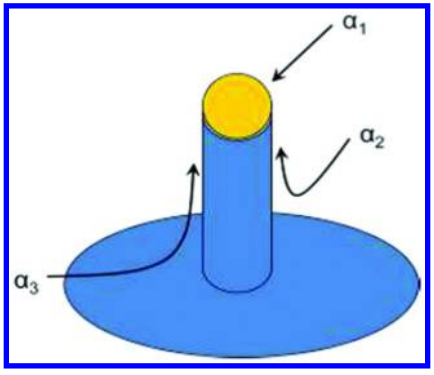

Figure 5. Diagram illustrating the respective regions of interest and their corresponding alphas from Equation 1.

There are several thermodynamic effects that also come into play in the growth of these highly asymmetric nanostructures. It is observed that thinner nanowires grow faster than their thicker counterparts (*40*). The Gibbs-Thomson effect dictates that below a certain threshold diameter the growth will again slow (*41*).

Difficulties in VLS Growth

Despite the numerous successes in growing complex structured nanowires, there remain several challenges which have not yet been fully resolved. Most nanowire growth systems rely on some sort of metallic catalyst, which alloys with the precursor materials. This raises the question of catalyst incorporation. Most catalysts are heavy metals such as gold, a poignant concern since gold is a lifetime killer, causing rapid recombination of electron and hole charge carriers, in semiconductor devices. Even a small amount of incorporation could potentially have huge effects on device performance. Efforts are moving forward using new analysis techniques such as atom probe tomography to determine the level of catalyst incorporation. So far, under most conditions, it appears that the metal catalyst does not appreciably intermingle with the main crystal body of the nanowire. However, there are certain growth regimes where this does not hold as well, so one must still exercise caution moving forward (*42*).

Another difficulty that must be overcome with nanowire synthesis is the ability to control dopant incorporation (*43*) or even the alloy elements when growing compound tertiary and quaternary semiconductor nanowires (*39*). Due to the high surface energy which arises from the surface curvature of the high surface-to-volume ratio nanowires, it is often energetically favorable for the dopant or alloy atoms to migrate to the outer surfaces of the nanowire, leading to a phase separation (*44*). This can be used in certain cases to provide a natural tendency to form core-shell type nanowires, but it is not always a desirable result. To date there is no standard growth method or technique that can eliminate this problem completely. The various systems used for nanowire growth attempt to address these issues in different ways.

This is only a brief overview of the mechanisms of VLS growth, to serve as an introduction to the topic of chemical beam epitaxy. The reader is referred to the literature for a far more detailed and complete explanation of the VLS growth mechanisms and challenges (*45–49*).

Types of Wires Grown

Many different materials have been grown as nanowires. The VLS method and its variants are particularly well suited to the growth of semiconductor nanowires; group IV, III-V, nitride, and oxide materials can all be efficiently grown. Metallic nanowires can be grown directly, or by chemical solution synthesis methods, as they are not as well suited to the high temperature growth of VLS. Table 1 summarizes a number of the different types of nanowires grown.

Table 1. Different semiconductor/metal combinations and growth methods for nanowires. (Added to and adapted from reference (*50*))

NW Material	*Source*	*Metal Catalyst*	*Growth process*	*Ref.*
Si	$SiCl_4$	Au	Chemical Vapor Deposition (CVD)	(*41*, *51*)
Si	$SiCl_4$	Au, Ag, Cu, Pt	CVD	(*36*)
Si,Ge	SiH_4,GeH_4	Au	CVD	(*52*)
Si	SiH_4	Au	CVD	(*53*)
Si,Ge		Fe,Si/Fe,Ge/Fe	Pulsed Laser Deposition (PLD)	(*18*)
Si	Si_2H_6	Au	CBE	(*20*)
GaAs	GaAs/Au	Au	PLD	(*17*)
InP	InP/Au	Au	PLD	(*17*)
CdSe	CdSe/Au	Au	PLD	(*17*)
Si	Si	Ga	microwave plasma	(*54*)
GaAs	Et_3Ga,Bu_3As	Au	CBE	(*21*)
ZnO	ZnO, C	Au	evaporation	(*25*)
Si	Si	Au	Molecular Beam Epitaxy (MBE)	(*55*)
Si	SiO	Au	evaporation	(*56*)
Si	silyl radicals	Ga	microwave plasma etching	(*54*)
Si	SiH_4 or SiH_2Cl_2	Ti	CVD	(*57*)

Continued on next page.

Table 1. (Continued). Different semiconductor/metal combinations and growth methods for nanowires

NW Material	*Source*	*Metal Catalyst*	*Growth process*	*Ref.*
GaAs/GaP	GaAs/GaP	Au	PLD	(*13*)
GaAs/InAs	Me_3Ga,Bu_3As,Me_3In	Au	CBE	(*21*)
Si/SiGe	$SiCl_4$	Au	Si: CVD; Ge: PLD	(*58*)
GaN	GaN/Fe	Fe	PLD	(*59*)
GaN	TMGa, NH_4	Au, Ni	CBE	(*60*)

Chemical Beam Epitaxy of Nanowires

Second generation growth systems provide the capability to tune the growth parameters with more precision over a wider range of values than those attainable by the equilibrium growth system of the hot-wall CVD (the tube furnace). One of the most successful methods for growing high quality nanowires with unique and controllable electronic properties is CBE. The Samuelson group at Lund University, Sweden has done very thorough characterization of the CBE technique for III-V In/Ga-As/P materials systems (*21*, *61*, *62*). Though not without its own difficulties in implementation, the CBE makes use of the high-vacuum of the MBE with the control of precursor delivery offered by the metalorganic sources of MOCVD, and it potentially allows the incorporation of plasma cracked sources to reduce the growth temperatures necessary.

CBE Reactor and Growth Concepts

Chemical beam epitaxy is a growth system using metal-organic and gas precursors to grow semiconductor nanostructures in a high-vacuum environment. Figure 6 shows a diagram of the CBE reactor, with a cutaway on the growth chamber showing the configuration of the heater assembly. The actual system, as built in-house is shown in Figure 7. A more thorough description of the system and growth parameters are found in the reference by Munden (*60*). The system includes a high vacuum growth chamber maintained under vacuum by a turbo molecular pump (TMP) system. The turbo molecular pump maintains pressures below the range of ~10^{-6} torr. There is a separate load-lock antechamber for sample entry and exit via a high vacuum magnetic transporter, which is independently pumped by its own turbo pump. This allows the samples to be completely isolated from the atmosphere, maintaining the purity of the growth chamber, as well as protecting users from undesirable exposure to hazardous precursors. The load-lock also houses a Stanford Research Systems RGA 300, a residual gas analyzer (RGA), used to monitor the status of the load-lock prior to opening to the atmosphere. It can also be used to leak check and to monitor overall system cleanliness in the growth chamber by opening the gate valve.

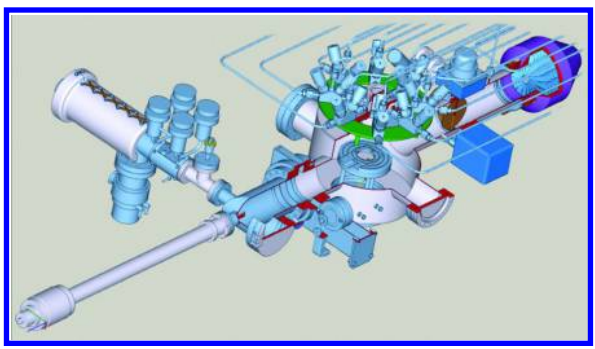

Figure 6. Growth Chamber of CBE reactor.

In The Science and Function of Nanomaterials: From Synthesis to Application; Harper-Leatherman, et al.;

Figure 7. Custom designed chemical beam epitaxy (CBE) system for semiconductor nanowire growth at Yale University.

The gas sources are admitted under their own vapor pressure through regulated mass flow controllers (MFC). Unlike conventional MOCVD, there is not necessarily a need for a separate "push gas," such as hydrogen or nitrogen, because of the high vacuum in the growth chamber. Enough of a pressure differential exists across the MFCs to maintain flow even when the source vapor pressures are only a few to tens of torr. Higher pressure sources, such as ammonia, can also be admitted controllably using this same technique. Due to the high vacuum (~10^{-8} torr base pressure, ~10^{-5} torr growth pressure) each gas species enters the chamber in the molecular flow regime. The gases enter the growth chamber through an injector flange assembly that directs all molecular beams onto the substrate. The molecular flow of sources means there are no interactions or reactions between molecules except at the substrate surface. This enables very precise control of material composition. Changes can be made in source composition by careful control of the MFCs and source valving, allowing the growth of high purity epitaxial material and heterojunction materials with material transitions on the atomic scale.

The substrate is heated to the appropriate temperature for source decomposition and material recrystallization. This initiates growth in a non-equilibrium regime due to the high arrival rates of molecules and the low decomposition temperature of the metalorganic sources. If the gas molecules are thermally decomposed at the surface, they may react with other molecules or the surface itself to form an epitaxial layer at the nucleation sites on the substrate. Metallic catalyst particles can be used to enhance anisotropic growth because the decomposed precursors can enter the catalyst due to the higher sticking coefficient and preferential eutectic alloying. This will allow growth of semiconductor nanostructures to occur with a high degree of control. The volatility of the unreacted molecules ensures that unreacted species are quickly removed from the system. The heater is capable of heating to ~1000 °C, enabling thermal decomposition of all metalorganic precursors, as well as the much more stable ammonia precursor for nitride growth. Heating is provided by a 1000 W quartz halogen lamp which radiatively heats a silicon support wafer. The thermocouple is positioned on the top of the substrate heater using a molybdenum clip to hold it in contact with the wafer surface for a better temperature reading.

The heater assembly mounts the substrate by sliding a sample holder into a dove-tailed dock machined into the surface of the heater assembly. Thus the substrate remains nearly flush with the surface of the heater assembly to lie at the focal point of the precursor beams. All of this is designed to optimize the likelihood of precursors cracking and depositing on the substrate surface, not the growth chamber surfaces.

Metalorganic precursor choice is flexible and varied, and can be chosen to minimize potential health risks. Precursors can be chosen for their decomposition temperature, vapor pressure, byproducts, and safety factors. In general it is desirable to have a precursor with a high vapor pressure to ease delivery and a relatively low decomposition temperature to ensure complete disassociation of the impinging molecules upon contact with the substrate. One other consideration is the volatility and decomposition of initial precursor byproducts. Byproducts should be relatively stable and volatile to ensure that they are fully pumped from the chamber before they can decompose at the growth substrate and lead to possible contamination. One such example is carbon impurity incorporation due to the decomposition of methyl groups at the surface (*63*). No hazardous hydrides or elemental group V sources are used. Instead, metalorganic sources such as trisdimethylamminophosphine (TDMAP) have been chosen. These sources cannot decompose into the more dangerous hydride forms.

The gas handling system consists of an MFC feeding a single source gas into a run-vent valve configuration. The vent valve allows flows to be established while flowing gas into the exhaust treatment system, then switching to the growth chamber. This provides more accurate control of source delivery to the substrate.

Each of the source inlets is low temperature, that is, no cracking of the precursors occurs prior to entry in to the growth chamber. In addition to the metalorganic precursors, ammonia is used as a source for nitride growth. Possible precursors include those in Table 2.

Table 2. Chemical Precursors for CBE. (Reproduced with permission from reference (*60*), 2014, Munden)

Chemical Precursors for CBE		
Group II	Formula	Character
Bis(methylcyclopentadienyl) magnesium	$(C_5H_4CH_3)_2Mg$	Solid powder p-type dopant
Group III		
Trimethylgallium (TMGa)	$(CH_3)_3Ga$	Liquid Group III growth source
Trimethylindium (TMI)	$(CH_3)_3In$	Liquid Group III growth source
Trimethylaluminum (TMAl)	$(CH_3)_3Al$	Liquid Group III growth source
Group IV		
Silane	SiH_4	Gas Group IV n-type dopant
Group V		
Ammonia	NH_3	Gas Group V growth source
Tris(dimethylamino)phosphine (TDMAP)	$((CH_3)_2N)_3P$	Liquid Group V growth source
Tris(dimethylamino)arsine (TDMAAs)	$((CH_3)_2N)_3As$	Liquid Group V growth source

GaN Nanowire Growth in CBE

Very well controlled and characterized growth of InAs nanowires in a CBE system has been achieved in the Samuelson group at Lund University (*61*). Growth of gallium nitride is not as straight forward as growth of III-arsenides/phosphides in bulk or thin-film applications, due to the higher energy necessary for high quality nitride crystal formation. Gallium Nitride's growth by chemical beam epitaxy is no exception. The availability of nitrogen bearing precursors makes ammonia the most easily available and useable source for most applications, but it requires very high temperatures to decompose into hydrogen and atomic nitrogen (≥ 750 °C). The control of dopants, defects, and impurities is also much more difficult as evidenced by the growth of GaN films and nanowires via MOCVD and HW-CVD. However, initial results of growth in the CBE show that CBE may allow tighter control of growth parameters. This would potentially enable control of growth, such as substrate alignment, comparable to that achieved in the arsenides and phosphides (see Figure 8).

Growths of GaN nanowires in the CBE system have approached the level of those grown by hot-wall CVD and MOCVD, (in terms of their morphology). Work with the CBE system has focused on improving growth yield, morphology, and materials characteristics to develop process recipes that will grow nanowires with the same characteristics repeatably from run to run so that future device fabrication can count on high-quality, well-understood nanowires.

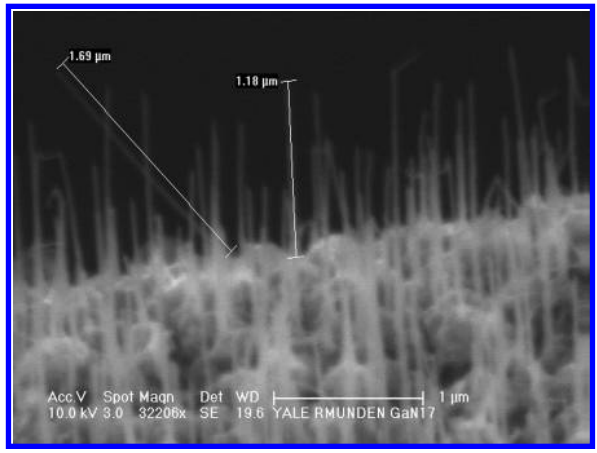

Figure 8. Growth of GaN nanowires shows alignment to substrate.

Initial growth conditions were chosen to be similar to those used for hot-wall CVD, since nanowires were regularly (though not always repeatably) grown within a certain range of parameters. Initial growth results can be characterized primarily as microcrystalline and film-like, as is highlighted by the GaN crystallites shown in Figure 9 and Figure 10. These structures are generally micron-sized, as evidenced by their clear appearance in the optical microscope image of the GaN sample in Figure 9, with many crystals growing to nearly 50 microns in length and 5 – 10 microns in width. This sample was grown on

In The Science and Function of Nanomaterials: From Synthesis to Application; Harper-Leatherman, et al.;

sapphire substrate with 30Åof evaporated Ni metal catalyst, at 780 °C, with 300 sccm (standard cubic centimeters per minute) of ammonia and 3 sccm of TMG as precursor flows, for 180 mins.

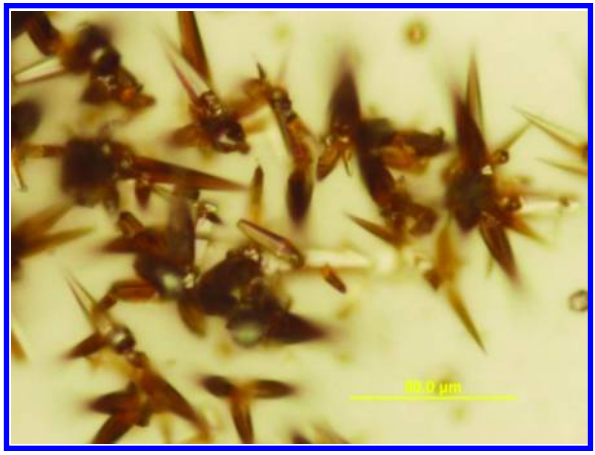

Figure 9. Optical micrograph of GaN microcrystals on alumina substrate.

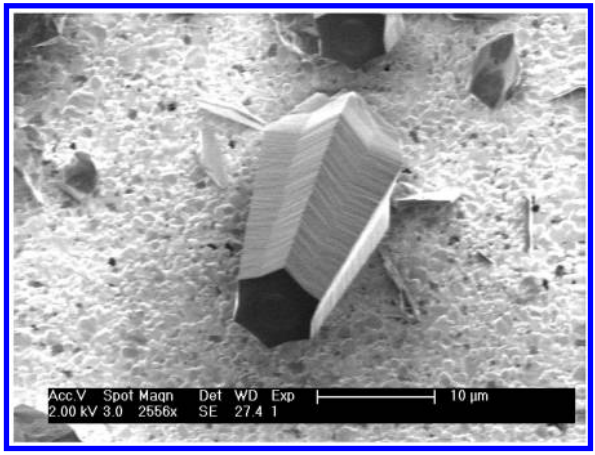

Figure 10. SEM micrograph of GaN microcrystal showing screw dislocations growing out of rough GaN film on alumina substrate.

Closer inspection of the sample by Field Emission Scanning Electronc Microscope (FE-SEM), Figure 10, revealed that the surface of the alumina substrate was covered by a polycrystalline GaN coating, which nucleated the larger microcrystals and single crystalline platelets. The microcrystals clearly emphasize the hexagonal structure of GaN. Many of these crystals also show a depression in the center of the hexagonal structure that is likely caused by a screw defect influencing the growth of the crystals. Energy dispersion spectroscopy (EDS) spectra of GaN nanowires grown on alumina (as shown in Figure 11) using

gold as a catalyst show all relevant peaks present: Al and O from the substrate, the very strong Ga peak from GaN nanowires and coating, the small Au peak from the catalyst, and very weakly, the N peak. There may also be small amounts of C and Si due to the chamber and contamination during transfer. It can be very difficult to make out the lighter elements such as N and C using EDS, so EDS cannot be used for quantitative analysis, but is evidence of the presence of the elements of interest.

Examining different regions of the substrate revealed clues about the growth process of the microcrystals and the possibilities for nucleating nanowires. In Figure 12 (left) the GaN film coating the surface and nucleating the microcrystals is seen to form from roughly spherical polycrystalline balls of GaN, or "nano-cauliflower". These spheroids are likely nucleated by the metallic catalyst, but growth conditions lead to agglomeration and large polycrystalline growth. One facet can then begin to dominate and grow the hexagonal structure. Certain of the nanocauliflower-nucleated, self-terminating, tapered hexagonal crystals, as shown in Figure 12 (center), grew into the needle-like structure. The tips of the tapered structures and other points on the nanocauliflowers can serve as nucleation points to launch the growth of nanowires, as shown in Figure 12 (right). In areas not dominated by nanocauliflower, clusters on the surface were capable of nucleating small clumps of dispersed nanowires (Figure 13). These initial growths showed the possibility of growing nanowires in the CBE with growth temperatures around 700 C, ammonia flow rates around 200 sccm, and low TMGa flow of about 3 sccm. It seemed from these early growths that achieving high-yield nanowire growth would be possible since at least a few nanowires grew.

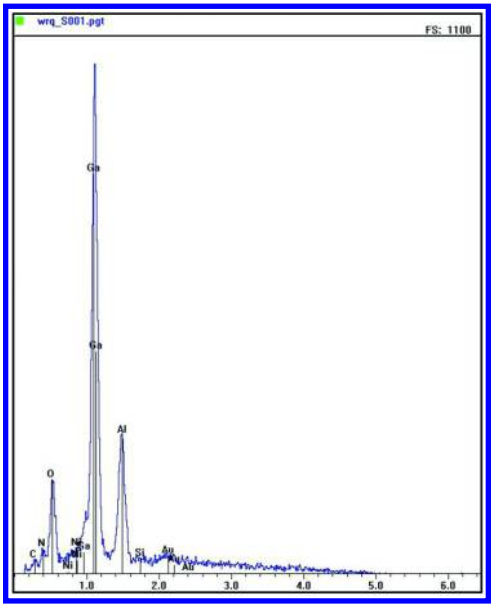

Figure 11. EDS spectra of GaN nanowires on alumina using gold catalyst showing presence of relevant peaks.

In The Science and Function of Nanomaterials: From Synthesis to Application; Harper-Leatherman, et al.;

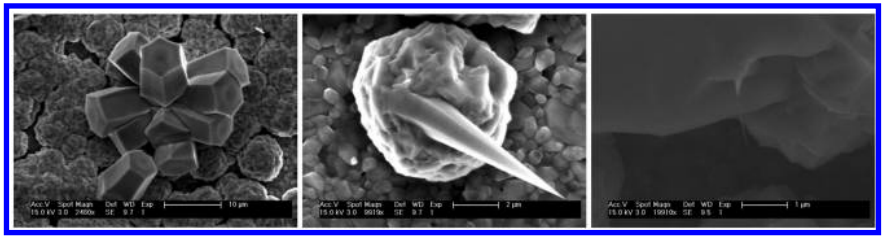

Figure 12. Cluster of GaN microcrystals growing out of GaN "nanocauliflower"(left), closeup of GaN "nanocauliflower" (center), nucleation short nanowire from tip of "nanocaulflower surface (right).

Other early growths were very gallium rich, leaving droplets of liquid gallium covering the surface (Figure 14). Between these droplets nanowires were still able to grow. This showed that gallium flux was too high. However, these microcrystals were grown near the lower limit of the MFC controllability. MFCs are only able to be controlled down to 10% of their max flow capability, which for the TMGa MFC is a 100 sccm rating. Roughly adjusted for the heat capacity of TMGa, the minimum flow rate is approximately 5 sccm.

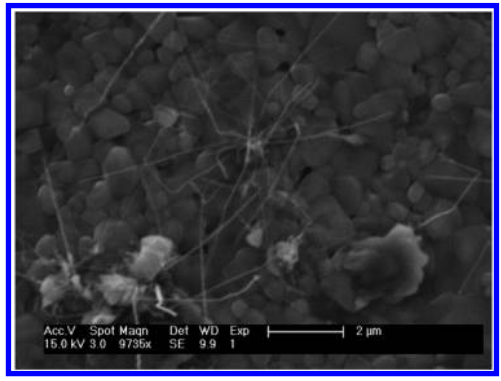

Figure 13. GaN nanowires grown from much smaller nucleation particles. Some isolated wires were 10's of microns long and as thin as 20nm.

From these initial growths, it was realized that the TMGa flux was too high and had to be reduced to prevent Ga accumulation. Since there is an overabundance of gallium, the growth is apparently limited by the amount of nitrogen delivered from thermal decomposition of the ammonia flux on the hot growth substrate. Ammonia flow is maximized near 200 sccm. Higher flow rates of ammonia begin to affect the pumping capacity of the TMP to maintain a low growth pressure. With 200 sccm of ammonia flow, chamber pressures reach approximately $1x10^{-5}$ torr as measured by the RGA during growth. This is still in the molecular flow regime but is the upper limit of desirable pressures. This led to a need to use other means to reduce the Ga flow to increase the V-III ratio of precursors.

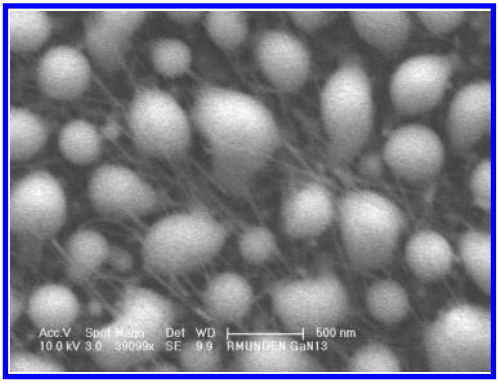

Figure 14. Another GaN growth shows liquid gallium droplets covering the substrate, but nanowires growing inbetween the drops.

The second round of growth comprising GaN17 through GaN23 was based on reducing the TMGa flux using source pulsing to control total delivery. This concept makes use of a modulated run-vent valve configuration. A low, but steady flow is set on the MFC through the vent valve, usually around 6 sccm. The computer control is then used to open and close the run valve, allowing approximately half of the flow through the run valve into the growth chamber, then diverting all flow back to the vent. The on-off cycle times can be controlled to obtain the desired duty-cycle, to achieve, on average, a lower total flux of TMGa to the substrate. With this technique the average flow can be set to a higher precision than allowed by the MFC alone. Flow rates below 6 sccm can also be obtained. By throttling flow rates of TMGa back to around 1 sccm, combining with 200 sccm of ammonia flow, and pushing up growth temperatures to promote ammonia cracking, high yield nanowires were regularly obtained across several growths using slight variations of the growth parameters. The very high density of the nanowire growth and the absence of either gallium droplets or polycrystalline nanocauliflower indicated reaching the desired growth regime. SEM investigation of the nanowires (Figure 15) shows the wires grow very dense and around 2 microns in length. In this image the nanowires were brushed over by a tweezer allowing them to be seen more easily. The nanowires appear to be very straight and to be growing in a relatively aligned way. Closer inspection of nanowires near the edge of the growth substrate provides more information. A polycrystalline nucleation layer appears to be present in some regions. Nanowire length can be determined more accurately, about 2.5 microns. The GaN growth shown in Figure 15 produced wires with diameters of about 30 nm.

Despite the growth of these, apparently good, nanowires, detailed examination by SEM of the nanowires grown on the amorphous alumina substrate reveal nanowires with noticeable diameter modulation (Figure 16). In these nanowires the diameter varies from about 150 nm to as little as 35 nm over a length scale of only 20-30 nm. Although not irrefutable, this seems to indicate that the pulsing of the TMGa source may be affecting the nanowire morphology; the growing nanowires are actually influenced by the short times without TMGa

flux. This effect was also only dominant on the alumina substrate, when viewed in the SEM, so initially it was thought to be confined to the alumina substrate.

Closer inspection via TEM, (Figure 17 and Figure 18), however, showed that even the nanowires grown on the sapphire substrate that appeared straight in the FE-SEM actually consisted of core structures full of stacking faults, where each segment of the crystal can have a different diameter. The bands of the stacking faults are most evident in Figure 17, but Figure 18 also shows that nanowires can have a more disordered core with diameter variations that are surrounded and somewhat smoothed by an outer amorphous layer, likely GaO. The tip of the nanowire, shown via TEM in Figure 18, clearly shows a thick (~20 nm) amorphous layer coating the nanowire and preventing the inner core variations from affecting the surface. This is what made the diameter modulation of the nanowires more difficult to detect in FE-SEM except in the most pronounced case of those nanowires grown on the alumina substrate.

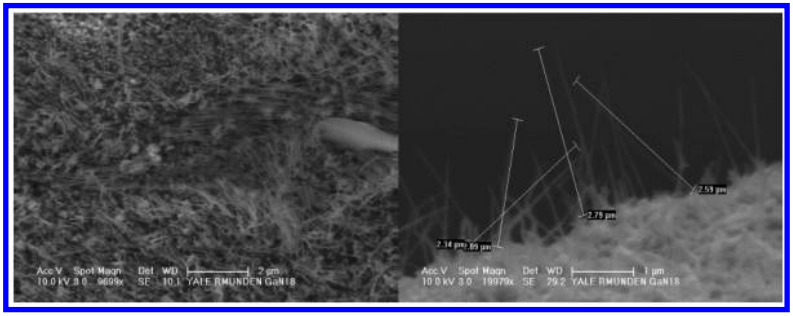

Figure 15. GaN SEM micrograph shows very dense growth of nanowires(NW). NWs were brushed over by a tweezer while loading the sample into the SEM, exposing the length of the wires, approximately 2 um (right). Nanowires near edge (left). These wires also show some tendency toward alignment.

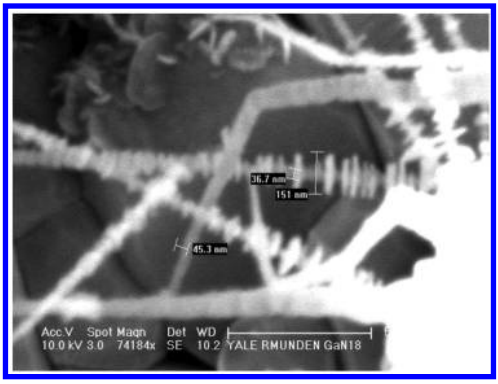

Figure 16. GaN nanowires grown on alumina show dramatic modulation of diameter along the length of the nanowire, perhaps due to fluctuations in source arrival or temperature variations. Diameter varies from ~150 nm to only ~35 nm.

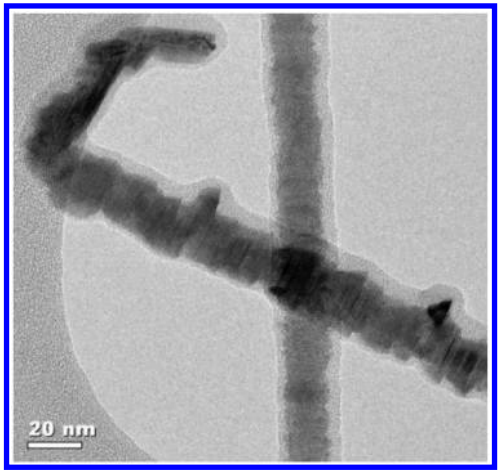

Figure 17. TEM micrograph of GaN nanowire. While not as dramatically modulated, TEM shows that the nanowires which seem more uniform actually suffer from many stacking faults. The structure looks like a series of discs of slightly different sizes stacked together.

The fact that the nanowires grown on crystalline substrates also showed the diameter variations discounted the idea that the amorphous nature of the alumina substrate was the cause, although it may have exacerbated the effect. This led to the recognition that the substrates were likely not reaching the requisite growth temperatures to provide enough surface mobility to the gallium atoms to allow them to properly recrystallize. This was a suspected problem because the substrate was still being heated by a resistive heater coil. This heater had to couple most of the energy into the substrate via infrared radiation due to the vacuum and the lack of intimate contact between the heater and the substrates. There was also often a great deal of difference in the temperatures reported by the thermocouple in the heater and the temperature reported on the pyrometer. The latter was often much higher, leading us to believe that the substrate was very transparent to the emitted radiation, and thus very inefficient at absorbing the energy to heat the substrate.

The nanowires of one growth were electrically contacted via an optical lithography method and were measured using the methods as described in Munden (*60*). Unfortunately, these results only served to confirm the poor quality of the nanowires. Although some nanowires were indeed making contact (verified by subsequent SEM imaging), none made good electrical contact. This was not surprising given the thick oxide and prevalence of stacking faults.

This difficulty provided motivation for improving the substrate heater to enable growth at temperatures nearer 900 °C. It was at this point in the development of the CBE processes that a change was made to use a lamp heating system with a silicon wafer as a susceptor, to concentrate the heat on the growth substrates. Implementation of the lamp immediately allowed for higher temperatures, as well as to have a substrate (the silicon) with known emissivity characteristics. This made optical pyrometry a more accurate way to measure the growth temperature, which generally could reach the target temperature without

problem. It was hoped that higher growth temperatures would enhance surface mobility of the adatoms (free, mobile atoms on the surface) and improve crystal quality even with the pulsed precursor supply.

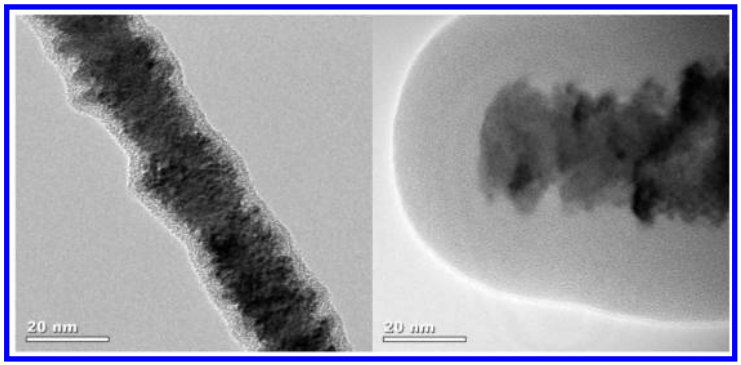

Figure 18. TEM also shows GaN nanowires that in the SEM appear straight can have a more amorphous structure, and a 20 nm thick amorphous, likely GaO, coating on the surface of the nanowires (left). The tip (right) appears to be free of catalyst, hinting that perhaps these nanowires are grown self-catalyzed from Ga droplets, instead of the deposited metal catalyst.

Upon inspection in the SEM, it was immediately noticeable that the nanowires grew very well aligned to the substrate, particularly the GaN-film substrates shown in Figure 19. These nanowires are observed to grow very densely packed and are generally vertically aligned out of the c-plane [0 0 0 1] GaN-film substrate, indicating c-direction growth of the nanowire. The density of nanowires makes it difficult to isolate individual nanowires, but they generally have 1.5 micron maximum length and 20 – 30nm diameters.

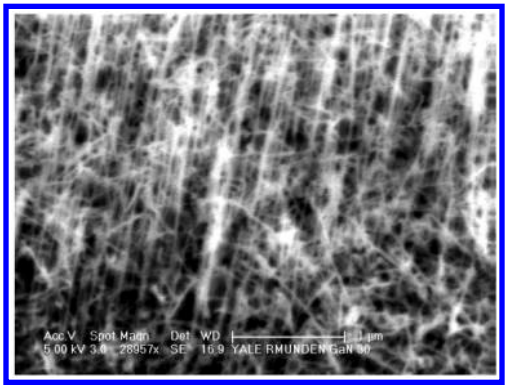

Figure 19. SEM micrographs of later growths on GaN film substrates that show very dense growth of nanowires aligned to the underlying substrate. Nanowires grow vertically aligned to c-plan GaN surface.

The nanowires located at the edge of the growth substrate are even more indicative of the crystalline alignment to the substrate. At the edge of the growth region nanowires can be seen growing aligned to different m-planes [1 0 -1 0] exposed at the edge of the GaN-film (Figure 20). This can be seen by the 60˚ angle between crossing nanowires in Figure 20. Edge nanowires can also be seen to have an average length of 1.5 microns. Despite many experiments, with times ranging from 3 – 5 hours, it was not possible to achieve high-yield of long nanowires. It appears that the density of the nanowires is interfering with the growth of nearest neighbors. It becomes easier to self-nucleate a new nanowire than it is for the Ga adatoms to move along another nanowire to increase its length. This competition is similar to that observed in the arsenide system (*64*).

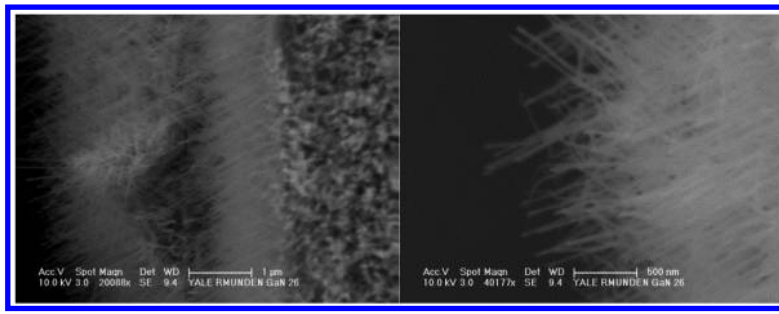

Figure 20. GaN26 nanowires grown on GaN films near the edges of the film show alignment to the m-planes of the GaN exposed near the edges of the film. This is indicated by the approximately 120˚ crossing angle of nanowires growing in different orientations (left). A closer view (right).

Finally, the initial results of TEM imaging of the nanowires from the post light heated growth run (Figure 21) show that the morphology and internal crystallinity appear to be much improved from the second round of growths. Although there is still an amorphous layer coating the surface, it is thinner (less than 10 nm in most areas). Also, the core structure, while not perfectly straight, shows far less evidence of the extreme stacking faults visible in the earlier GaN growth (Figure 17). This nanowire shows very little banding and shows a much more uniform diameter (approximately 40 nm). These results provide favorable evidence that the growth process in the CBE using the halogen lamp as a substrate heater provides enough energy to the group III Ga atoms to recrystallize much closer to a single crystal along the length of the nanowires. This provides hope that the electrical characteristics will be far superior to earlier growths. Successful fabrication of electrical nanowire FET devices from these later growth conditions has not yet been achieved, but it will require electron beam lithography (e-beam) methods (described in section 3.2.2 of Munden (*60*)) due to their very short length, which makes them prohibitively difficult to contact using optical lithography methods. E-beam lithography requires prepatterning a substrate with fiducial (or registration) marks. After depositing the short nanowires on the substrate each individual nanowire must be located relative to the fiducial marks using FE-SEM. After locating each nanowire, a pattern must be created to form metallic contacts

to each nanowire. This is a serial, and very slow, process. Whereas optical lithography can contact many wires at once, but only when they are long enough to regularly cross the 1 micron minimum gap between leads acheiveable with optical contact lithography.

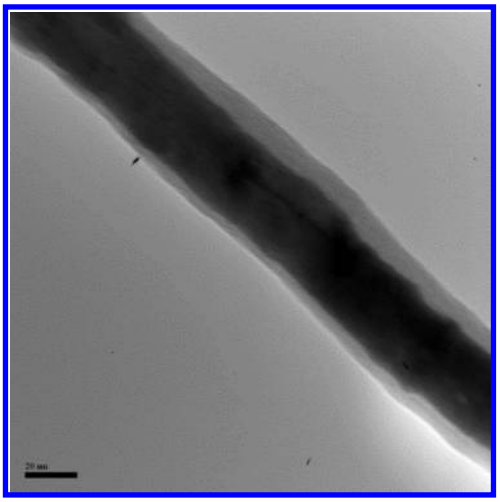

Figure 21. TEM studies of these straighter, aligned nanowires shows they have much more uniform internal structure (far less stacking faults) and somewhat more uniform diameter. There is still an amorphous (likely GaO) coating, though only a few nanometers thick. This nanowire is approximately 40 nm in diameter.

Conclusion

There are promising results from the growth of nanowires via CBE methods in the literature. The growth of GaN via CBE with ammonia and TMGa precursors is improving, but is dominated by self-catalyzed growth of nanowires, and limited by the low thermal cracking rate of ammonia, which severely limits the range of V-III ratios accessible in the reactor. Due to the generally higher volatility of the group V compounds, the V-III ratio is typically very high in III-V nanowire and thin film growth. The high temperatures necessary to achieve ammonia cracking are too high to grow nanowires by the traditional VLS method. GaN nanowires grown via CVD methods nearer thermal equilibrium allow for greater cracking of the ammonia, due to longer dwell times in the growth reactor, and larger surface areas to impinge upon. In the CBE process, under high vacuum, operation occurs within the mean free path distance, whereby ammonia molecules only collide at the substrate, and must crack and adsorb onto the surface immediately, or else remain volatile and be evacuated from the chamber. In addition, the gallium is too mobile at these temperatures, and is able to self-catalyze nanowires more efficiently than the catalyst driven growth, as evidenced by the lack of metal catalyst tip in the TEM of the nanowire in Figure 18. This eliminates the ability to control precursor delivery and nanowire diameter via catalyst placement and material. While difficult to quantify in TEM studies to date, there are likely many

faults or Nitrogen vacancies present which reduce the quality of these nanowires, due to poor availability of nitrogen during the growth process. Future work will require either adoption of a nitrogen source with a lower cracking temperature, such as hydrazine, and/or implementation of push-gas based delivery system to sufficiently dilute the TMGa, to increase the V-III flow ratios.

As the quality of GaN nanowire processing improves, it will be possible to explore expanded capabilities that will capitalize on the high vacuum growth environment. Specifically growth of heterostructures based on GaN could be pursued. The high-vacuum environment of CBE has been shown to be very effective at acheiving high quality heterostructured nanowires. The gas phase precursors are quickly evacuated, and abrupt transitions in materials composition become possible in the CBE system (*24*). Work remains to be done to achieve similar results in the GaN material system via CBE.

References

1. Reinhoudt, D. N.; Crego-Calama, M. *Science* **2002**, *295*, 2403–2407.
2. Schon, J. H.; Meng, H.; Bao, Z. N. *Science* **2001**, *294*, 2138–2140.
3. Huang, Y.; Duan, X. F.; Cui, Y.; Lauhon, L. J.; Kim, K. H.; Lieber, C. M. *Science* **2001**, *294*, 1313–1317.
4. Fleming, J. G.; Lin, S. Y.; El-Kady, I.; Biswas, R.; Ho, K. M. *Nature* **2002**, *417*, 52–55.
5. Noda, S.; Yokoyama, M.; Imada, M.; Chutinan, A.; Mochizuki, M. *Science* **2001**, *293*, 1123–1125.
6. Xia, Y. N.; Yang, P. D.; Sun, Y. G.; Wu, Y. Y.; Mayers, B.; Gates, B.; Yin, Y. D.; Kim, F.; Yan, Y. Q. *Adv. Mater.* **2003**, *15*, 353–389.
7. Wu, Y.; Fan, R.; Yang, P. *Nano Lett* **.2002**, *2*, 83–86.
8. Lauhon, L. J.; Gudiksen, M. S.; Wang, C. L.; Lieber, C. M. *Nature* **2002**, *420*, 57–61.
9. Fuhrer, M. S.; Nygard, J.; Shih, L.; Forero, M.; Yoon, Y. G.; Mazzoni, M. S. C.; Choi, H. J.; Ihm, J.; Louie, S. G.; Zettl, A.; McEuen, P. L. *Science* **2000**, *288*, 494–497.
10. Duan, X. F.; Huang, Y.; Cui, Y.; Wang, J. F.; Lieber, C. M. *Nature* **2001**, *409*, 66–69.
11. Zhong, Z. H.; Fang, Y.; Lu, W.; Lieber, C. M. *Nano Lett.* **2005**, *5*, 1143–1146.
12. Huang, Y.; Duan, X. F.; Cui, Y.; Lieber, C. M. *Nano Lett.* **2002**, *2*, 101–104.
13. Gudiksen, M. S.; Lauhon, L. J.; Wang, J.; Smith, D. C.; Lieber, C. M. *Nature* **2002**, *415*, 617–620.
14. Cheng, G. S.; Kolmakov, A.; Zhang, Y. X.; Moskovits, M.; Munden, R.; Reed, M. A.; Wang, G. M.; Moses, D.; Zhang, J. P. *Appl. Phys. Lett.* **2003**, *83*, 1578–1580.
15. Valcarcel, V.; Souto, A.; Guitian, F. *Adv. Mater.* **1998**, *10*, 138–140.
16. Shi, W. S.; Zheng, Y. F.; Wang, N.; Lee, C. S.; Lee, S. T. *Adv. Mater.* **2001**, *13*, 591–594.
17. Duan, X. F.; Lieber, C. M. *Adv. Mater.* **2000**, *12*, 298–302.
18. Morales, A. M.; Lieber, C. M. *Science* **1998**, *279*, 208–211.

In The Science and Function of Nanomaterials: From Synthesis to Application; Harper-Leatherman, et al.;

19. Sacilotti, M.; Decobert, J.; Sik, H.; Post, G.; Dumas, C.; Viste, P.; Patriarche, G. *J. Cryst. Growth* **2004**, *272*, 198–203.
20. Liu, J. L.; Cai, S. J.; Jin, G. L.; Thomas, S. G.; Wang, K. L. *J. Cryst. Growth* **1999**, *200*, 106–111.
21. Ohlsson, B. J.; Bjork, M. T.; Magnusson, M. H.; Deppert, K.; Samuelson, L.; Wallenberg, L. R. *Appl. Phys.* **2001**, *79*, 3335–3337.
22. Borisenko, V. E.; Ossicini, S. *What is What in the Nanoworld: A Handbook on Nanoscience and Nanotechnology*; Wiley: Weinheim, 2008.
23. Park, Y. S.; Lee, S.-H.; Oh, J.-E.; Park, C.-M.; Kang, T.-W. *J. Cryst. Growth* **2005**, *282*, 313–319.
24. Ohlsson, B. J.; Bjork, M. T.; Persson, A. I.; Thelander, C.; Wallenberg, L. R.; Magnusson, M. H.; Deppert, K.; Samuelson, L. In *Growth and Characterization of GaAs and InAs Nano-Whiskers and InAs/GaAs Heterostructures*, Linz, Austria, July 23−27, 2001; pp 1126−1130.
25. Huang, M. H.; Mao, S.; Feick, H.; Yan, H. Q.; Wu, Y. Y.; Kind, H.; Weber, E.; Russo, R.; Yang, P. D. *Science* **2001**, *292*, 1897–1899.
26. Tatebayashi, J.; Lin, A.; Wong, P. S.; Hick, R. F.; Huffaker, D. L. *J Appl Phys* **2010**, *108*.
27. Tsakalakos, L. *Nanotechnology for Photovoltaics*; CRC Press: Hoboken, NJ, 2010.
28. LaPierre, R. R. *J. Appl. Phys.* **2011**, *110*.
29. Tian, B. Z.; Lieber, C. M. *Pure Appl. Chem.* **2011**, *83*, 2153–2169.
30. Bu, S.; Li, X.; Wen, L.; Zeng, X.; Zhao, Y.; Wang, W.; Wang, Y. *Appl. Phys. Lett.* **2013**, *102*, 031106–031106-031105.
31. Cui, Y.; Wei, Q. Q.; Park, H. K.; Lieber, C. M. *Science* **2001**, *293*, 1289–1292.
32. Stern, E.; Klemic, J. F.; Routenberg, D. A.; Wyrembak, P. N.; Turner-Evans, D. B.; Hamilton, A. D.; LaVan, D. A.; Fahmy, T. M.; Reed, M. A. *Nature* **2007**, *445*, 519–522.
33. Zhou, J.; Lao, C. S.; Gao, P.; Mai, W.; Hughes, W. L.; Deng, S. Z.; Xu, N. S.; Wang, Z. L. *Solid State Commun.* **2006**, *139*, 222–226.
34. Tay, A. B. H.; Thong, J. T. L. *Rev. Sci. Instrum.* **2004**, *75*, 3248–3255.
35. Qin, Y.; Wang, X.; Wang, Z. L. *Nature* **2008**, *451*, 809–813.
36. Wagner, R. S.; Ellis, W. C. *Trans. Metall. Soc. AIME* **1965**, *233*, 1053–1064.
37. Quitoriano, N. J.; Kamins, T. I. *J. Appl. Phys.* **2007**, *102*, 044311.
38. Quitoriano, N. J.; Kamins, T. I. *Nano Lett.* **2008**, *8*, 4410–4414.
39. Su, J. Metal-Organic Chemical Vapor Deposition Growth and Characterization of Gallium Nitride Nanostructures. Doctoral Dissertation, Yale University, New Haven, CT, 2005.
40. Seifert, W.; Borgström, M.; Deppert, K.; Dick, K. A.; Johansson, J.; Larsson, M. W.; Mårtensson, T.; Sköld, N.; Patrik, T.; Svensson, C.; Wacaser, B. A.; Reine Wallenberg, L.; Samuelson, L. *J. Cryst. Growth* **2004**, *272*, 211–220.
41. Givargizov, E. I. *J. Cryst. Growth* **1975**, *31*, 20–30.
42. Allen, J. E.; Hemesath, E. R.; Perea, D. E.; Lensch-Falk, J. L.; LiZ, Y; Yin, F.; Gass, M. H.; Wang, P.; Bleloch, A. L.; Palmer, R. E.; Lauhon, L. J. *Nat. Nano* **2008**, *3*, 168–173.

43. Cimpoiasu, E.; Stern, E.; Klie, R.; Munden, R. A.; Cheng, G.; Reed, M. A. *Nanotechnology* **2006**, *17*, 5735–5739.
44. Wagner, J. B.; Sköld, N.; Reine Wallenberg, L.; Samuelson, L. *J. Cryst. Growth* **2010**, *312*, 1755–1760.
45. Wacaser, B. A.; Dick, K. A.; Johansson, J.; Borgström, M. T.; Deppert, K.; Samuelson, L. *Adv. Mater.* **2009**, *21*, 153–165.
46. Dick, K. A. *Prog. Cryst. Growth Charact. Mater* **2008**, *54*, 138–173.
47. Wu, Y.; Yang, P. *J. Am. Chem. Soc.* **2001**, *123*, 3165–3166.
48. Chèze, C.; Geelhaar, L.; Trampert, A.; Brandt, O.; Riechert, H. *Nano Lett.* **2010**, *10*, 3426–3431.
49. Chèze, C.; Geelhaar, L.; Brandt, O.; Weber, W.; Riechert, H.; Münch, S.; Rothemund, R.; Reitzenstein, S.; Forchel, A.; Kehagias, T.; Komninou, P.; Dimitrakopulos, G.; Karakostas, T. *Nano Res.* **2010**, *3*, 528–536.
50. Fan, H. J.; Lee, W.; Hauschild, R.; Alexe, M.; Le Rhun, G.; Scholz, R.; Dadgar, A.; Nielsch, K.; Kalt, H.; Krost, A.; Zacharias, M.; Gosele, U. *Small* **2006**, *2*, 561–568.
51. Wagner, R. S.; Ellis, W. C. *Appl. Phys. Lett.* **1964**, *4*, 89.
52. Bootsma, G. A.; Gassen, H. J. *J. Cryst. Growth* **1971**, *10*, 223–234.
53. Westwater, J.; Gosain, D. P.; Tomiya, S.; Usui, S.; Ruda, H. *J. Vac. Sci. Technol., B* **1997**, *15*, 554–557.
54. Sunkara, M. K.; Sharma, S.; Miranda, R.; Lian, G.; Dickey, E. C. *Appl. Phys. Lett.* **2001**, *79*, 1546–1548.
55. Schubert, L.; Werner, P.; Zakharov, N. D.; Gerth, G.; Kolb, F. M.; Long, L.; Gosele, U.; Tan, T. Y. *Appl. Phys. Lett.* **2004**, *84*, 4968–4970.
56. Kolb, F. M.; Hofmeister, H.; Scholz, R.; Zacharias, M.; Gosele, U.; Ma, D. D.; Lee, S. T. *J. Electrochem. Soc.* **2004**, *151*, G472–G475.
57. Kamins, T. I.; Williams, R. S.; Hesjedal, T.; Harris, J. S. In *Chemically Vapor Deposited Si Nanowires Nucleated by Self-Assembled Ti Islands on Patterned and Unpatterned Si Substrates*, Linz, Austria, July 23−27, 2001; pp 995−998.
58. Wu, Y. Y.; Fan, R.; Yang, P. D. *Nano Lett.* **2002**, *2*, 83–86.
59. Duan, X.; Lieber, C. M. *J Am Chem Soc* **2000**, *122*, 188–189.
60. Munden, R. Semiconductor Nanowire Characterization and Growth. Dissertation, Yale University, New Haven, CT, 2014.
61. Jensen, L. E.; Bjork, M. T.; Jeppesen, S.; Persson, A. I.; Ohlsson, B. J.; Samuelson, L. *Nano Lett.* **2004**, *4*, 1961–1964.
62. Persson, A. Growth of Nanowires with Chemical Beam Epitaxy. Master‘ Thesis, Lund University, Lund, Sweden, 2004.
63. Foord, J. S.; Davies, G. J.; Tsang, W. T. *Chemical Beam Epitaxy and Related Techniques*; Wiley: New York, 1997; p xiv.
64. Persson, A. I.; Froberg, L. E.; Jeppesen, S.; Bjork, M. T.; Samuelson, L. *J. Appl. Phys.* **2007**, *101*, 034313–034316.

Chapter 3

Reversible Graphene Functionalization for Electronic Applications: A Review

Keith E. Whitener, Jr.*

NRC Postdoctoral Research Associate, Chemistry Division,
U.S. Naval Research Laboratory, Washington, DC 20375, United States
***E-mail: keith.whitener.ctr@nrl.navy.mil**

Covalent attachment of various functional groups to the surface of graphene is a straightforward way to modify its electronic properties. A considerable number of chemical reactions have been developed on graphene, most of which result in permanent modification of the structure of graphene. However, a subset of these reactions are reversible, so that the properties of pristine graphene can be restored. Reversibility of functionalization on graphene has important implications for device design and circuit patterning. Different functionalities change the electronic properties of graphene in different ways, and patterning pristine graphene in a functionalized graphene matrix yields devices with interesting electronic properties. In this review, we examine several partially and fully reversible graphene reactions and their effects on graphene's electronic properties. We also detail useful applications for these reversible reactions.

Introduction

The two-dimensional carbon allotrope graphene has generated significant excitement in the scientific community due to theoretical and experimental observations of its unique properties. In particular, the electronic structure and transport properties of graphene are remarkably sensitive to the presence of surface-physisorbed and chemisorbed dopants (*1*). This sensitivity is the basis for using graphene as an active substrate in chemical and biological sensors (*2*). The tunability of graphene's electronic structure through chemical means is also

In The Science and Function of Nanomaterials: From Synthesis to Application; Harper-Leatherman, et al.;

critically important in designing and constructing graphene electronic devices (*3*). In light of these considerations, there has recently been significant attention paid to the structural and electronic effects of various chemical modifications of graphene.

The superlative conductivity of graphene stems from its bonding network, namely that each carbon is sp^2-bonded to its three neighbors in a planar configuration. As a result of this bonding scheme, each carbon center contributes one electron in its out-of-plane p orbital to the π-valence band and the π*-conduction band of the graphene lattice. The electrons in the π and π* bands are delocalized over the entire graphene lattice, allowing them to respond with minimal resistance to a potential difference (*4*). This strong two-dimensional ordering has observable effects in bulk graphite as well, as crystalline graphite is twice as conductive in the direction parallel to the individual graphene planes as it is in the perpendicular direction (*5*). This high conductivity is in contrast to the insulating property of diamond, where each carbon is sp^3-bonded to its neighbor in a tetrahedral configuration. Interestingly, this observation has implications for the electronic properties of covalently functionalized graphene. Since a covalent bond to the basal plane of a graphene sheet converts an sp^2 carbon center to an sp^3 carbon center, it breaks up graphene's delocalized π band structure and acts as a scattering center in the graphene lattice. Thus, the functionalization of graphene typically leads to an observable decrease in conductivity of the sheet.

Graphene is quite chemically inert when compared with other commonly encountered surfaces, a feature which can be exploited. For instance, graphene has been examined as a corrosion inhibitor on various surfaces, although with mixed results (*6*). In addition, many groups are using graphene as a barrier for trapping gases and other molecules (*7*). While graphene's resistance to chemical attack can be an asset, for researchers wanting to alter the chemistry of graphene, its low chemical reactivity must be overcome. Fortunately, the past decade has seen numerous advances of chemistry on graphene (*8*). Many of these chemical reactions are extensible. For example, the oxidation of graphene decorates the basal plane and edges with hydroxyl and carboxyl groups, which in turn allows further extension of graphene chemistry by exploiting the reactivity of these groups to yield other functionalities, *e.g.*, esters and amides (*9*). This feature renders graphene particularly flexible as a chemically active substrate, and makes it an attractive material for a wide variety of applications, from polymer composites (*10*) to chemical catalysis (*11*), and even to DNA transfection in cells (*12*).

Many applications of functionalized graphene depend upon the graphene reaction being at least partially reversible. A major area where this is important is in the exfoliation of graphite to graphene. A common technique is to chemically functionalize bulk crystalline graphite and then decouple the individual graphene sheets from one another, generally using sonication or some other mechanical means. Once the individual exfoliated sheets are obtained, pristine graphene is then restored by removing the functional groups. The success of this endeavor depends principally on the extent of reversibility of the functionalization reaction (*13*). A more intriguing use of reversibility in graphene functionalization occurs in applications involving heterostructures, where it is desirable that

one part of a device possess electronic properties unique to pristine graphene while another part of the device is decorated with functional groups, e.g., in lithographically patterned functionalized graphene (*14*, *15*). Since functionalized and unfunctionalized graphene often have different electronic properties, it is possible to selectively defunctionalize some areas of functionalized graphene, while leaving other areas functionalized, creating patterns of electrically active thin-film carbon. In fact, this has been achieved on several substrates using electron-beam lithography (*14*) as well as thermochemical nanolithography (*16*). The ability to pattern structures with different electronic properties in graphene materials is a promising breakthrough on the road to building electronic functional devices from graphene.

In this review, we will examine several chemical reactions on graphene in terms of their effects on graphene's electronic structure, their reversibility, and the degree to which they can be extended into various applications. In particular, we will examine various methods of oxidation, hydrogenation, and halogenation as simple reversible graphene chemical frameworks. We will also discuss more complex reactions, including the Diels-Alder reactivity of graphene as well as using graphene as a ligand in organometallic reactions.

Bulk Oxidation

One of the oldest and most important graphene reactions is oxidation, dating back over 150 years to Brodie's work on graphite oxidation (*17*). Before continuing any further, it is worthwhile to clarify some terminology used throughout this section. We use the term "graphite oxide" to refer to the bulk product resulting from the oxidation of crystalline graphite. Graphite oxide displays a lamellar structure similar to graphite. The term "graphene oxide" will refer to individual sheets of graphite oxide and will be abbreviated GO. Currently, graphite is oxidized using a method first developed by Hummers and Offeman (*18*) who reacted bulk graphite with sulfuric acid and permanganate anion to obtain highly functionalized graphite oxide. At the end of this reaction, the graphene basal plane bears several different oxygen functional groups, including hydroxyls, epoxides, ketones, and edge ethers and carboxylic acids. These polar groups allow graphite oxide to be dispersed easily in water or methanol, where it separates upon sonication into individual GO sheets which can subsequently be used to coat a surface with a thin film. Notably, the thin GO films retain the wide variety of functional groups of the isolated sheets enabling them to be further reacted with other molecules. For instance, the edge carboxyl groups lend themselves readily to amidation and esterification, and the epoxy groups on the basal plane can undergo ring-opening reactions to graft other nucleophiles to the surface of the graphene (*9*). This extensibility explains a significant portion of GO's popularity as a functional carbon material.

Monolayer GO differs from graphene in its low optical density and low conductivity. Much of the chararacter of graphene can be restored by treating it with a strong reducing agent such as hydrazine to yield a reasonably conductive material (*19*). However, oxidation of graphene is not fully reversible. The

In The Science and Function of Nanomaterials: From Synthesis to Application; Harper-Leatherman, et al.;

product of GO reduction has only a fraction of the conductivity of pristine graphene, and it differs from pristine graphene spectroscopically as well, to the extent that many researchers refer to the resultant material as "reduced graphene oxide" (rGO) instead of graphene (*20*). Historically, graphite oxidation has been a promising route to graphene isolation because of the ease of the oxidation reaction and separation of the material into individual sheets. The fact that the reaction is not completely reversible complicates some lines of research, in particular any application that requires that the material possess the superlative electronic properties of pristine graphene. For this reason, most of the research into the application of graphene as a revolutionary electronic material focuses on graphene obtained by methods other than GO reduction. However, a number of chemistries on graphene have now been developed that exhibit a larger degree of reversibility than the bulk oxidation and reduction of graphite.

Epoxidation

While epoxidation occurs during the course of the Hummers graphite oxidation, it is accompanied by several other reactions that complicate the study of one type of functional group. Fortunately, other methods have been developed to efficiently produce epoxides without producing large amounts of other functionalities, allowing researchers to study this particular functionalization in detail. Aside from the importance of examining a simplified GO system such as epoxidized graphene from a basic research standpoint, epoxidation also holds promise for applications, namely by tunably altering graphene's electronic properties vis-à-vis conductivity and doping levels. The oxygen groups break up the sp^2 network of bonding, lowering the conductivity of graphene, while simultaneously pulling electron density from the graphene material, which leaves the graphene p-doped. These two properties are important for building complex circuits using graphene.

Two significant methods currently exist for graphene epoxidation: one global and one local. Global epoxidation—that is, epoxidation that occurs across the entire sheet of graphene—can be achieved by exposing graphene to a low energy plasma of atomic oxygen (*21*). This has the advantage of covering large surface areas, but this advantage comes with a price. Even under the mildest conditions, exposure of graphene to atomic oxygen leads to removal of carbon from the graphene basal plane (etching) and therefore irreversible damage to the graphene (*22*).

The second method of graphene epoxidation was developed in the Hersam group at Northwestern (*23*). It uses a heated scanning tunneling microscope (STM) tip to crack oxygen gas into atomic oxygen under ultrahigh vacuum. This atomic oxygen then reacts with graphene in the same way as the aforementioned plasma-produced atomic oxygen. The critical difference is that the atomic oxygen is produced only in the immediate vicinity of the STM tip. This approach confers two advantages over oxygen plasma processing of graphene. First, because of the extremely low density of atomic oxygen in the processing chamber, the likelihood of creating many permanent crystal lattice defects in the graphene is

In The Science and Function of Nanomaterials: From Synthesis to Application; Harper-Leatherman, et al.;

far lower than exposure of the full graphene sheet to an atomic oxygen plasma. Second, the atomic oxygen is produced and consumed directly at the STM tip, giving particularly good local control over which areas of the graphene sheet are epoxidized and which areas remain pristine. Moreover, because the STM tip method of producing epoxidized graphene results in less permanent damage to the graphene sheet, it is readily reversible to recover pristine graphene, as shown in Figure 1.

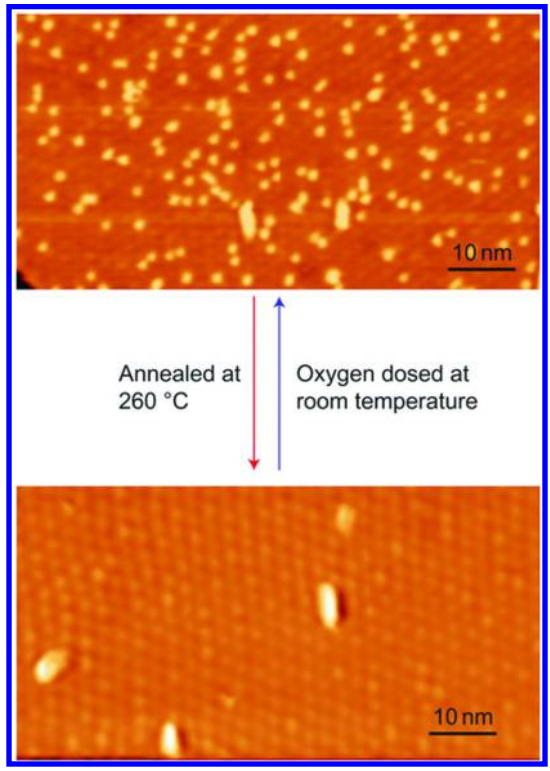

Figure 1. STM images of graphene that has been epoxidized with locally generated atomic oxygen (top) and thermally annealed to recover pristine graphene (bottom). The small bright dots in the top figure inidicate epoxide oxygens protruding from the graphene surface. (Adapted with permission from Macmillan Publishers Ltd: Nature Chemistry, reference (23), Copyright 2012.)

Halogenation

Bulk graphite undergoes fluorination at elevated temperatures in an atmosphere of pure fluorine. This material can be exfoliated by liquid-phase sonication and spin-coated or drop-cast onto a surface, similar to GO (*24*). The fluorinated graphene can then be reduced, typically using a silane or metal-acid, to give reduced graphene fluoride. This material, like rGO, is conductive but has properties that differ considerably from those of pristine graphene (*25*).

Recently, several groups have made progress on the fluorination of individual graphene sheets. Robinson *et al.* used xenon difluoride at room temperature to fluorinate single-layer graphene for incorporation into devices (*26*). Ruoff *et al*. could create patterned fluorinated graphene by depositing a fluoropolymer on the graphene surface and selectively irradiating it with a laser to dissociate fluorine radicals and fluorinate the underlying graphene (*27*). Sun *et al*. used an SF_6 plasma to produce fluorine radicals for reaction with graphene (*28*). In all cases, reversibility of the reaction was observed. In fact, using the XeF_2 method, graphene on a silicon oxide support overfluorinates to nearly stoichiometric levels (between CF and C_2F), but then rapidly defluorinates until it reaches a stable configuration closer to C_8F. Reactivity studies on this material indicate that two distinct species of fluorine are present on the surface of graphene: one species which is weakly bound—possibly only physisorbed—and which is steadily lost over time, and another species which is clearly covalently bound and which participates directly in the substitution chemistry of graphene fluoride (*29*).

The more strongly bound fluorines can be removed using standard chemical reduction or by thermal reduction. However, restoration of pristine graphene is incomplete. X-ray photoelectron spectroscopy reveals that fluorine is readily lost during chemical or thermal reduction, but Raman spectroscopy reveals that defect density remains high in the restored material. In addition, conductivity in the reduced material is restored only incompletely, to within roughly 3 times its initial value (*26*).

Despite its incomplete reversibility, fluorination of graphene is noteworthy for several reasons. For one, fluorine is extremely electronegative, and the carbon-fluorine bond is quite polar. It follows that areas of graphene fluoride act as strongly p-doped wide-band semiconductors, and that juxtaposing graphene fluoride with unfunctionalized graphene will withdraw negative charge carriers from the graphene, leaving the material p-doped (*15*). Thus graphene fluoride can serve as a tunable dopant for adjacent graphene channels. Secondly, the covalently bonded fluorine can be replaced with other nucleophiles in subsequent reactions. For instance, if graphene fluoride is immersed in neat ethylenediamine with a small amount of pyridine catalyst for a few hours at elevated temperatures, nearly all the fluorine is replaced by amine groups, forming a dense self-assembled monolayer that can participate in further reactions (*30*). For these reasons, graphene fluoride is an important graphene-based system.

In addition to fluorination, chlorination has also been reported on graphene using either chlorine plasma (*31*) or chlorine gas dissociated with UV light (*32*, *33*). Both pathways are presumably mediated by the generation of chlorine radicals and their subsequent reaction with graphene. The reaction is similar to fluorination in that a high chlorine content (30 at. %) can be obtained and the material shows efficient p-doping of the graphene. The reaction is also reversible upon application of heat, but conductivity results are anomalous.

It appears that chlorine has two bonding motifs to graphene (Figure 2): one where the chlorine is covalently bonded and introduces resistive sp^3 scattering centers into the graphene sheet, and another where the chlorine is bonded through a non-covalent mechanism (possibly a charge-transfer complex) which effectively p-dopes the graphene without disturbing the conductivity of the sheet. DFT

studies of the chlorination pathway suggest that chlorine radicals undergo charge transfer upon encountering a graphene sheet. This bonding mode predominates at low Cl concentrations, whereas at higher concentrations, covalent bonding and physisorption are favored. Physisorbed chlorine is more energetically favorable than covalent bonding, but physisorbed chlorine recombines to Cl_2 gas and escapes easily, leaving behind covalently bound chlorine on graphene as the predominant form at higher concentrations (*34*).

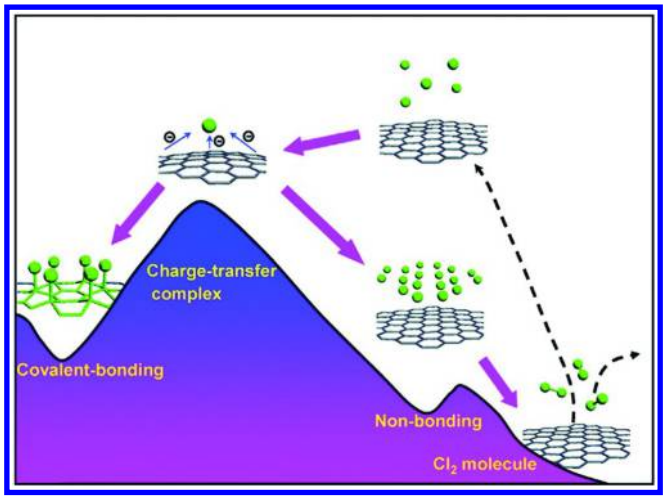

Figure 2. Schematic of the different bonding motifs of chlorine to graphene, including covalent bonding and charge-transfer complex formation. (Reprinted with permission from reference (34). Copyright (2012) American Chemical Society.)

There are scattered reports of reaction with bromine and iodine. Bromination of arc-evaporated graphene via UV irradiation and sonication has been reported at low levels (4 at. %) (*33*), and iodine can intercalate between the layers of few-layer graphene (*35*). However, these species are predicted to be unstable (*36*). This assertion is corroborated by the observation that iodine can effectively reduce graphene fluoride by first substituting the fluorines with iodines, and then decomposing into graphene and iodine (*37*).

Hydrogenation

Hydrogenation is perhaps the cleanest method to reversibly functionalize graphene. Several methods exist for hydrogenating graphene. The oldest method, and the one most extensively used in the electronics community, is plasma hydrogenation, where graphene is exposed to a low energy plasma of atomic

In The Science and Function of Nanomaterials: From Synthesis to Application; Harper-Leatherman, et al.;

hydrogen (*38*). This method has the advantage of being clean, with no exposure of the graphene to wet chemistry, but it requires specialized equipment to carry out, and the resistivity of the hydrogenated graphene sheet can be reversibly increased by only roughly 100-fold, from R_{sheet} ~ 1kΩ/square to R_{sheet} ~ 100kΩ/square, before the plasma begins to etch the carbon basal plane irreversibly (*39*). A word about the unit convention of Ω/square for sheet resistivity: Specific resistivity of a bulk 3D material is measured in units of Ω·cm, and therefore the sheet resistivity per unit length of a uniform thickness 2D conductor is rendered as Ω·cm/cm. If one naively cancels the length units to give Ω as the standard unit, then sheet resistivity (an intensive property of 2D systems) has the same units as bulk resistance (an extensive property), which can lead to confusion. By denoting sheet resistivity units as Ω/square, this ambiguity is avoided.

It is also possible to hydrogenate graphene via a number of different chemical routes. Notable among these is the Birch reduction, which employs alkali metal dissolved in liquid ammonia to reduce graphene to a strongly negatively charged species. Quenching the reaction mixture with a proton donor such as an alcohol or water gives highly hydrogenated graphene (*40–42*). In our own lab, we have shown that single-layer graphene that has been hydrogenated via the Birch reduction can be nearly completely restored to pristine graphene (*43*).

Birch hydrogenation of single-layer graphene causes a reversible >10^7-fold change in conductivity of the graphene sheet. Upon simple heating of the material at 300°C for 2 hours under argon gas, the sheet conductivity of the hydrogenated material is restored to within 30% of its original value (Figure 3). This indicates that very few permanent defects are introduced into the graphene lattice during the hydrogenation process. We have also found that hydrogenation offers a straightforward way to produce n-doped graphene. As most reversible reactions on graphene produce some variety of p-doped material, the synthesis of n-doped material in a facile and reversible manner greatly expands the possibilities for constructing active electronic devices (*43*).

Another important feature of reduction of graphene via dissolving metal in ammonia is that it is extensible to groups other than simple hydrogen. Several groups have shown that graphene and other carbonaceous materials can be alkylated by quenching the Birch reduction with alkyl halides instead of proton donors (*44*, *45*). Furthermore, in our lab we have shown that quenching the reaction with tributyltin chloride is an effective method for attaching stannyl groups to the surface of the graphene (*43*). As the tin moiety has a lower electronegativity than the carbon in the graphene sheet, it can be expected to n-dope the graphene even more heavily than hydrogen functionalization. The flexibility of chemically n- and p-doping graphene can be used in applications such as graphene diodes and transistors. Examination of the electronic properties and reversibility of these reactions is still underway, but the fact that these reactions occur at all gives a sense of the versatility of this type of chemistry.

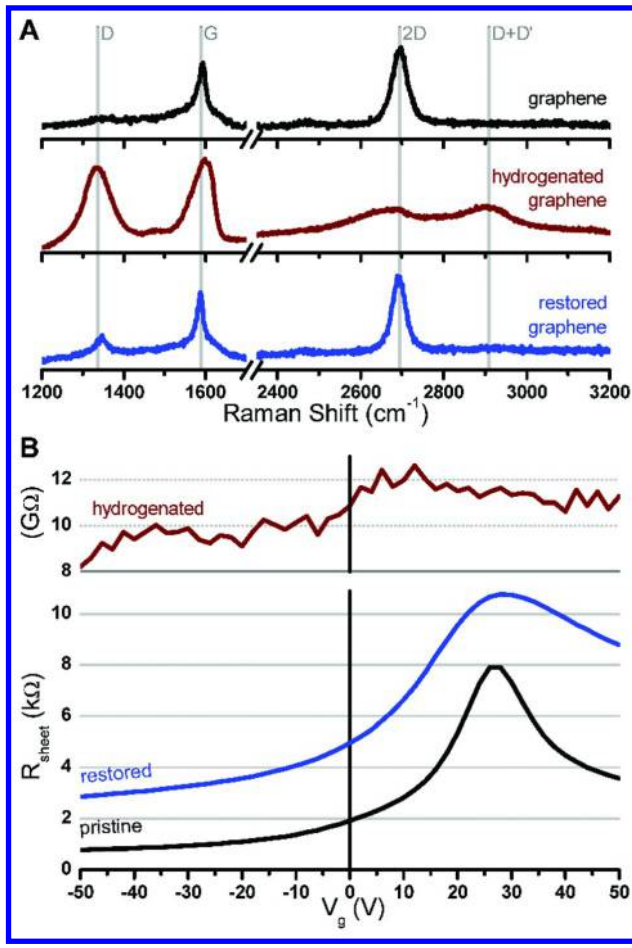

Figure 3. A) Raman spectra and B) FET electronic measurements of graphene (black curves), Birch hydrogenated graphene (red curves), and thermally restored graphene (blue curves), showing the spectroscopic and electronic effects of hydrogenation and subsequent restoration of graphene. (Reprinted from reference (43), Copyright (2014) with permission from Elsevier.)

Other Methods

So far, we have discussed the reversibility of reactions on graphene with respect to relatively simple, monatomic functional groups. However, many other chemical reactions have been developed on graphene. In this section, we mention two of these reactions, notable in that they are both quite easily reversible. They are the Diels-Alder reaction and exchange of ligands in an organometallic complex. Both reactions were developed in the Haddon research group (*46*, *47*).

The Diels-Alder reaction is a remarkable ring-forming reaction that has a long history in synthetic chemistry, as well as being conceptually important to the development of frontier molecular orbital theory in physical organic chemistry.

The reaction is a concerted, pericyclic reaction that occurs between a diene and an alkene, known as a dienophile, which results in the formation of a six-membered ring, (Scheme 1). In a normal Diels-Alder reaction, the highest-occupied molecular orbital (HOMO) of the diene and the lowest-unoccupied molecular orbital (LUMO) of the dienophile have the same symmetry, which allows for significant overlap and favorable energetics for bond formation (Figure 4).

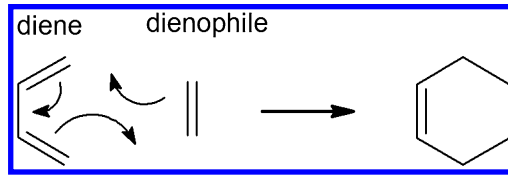

Scheme 1. Skeleton of a Diels-Alder reaction.

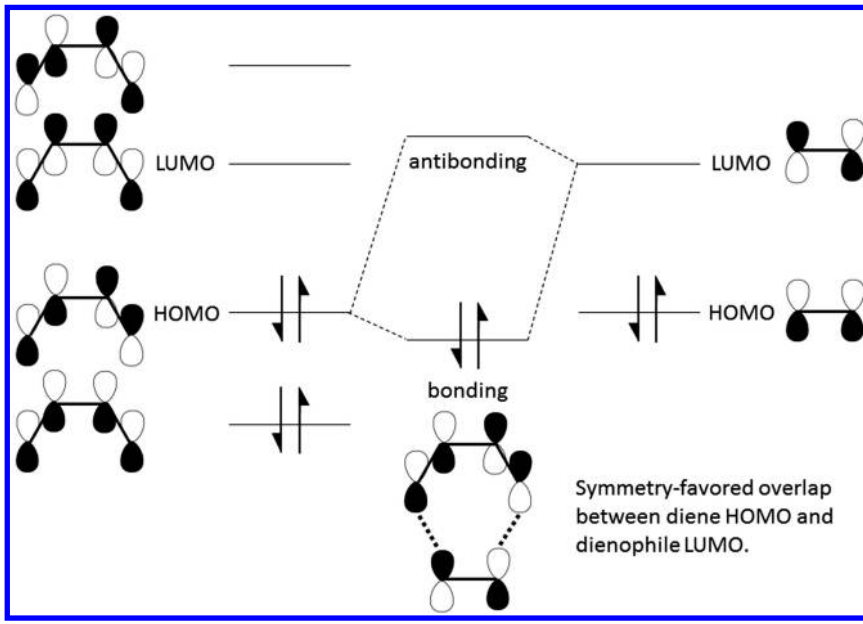

Figure 4. Frontier molecular orbital diagram showing how orbital symmetry mediates the Diels-Alder reaction.

In graphene, the HOMO and the LUMO are degenerate at the Dirac point, and so graphene can act as either the diene or the dienophile in the Diels-Alder reaction (*48*). In fact, Haddon *et al.* have shown evidence of graphite and graphene reacting with the dienophiles tetracyanoethylene (TCNE) and maleic anhydride (MA), as well as the dienes 9-methylanthracene (9MA) and 2,3-dimethoxy-1,3-butadiene (DMBD) (*46*). As presented in Figure 5, conductivity studies show that reaction of epitaxial graphene on silicon carbide with DMBD at 50°C causes a twofold increase in resistance, indicating that the reaction introduces sp^3 scattering centers into the ballistically conductive sp^2 graphene lattice. Raman spectroscopy

corroborates the presence of defects in reactions of graphene with all the reagents mentioned above. Furthermore, the Diels-Alder reaction on graphene is thermally reversible both when graphene acts as a diene and when graphene acts as a dienophile. Simple heating of the graphene in a nonreactive solvent completely recovers pristine graphene. Computational studies of the process indicate that cycloaddition occurs primarily at edge defects of the graphene (*49*). Since the side groups of dienes and dienophiles can be rationally chosen, the Diels-Alder reaction provides a potentially powerful method for reversibly attaching a wide variety of organic functional groups to graphene, and then removing them when they are no longer needed.

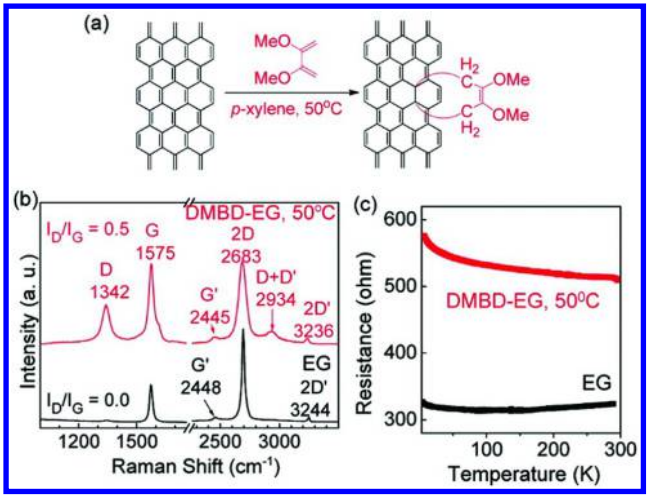

Figure 5. Scheme of Diels-Alder reaction of graphene with DMBD. (b) Raman spectra of pristine epitaxial graphene (bottom) and Diels-Alder functionalized graphene (top), showing the growth of the defect D peak at 1342 cm^{-1}. (c) Conductivity measurements of graphene (bottom) and functionalized graphene (top). (Reprinted with permission from reference (26). Copyright (2011) American Chemical Society.)

The second reaction of note is the ligand substitution reaction of various zero-valent chromium complexes. Chromium(0) is d^6, so its ligands must provide 12 electrons to satisfy the 18-electron rule and fill the metal's valence shell. The sandwich compound bis(benzene)chromium fulfills this rule by bonding chromium to two benzene ligands through η^6 haptic bonds, each providing six electrons. It is conceptually appealing to imagine replacing one of the benzene rings with a six-membered ring on a graphene sheet; however, the Cr-benzene bonds are actually quite strong and therefore, the substitution of a benzene ligand with graphene is not feasible. Haddon *et al.* circumvented this problem by employing chromium compounds with more labile ligands than η^6-benzene (*47*). In particular, they used chromium hexacarbonyl and benzene(chromium)tricarbonyl, exploiting the weak bond between CO and chromium to promote the substitution of three carbon monoxide ligands with

In The Science and Function of Nanomaterials: From Synthesis to Application; Harper-Leatherman, et al.;

graphene. In addition, by heating the chromium-functionalized graphene in mesitylene for an extended period of time, they could decomplex the chromium from the graphene, restoring it to a pristine state. These hexahapto structures are predicted theoretically to alter graphene's electronic structure significantly without upsetting its planar geometry, allowing for heavy doping without destroying the ballistic nature of the conductivity of graphene (*50*). Spin polarization in these systems could also lead to development of a graphene-mediated spin valve (*51*).

Conclusion

The reversible chemistry of graphene has developed rapidly in the past few years. While simple, partially reversible chemistries such as Hummers method oxidation and fluorination were the first to be explored in depth, newer chemistries, including locally directed epoxidation as well as Birch hydrogenation, have been developed which are completely reversible, allowing for the development of devices where restoration of graphene is key for exploitation of its unique electronic properties. In addition, exciting new chemistries in the form of Diels-Alder chemistry and organometallic haptic ligand substitution represent reactions that are not only reversible, but are also extensible to a wide variety of functionalities. All of these reactions will be important to the future development of various applications of graphene, including electronics with novel doping characteristics and sensing devices with high specificity.

References

1. Schedin, F.; Geim, A. K.; Morozov, S. V.; Hill, E. W.; Blake, P.; Katsnelson, M. I.; Novoselov, K. S. *Nat. Mater.* **2007**, *6*, 652–655.
2. Kuila, T.; Bose, S.; Khanra, P.; Mishra, A. K.; Kim, N. H.; Lee, J. H. *Biosens. Bioelectron.* **2011**, *26*, 4637–4648.
3. Geim, A. K.; Novoselov, K. S. *Nat. Mater.* **2007**, *6*, 183–191.
4. Rao, C. N. R.; Sood, A. K.; Subrahmanyam, K. S.; Govindaraj, A. *Angew. Chem., Int. Ed.* **2009**, *48*, 7752–7777.
5. Goetz, A.; Holser, A. *J. Electrochem. Soc.* **1942**, *82*, 391–396.
6. Prasai, D.; Tuberquia, J. C.; Harl, R. R.; Jennings, G. K.; Bolotin, K. I. *ACS Nano.* **2012**, *6*, 1102–1108.
7. Bunch, J. S.; Verbridge, S. S.; Alden, J. S.; van der Zande, A. M.; Parpia, J. M.; Craighead, H. G.; McEuen, P. L. *Nano Lett.* **2008**, *8*, 2458–2462.
8. Kuila, T.; Bose, S.; Mishra, A. K.; Khanra, P.; Kim, N. H.; Lee, J. H. *Prog. Mater. Sci.* **2012**, *57*, 1061–1105.
9. Dreyer, D. R.; Park, S.; Bielawski, C. W.; Ruoff, R. S. *Chem. Soc. Rev.* **2010**, *39*, 228–240.
10. Kuila, T.; Bhadra, S.; Yao, D.; Kim, N. H.; Bose, S.; Lee, J. H. *Prog. Polym. Sci.* **2010**, *35*, 1350–1375.
11. Dreyer, D. R.; Jia, H.-P.; Bielawski, C. W. *Angew. Chem., Int. Ed.* **2010**, *49*, 6813–6816.
12. Feng, L.; Zhang, S.; Liu, Z. *Nanoscale* **2011**, *3*, 1252–1257.

13. Whitener, K. E., Jr; Sheehan, P. E. *Diamond Relat. Mater.* **2014**, *46*, 25–34.
14. Steven, E. M.; Withers, F.; Dubois, M.; Craciun, M. F.; Russo, S. *New J. Phys.* **2013**, *15*, 033024.
15. Lee, W.-K.; Robinson, J. T.; Gunlycke, D.; Stine, R. R.; Tamanaha, C. R.; King, W. P.; Sheehan, P. E. *Nano Lett.* **2011**, *11*, 5461–5464.
16. Wei, Z.; Wang, D.; Kim, S.; Kim, S.-Y.; Hu, Y.; Yakes, M. K.; Laracuente, A. R.; Dai, Z.; Marder, S. R.; Berger, C.; King, W. P.; de Heer, W. A.; Sheehan, P. E.; Riedo, E. *Science* **2010**, *328*, 1373–1376.
17. Brodie, B. C. *Phil. Trans. R. Soc. London* **1859**, *149*, 249–259.
18. Hummers, W. S.; Offeman, R. E. *J. Am. Chem. Soc.* **1958**, *80*, 1339.
19. Stankovich, S.; Dikin, D. A.; Piner, R. D.; Kohlhaas, K. A.; Kleinhammes, A.; Jia, Y.; Wu, Y.; Nguyen, S. T.; Ruoff, R. S. *Carbon* **2007**, *45*, 1558–1565.
20. Pei, S.; Cheng, H.-M. *Carbon* **2012**, *50*, 3210–3228.
21. Barinov, A.; Malcioğlu, O. B.; Fabris, S.; Sun, T.; Gregoratti, L.; Dalmiglio, M.; Kiskinova, M. *J. Phys. Chem. C* **2009**, *113*, 9009–9013.
22. Johns, J. E.; Hersam, M. C. *Acc. Chem. Res.* **2012**, *46*, 77–86.
23. Hossain, M. Z.; Johns, J. E.; Bevan, K. H.; Karmel, H. J.; Liang, Y. T.; Yoshimoto, S.; Mukai, K.; Koitaya, T.; Yoshinobu, J.; Kawai, M.; Lear, A. M.; Kesmodel, L. L.; Tait, S. L.; Hersam, M. C. *Nat. Chem.* **2012**, *4*, 305–309.
24. Bourlinos, A. B.; Bakandritsos, A.; Liaros, N.; Couris, S.; Safarova, K.; Otyepka, M.; Zbořil, R. *Chem. Phys. Lett.* **2012**, *543*, 101–105.
25. Bourlinos, A. B.; Safarova, K.; Siskova, K.; Zbořil, R. *Carbon* **2012**, *50*, 1425–1428.
26. Robinson, J. T.; Burgess, J. S.; Junkermeier, C. E.; Badescu, S. C.; Reinecke, T. L.; Perkins, F. K.; Zalalutdniov, M. K.; Baldwin, J. W.; Culbertson, J. C.; Sheehan, P. E.; Snow, E. S. *Nano Lett.* **2010**, *10*, 3001–3005.
27. Lee, W. H.; Suk, J. W.; Chou, H.; Lee, J.; Hao, Y.; Wu, Y.; Piner, R.; Akinwande, D.; Kim, K. S.; Ruoff, R. S. *Nano Lett.* **2012**, *12*, 2374–2378.
28. Yang, H.; Chen, M.; Zhou, H.; Qiu, C.; Hu, L.; Yu, F.; Chu, W.; Sun, S.; Sun, L. *J. Phys. Chem. C* **2011**, *115*, 16844–16848.
29. Stine, R.; Lee, W.-K.; Whitener, K. E.; Robinson, J. T.; Sheehan, P. E. *Nano Lett.* **2013**, *13*, 4311–4316.
30. Stine, R.; Ciszek, J. W.; Barlow, D. E.; Lee, W.-K.; Robinson, J. T.; Sheehan, P. E. *Langmuir* **2012**, *28*, 7957–7961.
31. Wu, J.; Xie, L.; Li, Y.; Wang, H.; Ouyang, Y.; Guo, J.; Dai, H. *J. Am. Chem. Soc.* **2011**, *133*, 19668–19671.
32. Li, B.; Zhou, L.; Wu, D.; Peng, H.; Yan, K.; Zhou, Y.; Liu, Z. *ACS Nano.* **2011**, *5*, 5957–5961.
33. Gopalakrishnan, K.; Subrahmanyam, K. S.; Kumar, P.; Govindaraj, A.; Rao, C. N. R. *R. Soc. Chem. Adv.* **2012**, *2*, 1605–1608.
34. Yang, M.; Zhou, L.; Wang, J.; Liu, Z.; Liu, Z. *J. Phys. Chem. C* **2011**, *116*, 844–850.
35. Kalita, G.; Wakita, K.; Takahashi, M.; Umeno, M. *J. Mater. Chem.* **2011**, *21*, 15209–15213.

36. Karlický, F.; Zbořil, R.; Otyepka, M. *J. Chem. Phys.* **2012**, *137*, 034709.
37. Zbořil, R.; Karlický, F.; Bourlinos, A. B.; Steriotis, T. A.; Stubos, A. K.; Georgakilas, V.; Šafářová, K.; Jančík, D.; Trapalis, C.; Otyepka, M. *Small* **2010**, *6*, 2885–2891.
38. Elias, D. C.; Nair, R. R.; Mohiuddin, T. M. G.; Morozov, S. V.; Blake, P.; Halsall, M. P.; Ferrari, A. C.; Boukhvalov, D. W.; Katsnelson, M. I.; Geim, A. K.; Novoselov, K. S. *Science* **2009**, *323*, 610–613.
39. Burgess, J. S.; Matis, B. R.; Robinson, J. T.; Bulat, F. A.; Perkins, F. K.; Houston, B. H.; Baldwin, J. W. *Carbon* **2011**, *49*, 4420–4426.
40. Yang, Z. Q.; Sun, Y. Q.; Alemany, L. B.; Narayanan, T. N.; Billups, W. E. *J. Am. Chem. Soc.* **2012**, *134*, 18689–18694.
41. Pekker, S.; Salvetat, J. P.; Jakab, E.; Bonard, J. M.; Forro, L. *J. Phys. Chem. B* **2001**, *105*, 7938–7943.
42. Eng, A. Y. S.; Poh, H. L.; Sanek, F.; Marysko, M.; Matejkova, S.; Sofer, Z.; Pumera, M. *ACS Nano.* **2013**, *7*, 5930–5939.
43. Whitener, K. E., Jr; Lee, W. K.; Campbell, P. M.; Robinson, J. T.; Sheehan, P. E. *Carbon* **2014**, *72*, 348–353.
44. Englert, J. M.; Knirsch, K. C.; Dotzer, C.; Butz, B.; Hauke, F.; Spiecker, E.; Hirsch, A. *Chem. Commun.* **2012**, *48*, 5025–5027.
45. Sternberg, H. W.; Delle Donne, C. L. *Fuel* **1974**, *53*, 172–175.
46. Sarkar, S.; Bekyarova, E.; Niyogi, S.; Haddon, R. C. *J. Am. Chem. Soc.* **2011**, *133*, 3324–3327.
47. Sarkar, S.; Niyogi, S.; Bekyarova, E.; Haddon, R. C. *Chem. Sci.* **2011**, *2*, 1326–1333.
48. Sarkar, S.; Bekyarova, E.; Haddon, R. C. *Acc. Chem. Res.* **2012**, *45*, 673–682.
49. Cao, Y.; Osuna, S.; Liang, Y.; Haddon, R. C.; Houk, K. N. *J. Am. Chem. Soc.* **2013**, *135*, 17643–17649.
50. Dai, J.; Zhao, Y.; Wu, X.; Zeng, X. C.; Yang, J. *J. Phys. Chem. C* **2013**, *117*, 22156–22161.
51. Avdoshenko, S. M.; Ioffe, I. N.; Cuniberti, G.; Dunsch, L.; Popov, A. A. *ACS Nano.* **2011**, *5*, 9939–9949.

Chapter 4

Synthesis of Single-Walled Carbon Nanotube–Nanoparticle Hybrid Structures

Tirandai Hemraj-Benny*

Department of Chemistry, Queensborough Community College/CUNY, 222-05 56th Avenue, Bayside, New York 11364, United States
***E-mail: THemrajbenny@qcc.cuny.edu**

In this chapter, we explore chemical strategies for the functionalization of single-walled carbon nanotube (SWNT) surfaces with metal nanoparticles reported in the past decade. The preparation of SWNT-metal nanoparticle hybrid materials is an important research area as the new hybrid materials generated possess unique properties and are useful for various nanotechnological applications. These hybrids can be stabilized by covalent and/or noncovalent interactions. Although covalent interactions between the sidewalls, ends and defect sites of SWNTs and nanoparticles are reviewed, the main focus of this chapter is to provide a summary of recently synthesized SWNT-nanoparticle hybrids via noncovalent interactions.

Introduction

Nanomaterials are at the leading edge of the rapidly developing field of nanotechnology, while carbon nanotubes (CNTs) have become a model one-dimensional (1D) nanostructure of the nanoscale world. CNTs are considered a third allotropic form of carbon, with the others being graphite and diamond. CNTs consist of shells of sp^2-hybridized (trivalent) carbon atoms forming a hexagonal network that is itself arranged helically within the tubular motif (*1*). CNTs are observed in two distinct structural forms: a) single-walled nanotubes, ($0.7 < d < 2$ nm) consisting of a single layer of graphene sheet seamlessly rolled into a cylindrical tube, or b) multiwalled nanotubes, MWNTs, ($1.4 < d < 150$ nm) consisting of multiple concentric tubes separated by about 0.34 nm (*2*). Studies have shown that SWNTs offer superior electrical, mechnical and

In The Science and Function of Nanomaterials: From Synthesis to Application; Harper-Leatherman, et al.;

catalytic performance over MWNTs due to their smaller and more homogeneous diameter, higher surface area and lower defect densities (*3*). Their highly crystalline structure results in improved mechanical properties (*3–6*). Due to their remarkable thermal, electrical, mechanical and optical properties, SWNTs have shown enormous potential in applications as varied as sensing, gas storage, composites, catalyst support, molecular electronics, field emission displays, bioanalytical labeling, and drug delivery (*7*, *8*).

Many of the applications of SWNTs require uniform and stable dispersions. However, pristine SWNTs are insoluble in most organic solvents and aqueous solutions and tend to aggregate as a result of van der Waals interactions between individual tubes. Moreover, it is desirable to separate semiconducting from metallic nanotubes, as the electronic properties of SWNTs depend on their chirality and diameter (*9*). SWNTs can undergo surface chemical functionalization to enhance their solubility in various solvents and to produce novel hybrid materials potentially suitable for the above mentioned applications.

Among the abundant carbon nanotube chemistry developed in the past decade (*10*), the integration of one-dimensional carbon nanotubes with zero-dimensional nanoparticles into hybrid structures has received the most attention (*11*). These nanoparticle-nanotube hybrids often possess unique structural, electromagnetic, electrochemical, and other properties that are not available to the respective components alone, and thus, have been envisioned for many applications (*12*, *13*).

This review provides an overview of chemical modification strategies of SWNTs developed over the past decade to produce novel single-walled carbon nanotube−nanoparticle (SWNT-NP) hybrid structures. In general, SWNTs can be functionalized with nanoparticles by utilizing a) covalent interactions between chemical groups bonded to the ends and defects sites on the surface of the nanotube or b) noncovalent interactions with adsorption or wrapping of various functional molecules on the π-conjugated skeleton of the nanotube (Figure 1). In most cases that involve covalent functionalization of sidewalls or ends and defect sites, as well as noncovalent coordination functionalization, nanoparticles are prepared by a reduction-solution method utilizing a metal salt precursor and a reducing agent.

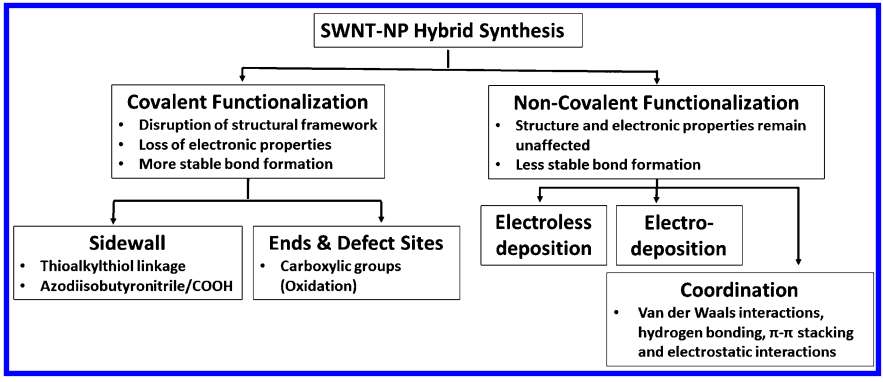

Figure 1. Overview scheme of the various methods of synthesizing single-walled carbon nanotube-metal nanoparticle (SWNT-NP) hybrids.

In The Science and Function of Nanomaterials: From Synthesis to Application; Harper-Leatherman, et al.;

Covalent Interactions

Sidewall

The chemical reactivity of SWNT sidewalls resulting in covalent bonds mainly arises from the π-orbital misalignment between adjacent carbons (*9*). Covalent sidewall derivatization usually results in the loss of the intrinsic electronic structure. The loss of conjugation and disruption of band structure is reflected in the loss of optical transitions between van Hove singularities in the electronic density of states (DOS) of nanotubes (*14*). This phenomenon can be observed in the UV-Vis-NIR data of these systems. In addition, Raman spectroscopy is effective at detecting the presence and extent of sidewall functionalization of SWNTs (*15*). The shape and intensity of a weak disorder mode peak (*D* band) at 1290-1320 cm^{-1} has been related to the extent of nanotube sidewall functionalization (*9*, *15*). In addition, the RBM features (the radial A_{1g} breathing mode) are dependent on the diameter of the tube that is brought into resonance. Using the formula ω_{RBM} $(cm^{-1}) = 238/d$ $(nm)^{0.93}$, the diameters (*d*) of the various tubes can be calculated, which can be identified as either semiconducting or metallic SWNTs (*16*).

Photolysis of cyclic disulfides with SWNTs produced thioalkylthiol linkages on the skeleton of the nanotubes, which were then used as substrates for the assembly of gold (Au) nanoparticles (*17*). Figure 2 shows a schematic of the chemical modification process. The metal salt precursor, $HAuCl_4$, and the reducing agent, sodium borohydride ($NaBH_4$), in the presence of boiling sodium citrate were used to initially prepare the gold nanoparticles. The gold nanoparticles were then attached to the surface of the thioalkylthiolated SWNTs by stirring overnight. Raman data confirmed covalent sidewall functionalization of the SWNTs by the increase in intensity of the *D*-band. Mid-IR data also confirmed the attachment of $–S(CH_2)_4SH$ to the C=C bonds of the SWNT sidewalls. Since there was no significant loss of the features denoted in the UV-Vis-NIR spectra, it was concluded that the SWNT sidewalls were not heavily modified.

Another example of sidewall functionalization was the recently reported attachment of platinum (Pt) nanoparticles to the sidewalls of SWNTs via covalently attached carboxylic groups (*3*). The sidewalls were first functionalized with azodiisobutyronitrile (AIBN) and subsequently treated with NaOH and HCl to yield terminal carboxylic groups. The SWNT-Pt NP hybrids were prepared by a microwave-assisted polyol method using ethylene glycol as the reducing agent and H_2PtCl_6 as the metal salt precursor. This hybrid material showed improved catalytic activity towards the oxidation of methanol and ethanol compared to platinum nanoparticles on carbon black.

In The Science and Function of Nanomaterials: From Synthesis to Application; Harper-Leatherman, et al.;

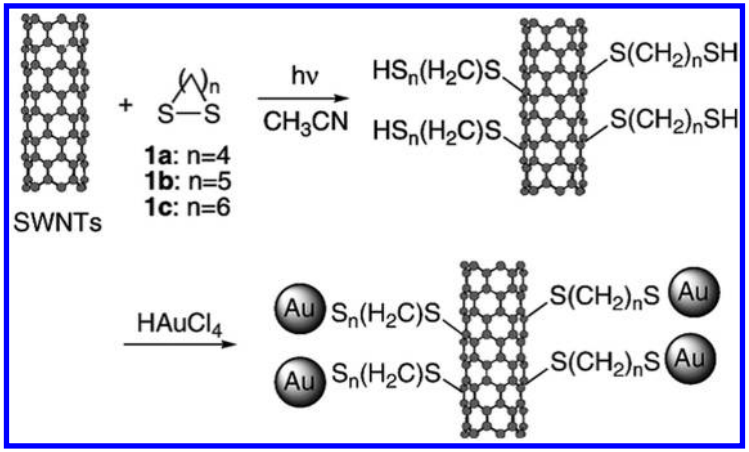

*Figure 2. Schematic representation of covalent sidewall functionalization of SWNTs with cyclic disulfides **1** and Au nanoparticles. (Reproduced with permission from reference (17). Copyright (2007) Elsevier B.V.)*

Ends and Defect Sites

The sidewalls of SWNTs contain defect sites such as pentagon-heptagon pairs called Stone-Waled defects, sp^3 hybridized defects, and vacancies in the nanotube lattice (*18*). Treatment with strong acids, such as nitric acid (*19*), oxygen gas (*9*) or other strong oxidizing agents, such as piranha solution (H_2SO_4 and H_2O_2 mixture) (*19*), facilitates the decoration of the ends and defect sites of the SWNT with oxygentated functional groups such as carboxylic acid.

Oxidized SWNTs are often used as stabilizing agents for the synthesis of metal nanoparticles, where metal salt reduction occurs in the prescence of the SWNTs. Carboxylic acid functionalized SWNTs were utilized as templates for anchoring palladium nanoparticles via thermolysis of palladium acetate under inert atmosphere without reducing agents (*20*). A one-pot synthesis method was used where the carboxylic acid functionalized SWNTs were present during the reduction of the metal salt. Figure 3 shows a schematic of the synthesis of SWNT-Pd NP hybrids. Carboxylic acid functionalized SWNTs and palladium acetate were heated at 95 ºC in dry DMF under nitrogen atmosphere for 4 hours. These SWNT-Pd NP composites proved to be an efficient recyclable catalyst for the acyl Sonogashira reaction.

In another case, it was determined that oxidized defects on sidewalls of SWNTs play an essential role as nucleation sites for gold nanoparticle formation and stabilization. Gold nanoparticles were attached to oxygenated groups which were produced on the surface of SWNTs by chemical oxidation utilizing nitric acid and piranha solution (*19*). The Au nanoparticles were formed by the reduction of $HAuCl_4$ under UV light irradiation in the presence of citric acid. There was loss of the van Hove singularity features for the oxidized SWNTs, where as the oxidized-SWNT-Au NP hybrid presented the same characteristic peaks as the starting unfunctionlized SWNTs. This effect suggests that electron-transfer from

In The Science and Function of Nanomaterials: From Synthesis to Application; Harper-Leatherman, et al.;

the particles to the tubes occurs, restoring the available electrons for optical transitions.

The synthesis of stable CdS nanoparticles on the oxygentated surface of SWNTs templated and stabilized by means of attached 1 → 3 C-branched amide-based dendrons was also reported (*21*). The dendron consisted of a branched tree-like arrangement of amino-polyester functionalities. $Cd(NO_3)_2 \cdot 4H_2O$ and Na_2S in methanol were used to synthesize CdS nanoparticles of about 1.4 nm. Separate Cd^{2+} and S^{2-} methanolic solutions were added to dendron functionalized SWNTs methanolic suspension at O°C. The mixture was then sonicated. It was determined that the SWNT-CdS NP hybrid exhibited reduced fluorescence emission intensity at 434 nm due to partial emission quenching by the SWNTs.

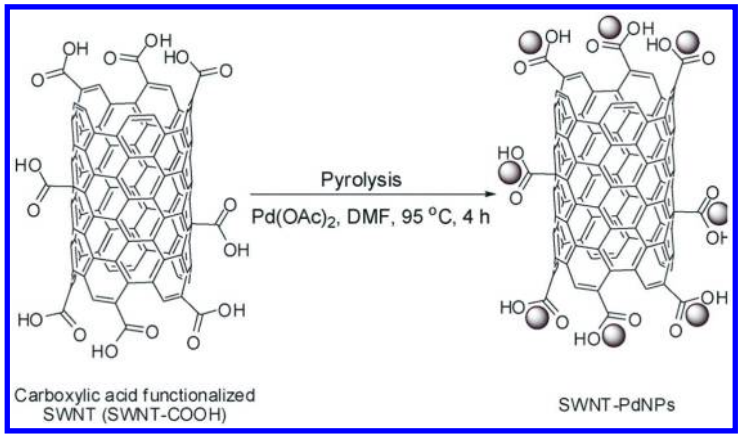

Figure 3. Schematic representation for the synthesis of SWNT-Pd nanoparticle hybrids by coordination of Pd-NPs to covalently attached carboxylic acid groups on the ends and defect sites of the nanotubes. (Reproduced with permission from reference (20). Copyright (2012) The Royal Society of Chemistry.)

The attachment of Ag nanoparticles onto defect sites of SWNTs was also reported (*22*). Initially, SWNTs were mixed in $SnCl_2$ and trifluoroacetic acid solution for 30 minutes, which resulted in electrophilic η^2coordination of Sn^{2+} ions on the surface of SWNTs. Defect sites in carbon nanotubes were selectively reactive with electropositive Sn^{2+} ions. Ag nanoparticles were then deposited on Sn-SWNTs via a redox reaction in ammoniacal $AgNO_3$ solution.

Others have reported the formation of SWNT-metal NP hybrids by mixing oxidized SWNTs and pre-synthesized nanoparticles. One example is the decoration of oxidized SWNTs with pyridine-protected CdSe nanoparticles (*23*). The SWNTs were heated in air at 350 °C and then treated with 5 M HCl. CdSe nanoparticles were synthesized by thermal treatment of CdO, trioctylphosphine oxide (TOPO), hexylphosphonic acid (HPA)/tetradecylphosphonic (TDPA) and selenium. Solutions of the SWNTs and NPs in pyridine were mixed and sonicated

In The Science and Function of Nanomaterials: From Synthesis to Application; Harper-Leatherman, et al.;

for 10 mins. The interaction between the SWNTs and the nanoparticles was proposed to be due to a) the binding of surface carboxylic groups on SWNT defect sites with the CdSe surface; and b) the π-π stacking interaction between SWNT sidewalls and the pyridine bound as a ligand to the nanoparticle surface.

Non-Covalent Interactions

Electroless Deposition

Qu *et al* (*24*) reported a substrate-enhanced electroless deposition (SEED) method for functionalization of SWNTs with various metal nanoparticles (Au, Pt, Pd). This was performed in the absence of any additional reducing agent by simply supporting the nanotubes on a metal substrate with a redox potential lower than that of the metal ions to be reduced into nanoparticles. Aqueous solutions of $HAuCl_4$, K_2PtCl_4 and $(NH_4)_2PdCl_4$ were used to obtain the metal nanoparticles (*24*). The same research group also employed the SEED method for the shape and size controlled syntheses of Pt and Au nanoparticles by varying the concentration and reaction time of the appropriate aqueous solutions with a copper foil via galvanic displacement (*25*).

Electrodeposition

For this technique, highly controlled functionalization of metal nanoparticles on SWNT ends and sidewalls can be achieved, where activators, such as carboxyl or hydroxyl groups, are not required. Quinn *et al* (*26*) demonstrated that noble metals can be equally electrodeposited on SWNT sidewalls and ends under direct potential control, where the nanotube acts as a nonsacrifical template for the deposited nanoparticles. Controlled particle size and surface coverage were obtained by varying the deposition potential, duration of the pulse and the concentrations of metal salts ($HAuCl_4$, K_2PtCl_4 and $(NH_4)_2PdCl_4$).

The decoration of SWNTs with different densities of Ag nanoparticles by changing the deposition time, the applied voltage and the location of carbon nanotubes with respect to the anode in a chemical and catalyst free environment was also reported (*27*). Figure 4 shows the schematic of the experimental setup and field emission scanning electron microscopy (FESEM) micrographs of the nanocrystal-nanotube hybrids. At low voltage, single Ag nanoparticles were successfully attached at the open ends of the nanotubes, whereas at high voltage, intermediate and full coverage densities of the Ag nanoparticles were observed. The newly fabricated SWNT-Ag nanoparticle hybrid was successfully used for label-free detection of ssDNA molecules.

It was also recently reported that SWNT-NP hybrids (Cu and Au NP) synthesized by galvanic displacement can improve the thermoelectric power factor of nanotubes (*28*). The thermoelectric power factor of carbon nanotubes can be improved by controlling their electrical conductance and thermopower. An efficient thermoelectric material, which can carry both charge and heat, requires high electrical conductivity and thermopower with low thermal conductivity. In galvanic displacement, metal ions in a solution are reduced on SWNTs by

In The Science and Function of Nanomaterials: From Synthesis to Application; Harper-Leatherman, et al.;

dissolving another metal whose reduction potential is smaller than that of the reduced metal. Dispersed SWNT, stabilized by sodium dodecyl benzene sulfonate (SDBS), were made into films and immersed in different concentrations of $CuSO_4$ or $HAuCl_4$ solution. Copper ions in solution were reduced on nanotubes by obtaining electrons from zinc electrodes since the reduction potential of zinc is lower than that of copper. Gold ions were reduced on nanotubes by silver counter electrodes and spontaneous reaction due to larger reduction potentials than those of nanotubes. It was reported that the transport properties of SWNTs can be considerably altered when decorated with Cu NPs resulting in a 2-fold improvement in the thermoelectric power factor with low metal ion concentration (1mM/30 minute reaction time). However, gold incorporation increased conductance of all samples with reduction in thermopower. When copper NPs are in contact with SWNTs, electrons are donated to the nanotubes, making them more n-type. However, gold NP incorporation makes SWNTs more p-type by withdrawing electrons from the nanotubes (*28*).

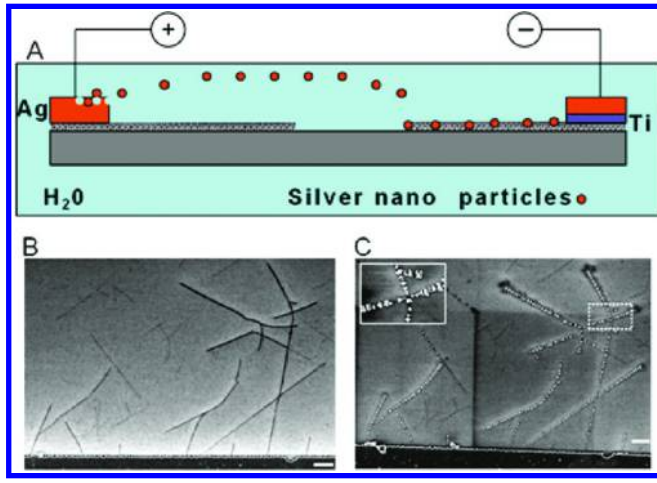

Figure 4. Electrodeposition of Ag nanoparticles onto SWNTs in a chemical and catalyst free environment. (A) Schematic representation of Ag nanoparticle attachment under an electric field. (B) FESEM micrographs representing the SWNTs network before and (C) after decoration with Ag nanoparticles. (Reproduced with permission from reference (27). Copyright (2011) American Chemical Society.)

In another report, gold nanoparticles were electrodeposited on the sidewalls of SWNTs, which had been functionalized with the amine-terminated ionic liquid 1-ethylamine-2,3-dimethylimimidazolium bromide (*29*). The electrodeposition was performed in an aqueous solution of Na_2SO_4 containing H_2SO_4 and $HAuCl_4 \cdot 4H_2O$. Glucose oxidase was further assembled onto the SWNT-Au NP composite through ionic interactions, and exhibited excellent electrocatalytic activity for the reduction of glucose.

Coordination

SWNT-nanoparticle hybrids synthesized by noncovalent coordination interactions have shown promising applications in optoelectronic devices (*12*, *30*, *31*), catalysis (*32–35*), solar cells (*36*), cancer therapy (*37*) and composite materials (*6*). In general, SWNTs sidewalls can be noncovalently functionalized with metal nanoparticles synthesized by solution-reduction methods and linked via aromatic compounds, surfactants, and polymers, which employ π-π stacking interactions.

Surfactants such as poly(styrene-alt-maleic acid) (PMSA) (*33*) have been used to better disperse SWNTs in solutions and act as templates for the binding of metal nanoparticles. For example, SWNT-Pt nanoparticle hybrids were synthesized by solution-phase reduction of Pt (2,2′:6′,2″-terpyridine)Cl_2 by $NaBH_4$ in the presence of PSMA (Figure 5) (*33*). It was proposed that the carbonyl groups on PSMA coordinated with the metal ions and acted as a capping reagent which prevented the subsequently formed nanoparticles from aggregating with each other.

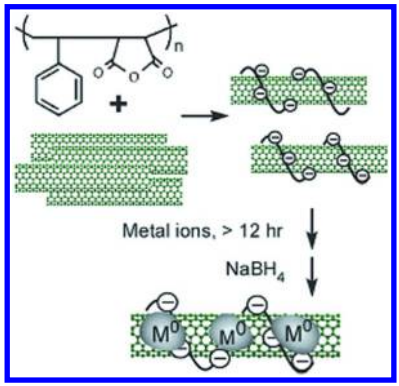

Figure 5. Schematic representation of the synthesis of SWNT-PSMA-Pt nanoparticle hybrid structure. (Reproduced with permission from reference (33). Copyright (2006) American Chemical Society.)

Other surfactants such as oleylamine and oleic acid were used to synthesize SWNT-CoPt nanoparticle systems by coordination in a one pot-synthesis method (*38*). Although oleylamine was essential for the formation of stable Pt alloy nanoparticles, addition of excess oleylamine (>0.15mmol) to a sample with a high coverage of nanoparticles resulted in spontaneous detachment of the nanoparticles from the nanotubes. CdS nanoparticles were also noncovalently coordinated to SWNTs via oleylamine (*31*). Figure 6 shows a schematic of the synthesis process. The CdS nanoparticles were first synthesized in a one-pot mixture of $CdCl_2$, sulfur and oleylamine. Thin-film photoswitches were fabricated using the resulting SWNT-CdS nanoparticle hybrids, which possess n-type enhanced conducting characteristics under illumination.

In other reports, polyaniline (PANI) was used to bridge Pt nanoparticles to SWNTs (*34*). The free electron pair on nitrogen in PANI interacts with the orbital of Pt to form a coordination complex, while the PANI aromatic groups link to

the surface of the SWNTs through π-π bonding. Figure 7 shows a schematic of this interaction. In a one-pot synthesis method, Pt nanoparticles were synthesized by ethanol reduction of H_2PtCl_6 in the presence of aniline and SWNT. Aniline is polymerized into conductive PANI by a protonic acid (HCl) and an oxidant ($NH_4S_2O_8$). It was proposed that the SWNT-Pt/PANI complex, having great electrochemical stability, can be used for fuel cells.

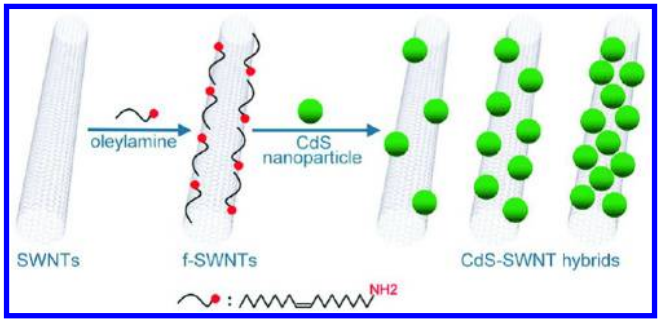

Figure 6. Schematic representation of noncovalent assembly of SWNT-CdS nanoparticles hybrids via oleylamine coordination. (Reproduced with permission from reference (31). Copyright (2010) American Chemical Society.)

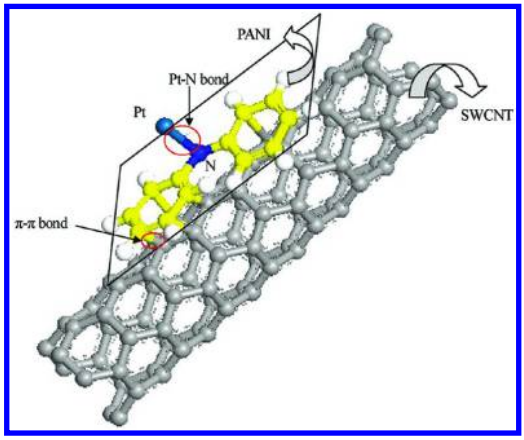

Figure 7. Schematic of molecular interaction of SWNT-Pt-PANI composite. (Reproduced with permission from reference (34). Copyright (2011) American Chemical Society.)

Enhancement in the electrocatalytic activity of Pt nanoparticles toward an oxygen-reduction reaction has been achieved by utilizing SWNT-Pt NP hybrids, which were synthesized via coordination with the copolymer Nafion (*32*). SWNTs were first mixed with a Nafion solution for one hour. Pt black powder was then added to this mixture, which was sonicated for 1 hour to yield the hybrid composites.

Yarns of SWNT-Pt NP have also been synthesized. A Pt-nanoparticle-adsorbed carbon nanotube yarn made by solution adsorption and yarn spinning processes was synthesized and used as the counter electrode in a TiO_2-based dye-sensitized fiber solar cell (*36*). Pt nanoparticles were first synthesized via the reduction of H_2PtCl_6 by ethylene glycol. SWNTs were added to Pt nanoparticle solution in ethylene glycol and were then spun into yarns.

SWNT-Palladium nanoparticle hybrids have also showed great potential for catalytic and sensor applications (*5*, *35*, *37*, *39*). We have recently reported a one-pot synthesis method for the coordination of Pd nanoparticles onto nonfunctionalized SWNTs via tris[3-(trimethoxysilyl)propyl] isocyanurate (TTPI) (*5*). Figure 8 shows the schematic representation of the synthesis of the SWNT-Pd nanoparticle hybrids. It was proposed that the TTPI hydrolyzes to form a Si-O-Si network on the SWNT surface, while the Pd nanoparticles coordinate to the carbonyl and the nitrogen functionalities of the isocyanurate ring. The synthesis of SWNT-Pd hybrids in the absence of TTPI was not possible, which confirms the importance of the TTPI in controlling the formation of the Pd nanoparticles. Capping agents prevent sintering of metal nanoparticles once the colloid is formed due to electrostatic interactions. High-Resolution Transmission Electron Microscopy (HR-TEM) images and Energy Dispersive X-ray Spectroscopy (EDS) spectra of the SWNT-Pd nanoparticle hybrids are represented in Figure 9

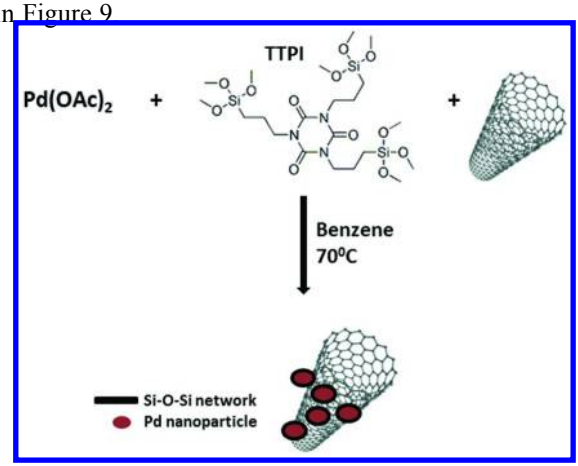

Figure 8. Schematic representation of the SWNT-Pd nanoparticle hybrid stabilized by coordination with TTPI as reported by reference (5).

Regarding the applications of such systems; SWNT-Pd nanoparticle hybrids fabricated by electrochemical post-treatment of Pd-based infinite coordinate polymers (ICP) have high electrocatalytic activity toward the oxidation of ethanol when compared with Pd/C catalyst (*35*). Pd nanoparticles deposited on SWNTs via N_2 reduction of $Pd(OAc)_2$ have served as a catalyst for the Heck reaction of styrene (*40*). H_2 sensors based on SWNTs with Pd and $Ni_{50}Pd_{50}$ nanoparticles have also been reported (*39*). These nanoparticles were first synthesized by reduction of Pd acetate and $NiSO_4 \cdot 6H_2O$ in ethylene glycol using polyvinylpyrrolidone (PVP) as the capping agent.

In The Science and Function of Nanomaterials: From Synthesis to Application; Harper-Leatherman, et al.;

Field-effect transistor (FET) devices were fabricated using pyrene-functionalized CdSe nanoparticles coordinated to SWNTs (*41*). The effective charge transfer from the pyrene/CdSe nanoparticles to the SWNTs in the hybrid shows promise for application in polymer heterojunction photovoltaic devices and solar cells.

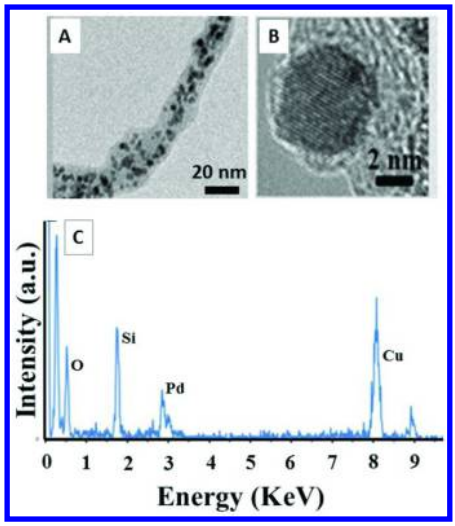

Figure 9. Top (A, B): HR-TEM images of SWNT-Pd nanoparticle-TTPI hybrid. Bottom (C): EDS spectrum indicating the presence of Pd and Si atoms. The Cu signal is from the sample grid.

Hybrids of semiconducting SWNTs and Au nanoparticles were achieved utilizing the coordination of a porphyrin-fluorene copolymer and were effectively used in a thin-film transistor (TFT) device (*30*). Pyridine-coated Au nanoparticles were first synthesized by a ligand exchange method utilizing tert-dodecanethiol-coated Au nanoparticles and 4-pyridineethanethiol. Separately, a SWNT-porphyrin-fluorene copolymer complex was created by sonication, which was then made into a film. A methanol solution of the pyridine coated Au NPs was spread onto the nanotube film and was then air-dried. The Au nanoparticles were connected to the SWNTs via coordination bonding between the pyridine-terminated nanoparticles and the zinc metal of the porphyrin on the copolymer. Raman spectroscopy data confirmed reactive selectivity for semiconducting (8,6) and (8,7) SWNTs .

"Golden" SWNTs were prepared by growing Au nanoparticles onto bilayer, polysaccharide-functionalized SWNTs (Figure 10) (*37*). The layer-by-layer self-assembly of two oppositely charged polysaccharides provided a surface with a high density of active metal binding groups such as amino and carboxylic acids. The SWNT-Au hybrids have good water dispersibilty and biocompatibility, and have been used to cause localized hyperthermia when taken up by the cells resulting in rapid cancer cell death.

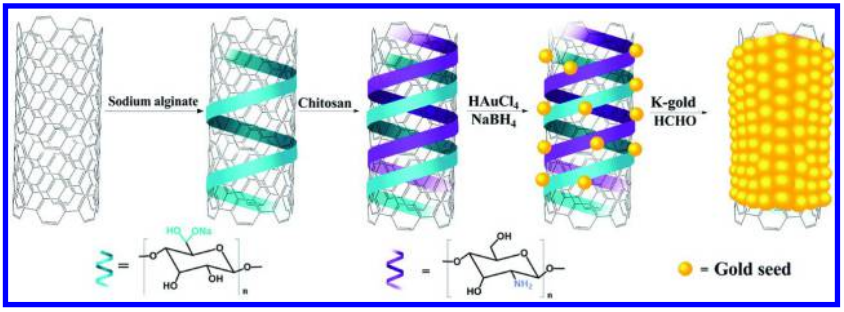

Figure 10. Schematic representation of the preparation process of a SWNT-Au hybrid via coordination with bilayer polysaccharides. (Reproduced with permission from reference (37). Copyright (2014) American Chemical Society.)

Recently, we have successfully synthesized SWNT-Mg nanoparticle hybrids for potential light-weight, high-strength applications (*6*). SWNTs reinforced with a uniform distribution of magnesium nanoparticles were synthesized by solution reduction using methylmagnesium chloride (MeMgCl) salt, a Grignard reagent, and lithium naphtalide (*6*). The SWNT-Mg nanoparticle hybrid was prepared in anhydrous tetrahydrofuran (THF) via lithium reduction of MeMgCl. Initially, a polyelectrolyte salt of the SWNTs was created by allowing the SWNTs to stir overnight in the presence of lithium metal and naphthalene (*42*). The naphthalene also served as an electron carrier to allow the reduction of Mg(II) to Mg(0). The Mg nanoparticles of an average size of 4.5±0.5 nm were uniformly dispersed on the surfaces of the SWNTs, as seen in Figure 11.

Raman spectroscopy data indicated distinct diameter selectivity of the coordination of the Mg NPs with the larger diameter metallic SWNTs of 2.21 nm. In addition, a degree of debundling of metallic nanotube bundles was noted upon the coordination of the magnesium nanoparticles. This debundling phenomena can be monitored by Raman spectroscopy (*15*). For metallic SWNTs, the band seen around 1535 cm^{-1} can be well fitted by a Breit-Wigner-Fano (BWF) line. This band results from coupling of phonons to the electronic continuum of the metallic tubes and can be used to distinguish between metallic and semiconducting tubes. It has been reported that a decrease in intensity of this feature, can be related to debundling of metallic tubes (*43*). And thus in our work, an observed significant decrease in intensity of this band feature for the Mg NP-SWNTs composites was attributed to the presence of the Mg nanoparticles causing a debundling effect of the nanotubes. The debundling effect may also be as a result of the initial reaction of the SWNTs with Li metal before the MeMgCl was added because Li metal facilitates debundling effects (*42*). An increase in dissolution was observed when SWNTs were stirred overnight with Li metal.

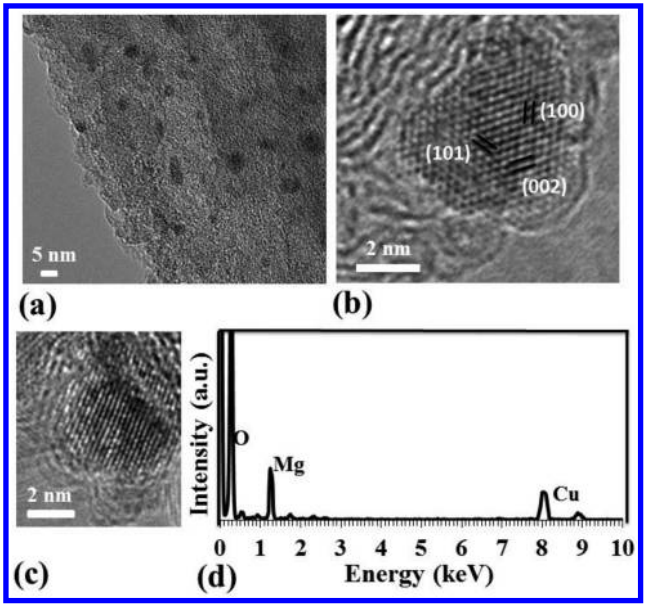

Figure 11. TEM micrographs of treated SWNTs. a) Image shows a uniform distribution of magnesium nanoparticles on the SWNTs with average particle sizes of 4.5 ± 0.5 nm. (b) and (c) show lattice fringes of the hexagonal metallic Mg nanoparticles. (d) EDS spectrum of treated SWNTs indicating the presence of Mg. The Cu signal originated from the TEM sample grid. (Reproduced with permission from reference (6). Copyright (2014) Elsevier B.V.)

Conclusion

Single walled carbon nanotube-metal nanoparticle hybrids have played an increasingly central role in the research, development, and application of nanotube-based systems. In this chapter, a brief description of recent progress in the preparation and application of these new hybrid materials synthesized by covalent interactions and noncovalent interactions is provided. Defect-site and covalent sidewall functionalization of SWNTs results in the change of carbon hybridization from sp^2 to sp^3, leading to partial loss of conjugation with consequences for electron-acceptor and/or electron-transport properties. Noncovalent functionalization results in the conservation of the SWNT electronic structure by preventing disruption of the intrinsic nanotube sp^2 structure and conjugation. However, the noncovalent interactions between SWNTs and nanoparticles are considerably less stable than covalent interactions.

In the past decade, there has been an increased number of reports from researchers in chemistry, physics, biology, materials, and engineering fields describing not only the synthesis of SWNT-NP hybrid structures, but also their incorporation into functional devices. The challenges of utilizing these SWNT-NP hybrids in electronic, composite and biological devices on a larger

scale include improving control of nanoparticle size, obtaining uniformity in SWNT length, diameter and chirality, and developing a better understanding of the biocompatibility of the hybrids.

Acknowledgments

I would like to thank Dr. David Sarno for helpful discussion and proofreading. Work performed in our lab was partially funded through a Professional Staff Congress of The City University of New York Grant (Award #66263-00 44).

References

1. Dresselhaus, M. S.; Dresselhaus, G.; Avouris, P. *Carbon Nanotubes: Synthesis, Structure, Properties, and Applications*; Berlin: Springer Verlag, 2001.
2. Guldi, D. M.; Martin, N. *Carbon Nanotubes and Related Structures: Synthesis, Characterization, Functionalization and Applications*; John Wiley & Sons, Inc.: New York, 2010.
3. Huang, M.; Dong, G.; Wu, C.; Guan, L. Preparation of highly dispersed Pt nanoparticles supported on single-walled carbon nanotubes by a microwave-assisted polyol method and their remarkably catalytic activity. *Int. J. Hydrogen Energy* **2014**, *39*, 4266–4273.
4. Ashrafi, B.; Guan, J.; Mirjalili, V.; Zhang, Y.; Chun, L.; Hubert, P.; Simard, B.; Kingston, C. T.; Bourne, O.; Johnston, A. Enhancement of mechanical performance of epoxy/carbon fiber laminate composites using single-walled carbon nanotubes. *Compos. Sci. Technol.* **2011**, *71*, 1569–1578.
5. Hemraj-Benny, T.; Chauhan, M.; Zhang, L.; Wong, C. K.; Singh, G.; Kim, E.; Ahn, E. Synthesis and characterization of novel hybrids of tris[3-(trimethoxysilyl)propyl] isocyanurate (TTPI) capped palladium nanoparticles and single-walled carbon nanotubes. *Silicon* **2011**, *3*, 97–101.
6. Hemraj-Benny, T.; Pigza, J. A.; Budhoo, S.; Condon, L.; Depner, S. W.; Dennis, R. V.; Banerjee, S. Synthesis of novel single-walled carbon nanotube-magnesium nanoparticle composites by a solution reduction method. *Mater. Lett.* **2014**, *117*, 305–308.
7. Eder, D. Carbon Nanotube-Inorganic Hybrids. *Chem. Rev.* **2010**, *110*, 1348–1385.
8. Park, T. J.; Banerjee, S.; Hemraj-Benny, T.; Wong, S. S. Purification strategies and purity visualization techniques for single-walled carbon nanotubes. *J. Mater. Chem.* **2006**, *16*, 141–154.
9. Banerjee, S.; Hemraj-Benny, T.; Wong, S. S. Covalent surface chemistry of single-walled carbon nanotubes. *Adv. Mater.* **2005**, *17*, 17–29.
10. Tasis, D.; Tagmatarchis, N.; Bianco, A.; Prato, M. Chemistry of carbon nanotubes. *Chem. Rev.* **2006**, *106*, 1105–1136.

11. Wildgoose, G. G.; Banks, C. E.; Compton, R. G. Metal nanoparticle and related materials supported on carbon nanotubes: methods and applications. *Small* **2006**, *2*, 182–193.
12. Zhao, Y.; Stoddart, J. F. Noncovalent functionalization of single-walled carbon nanotube. *Acc. Chem. Res.* **2009**, *42*, 1161–1171.
13. Zhang, Y.; Stucky, G. D. Heterostructured approches to efficient thermoelectric materials. *Chem. Mater.* **2014**, *26*, 837–848.
14. Hu, H.; Zhao, B.; Hamon, M. A.; Kamaras, K.; Itkis, M. E.; Haddon, R. C. Sidewall functionalization of single-walled carbon nanotubes by addition of dichlorocarbene. *J. Am. Chem. Soc* **2003**, *125*, 14893.
15. Dresselhaus, M. S.; Dresselhaus, G.; Saito, R.; Jorio, A. Raman spectroscopy of carbon nanotubes. *Phys. Rep.* **2005**, *409*, 47–99.
16. Hemraj-Benny, T.; Wong, S. S. Silylation of single-walled carbon nanotubes. *Chem. Mater.* **2006**, *18*, 4827–4839.
17. Nakamura, T.; Ohana, T.; Ishihara, M.; Hasegawa, M.; Koga, Y. Chemical modification of single-walled carbon nanotubes with sulfur-containing functionlities. *Diamond Relat. Mater.* **2007**, *16*, 1091–1094.
18. Hirsch, A. Functionalization of single-walled carbon nanotubes. *Angew. Chem., Int. Ed.* **2002**, *41*, 1853–9.
19. Quintana, M.; Ke, X.; Tendeloo, G. V.; Meneghetti, M.; Bittencourt, C.; Prato, M. Light-induced selective deposition of Au nanopaerticles on single-walled carbon nanotubes. *ACS Nano* **2010**, *4*, 6105–6113.
20. Santra, S.; Ranjan, P.; Bera, P.; Ghosh, P.; Mandal, S. K. Anchored palladium nanoparticles onto single-walled carbon nanotubes: Efficient recyclable catalyst for N-containing heterocycles. *RSC Adv.* **2012**, *2*, 7523–7533.
21. Hwang, S. H.; Moorefield, C. N.; Wang, P.; Jeong, K.; Cheng, S. Z. D.; Kotta, K. K.; Newkome, G. R. Dendron-tethered and templated CdS quantum dots on single-walled carbon nanotubes. *J. Am. Chem. Soc.* **2006**, *128*, 7505–7509.
22. Choi, S. K.; Chun, K. Y.; Lee, S. B. Selective decoration of silver nanoparticles on the defect sites of single-walled carbon nanotubes. *Diamond Relat. Mater.* **2009**, *18*, 637–641.
23. Lu, C.; Akey, A.; Wang, W.; Herman, I. P. Versatile formation of CdSe nanoparticle-single walled carbon nanotube hybrid structures. *J. Am. Chem. Soc.* **2009**, *131*, 3446–3447.
24. Qu, L.; Dai, L. Substrate-enhanced electroless deposition of metal nanoparticles on carbon nanotubes. *J. Am. Chem. Soc.* **2005**, *127*, 10806–10807.
25. Qu, L.; Dai, L.; Osawa, E. Shape/size-controlled syntheses of metal nanoparticles for site-selective modification of carbon nanotubes. *J. Am. Chem. Soc.* **2006**, *128*, 5523–5532.
26. Quinn, B. M.; Dekker, C.; Lemay, S. G. Electrodeposition of noble metal nanoparticles on carbon nanotubes. *J. Am. Chem. Soc.* **2005**, *127*, 6146–6147.
27. Sahoo, S.; Husale, S.; Karna, S.; Nayak, S. K.; Ajayan, P. M. Controlled asssembly of Ag nanoparticles and carbon nanotube hybrid structure for biosensing. *J. Am. Chem. Soc.* **2011**, *133*, 4005–4009.

28. Yu, C.; Ryu, Y.; Yin, L.; Yang, H. Modulating electronic transport properties of carbon nanotubes to improve the thermoelectric power factor via nanoparticle decoration. *ACS Nano* **2011**, *2*, 1297–1303.
29. Gao, R.; Zheng, J. Amine-terminated ionic liquid functionalized carbon nanotube-gold nanoparticles for investigating the direct electron transfer of glucose oxidase. *Electrochem. Commun.* **2009**, *11*, 608–611.
30. Ozawa, H.; Yi, X.; Fujigaya, T.; Niidome, Y.; Asano, T.; Nakashima, N. Supramolecular hybrid of gold nanoparticles and semiconducting single-walled carbon nanotubes wrapped by a porphyrin-fluorene copolymer. *J. Am. Chem. Soc.* **2011**, *133*, 14771–14777.
31. Li, X.; Jia, Y.; Cao, A. Tailored single-walled carbon nanotube-CdS nanoparticle hybrids for tunable optoelectronic devices. *ACS Nano* **2010**, *4*, 506–512.
32. Kongkanand, A.; Kuwabata, S.; Girishkumar, G.; Kamat, P. Single-walled carbon nanotubes supported platinum nanoparticles with improved electrocatalytic activity for oxygen reduction reaction. *Langmuir* **2006**, *22*, 2392–2396.
33. Wang, D.; Li, Z. C.; Chen, L. Templated synthesis of single-walled carbon nanotube and metal nanoparticle assemblies in solution. *J. Am. Chem. Soc.* **2006**, *128*, 15078–15079.
34. He, D.; Zeng, C.; Xu, C.; Cheng, N.; Li, H.; Mu, S.; Pan, M. Polyaniline-functionalized carbon nanotube support platinum catalysts. *Langmuir* **2011**, *27*, 5582–5588.
35. Ren, L.; Yang, L.; Yu, P.; Wang, Y.; Mao, L. Electrochemical post-treatment of infinite coordination polymers: an effective route to preparation of Pd nanoparticles supported onto carbon nanotubes with enhanced electrocatalytic activity toward ethanol oxidation. *ACS Appl. Mater. Interfaces* **2013**, *5*, 11471–11478.
36. Zhang, S.; Ji, C.; Bian, Z.; Yu, P.; Zhang, L.; Liu, D.; Shi, E.; Shang, Y.; Peng, H.; Cheng, Q.; Wang, D.; Huang, C.; Cao, A. Porous, platinum nanoparticle-adsorbed carbon nanotube yarns for efficient fiber solar cells. *ACS Nano* **2012**, *6*, 7191–7198.
37. Meng, L.; Xia, W.; Liu, L.; Niu, L.; Lu, Q. Golden single-walled carbon nanotubes prepared using double layer polysaccharides bridge for photothermal therapy. *ACS Appl. Mater. Interfaces* **2014**, *6*, 4989–4996.
38. Ritz, B.; Heller, H.; Myalitsin, A.; Kornowski, A.; Martin-Martinez, F. J.; Melchor, S.; Dobado, J. A.; Juarez, B. H.; Weller, H.; Klinke, C. Reversible attachment of platinum alloy nanoparticles to nonfunctionalized carbon nanotubes. *ACS Nano* **2010**, *4*, 2438–2444.
39. Garcia-Aguilar, J.; Miguel-Garcia, I.; Berenguer-Murcia, A.; Cazorla-Amoros, D. Single wall carbon nanotubes loaded with Pd and NiPd nanoparticles for H_2 sensing at room temperature. *Carbon* **2014**, *66*, 599–611.
40. Corma, A.; Garcia, H.; Leyva, A. Catalytic activity of palladium supported on single wall carbon nanotubes compared to palladium supported on activated carbon: Study of the Heck and Suzuki couplings, aerobic alcohol oxidation and selective hydrogenation. *J. Mol. Catal. A: Chem.* **2005**, *230*, 97–105.

41. Hu, L.; Zhao, Y. L.; Ryu, Y.; Zhou, C.; Stoddart, J. F.; Gruner, G. Light-induced charge transfer in pyrene/CdSe-SWNT hybrids. *Adv. Mater.* **2008**, *20*, 939–946.
42. Penicaud, A.; Poulin, P.; Derre, A.; Anglaret, E.; Petit, P. Spontaneous dissolution of single-walled carbon nanotube salt. *J. Am. Chem. Soc.* **2005**, *127*, 8–9.
43. Jiang, C.; Kempa, K.; Zhao, J.; Schlecht, U.; Kolb, U.; Basche, T.; Burghard, M.; Mews, A. Strong enhancement of the Breit-Wigner-Fano Raman line in carbon nanotube bundles caused by plasmon band formation. *Phys. Rev. B: Condens. Matter Mater. Phys.* **2002**, *66*, 161404(R).

Chapter 5

Multifunctional Nanoparticles in Radiation Oncology: An Emerging Paradigm

Jodi E. Belz,[1] Wilfred Ngwa,[2] Houari Korideck,[2] Robert A. Cormack,[2] Ross Berbeco,[2] Mike Makrigiorgos,[2] Srinivas Sridhar,[1,2] and Rajiv Kumar[*,1,2]

[1]Nanomedicine Science and Technology Center and Department of Physics, Northeastern University, Boston, Massachusetts 02115, United States
[2]Department of Radiation Oncology, Dana-Farber Cancer Institute, Brigham and Women's Hospital and Harvard Medical School, Boston, Massachusetts 02215, United States
[*]E-mail: r.kumar@neu.edu, rajiv_kumar@dfci.harvard.edu

The parallel advances in the field of radiation oncology and nanotechnology have created a paradigm changing opportunity to improve the therapeutic outcome in oncology. The integration of nanomedicine in clinical oncology has led to the appreciation of the use of 'theranostic nanoparticles' in not only understanding various biological mechanisms associated with cancer, but also in successfully targeting these pathways to modulate the efficacy of treatment. This chapter focuses on the application of various nanoparticle-based formulations to improve radiation therapy. The emphasis is on the functionality of nanoparticles that can modulate the tumor response to radiation, target the molecular pathways, minimize normal tissue toxicities and improve the imaging efficacy for better disease staging and treatment planning. We believe addressing these factors using nanoparticles can shape the future of radiation therapy, facilitating their use towards a personalized medicine approach.

In The Science and Function of Nanomaterials: From Synthesis to Application; Harper-Leatherman, et al.;

Introduction

The field of radiation oncology has evolved tremendously since X-rays were first discovered by Roentgen in 1895. The notion of using radioactive materials to treat cancer accounts back to 1901 (*1*, *2*). Since then radiotherapy (RT) has become a standard treatment option for more than 50% of malignancies (*3*, *4*). RT involves the use of high energy ionizing X-rays or gamma rays to ionize the cellular components (mainly DNA) or to generate charged species (free radicals) within the diseased cells to damage DNA (*5*, *6*). Usually, DNA is the prime target of the ionizing radiation, however, the resulting free radicals are also known to interact with membrane structures inducing lipid peroxidation and further apoptosis. Revolutionary progress in the development of X-ray production and delivery techniques, improved imaging efficacy, and better treatment planning systems have led to improved therapeutic benefit in RT. The advanced RT modalities which include intensity-modulated RT (IMRT), image guided RT (IGRT), stereotactic body RT (SABR), proton therapy (PT) and external beam RT (XRT) provide enhanced therapeutic efficacy with greatly reduced side effects (refer to appendix 1 for a complete list of abbreviation definitions used throughout the chapter) (*7*). The improved accuracy of radiation treatment combined with the plethora of knowledge on cancer biology has in turn made dose escalation or "radiation boosting" feasible and has helped to further improve the therapeutic ratios for several tumor sites in the body.

Although the advances in RT have led to higher survival rates for some early stage cancers, many cancer survival rates are still very depressing. A majority of patients treated with RT suffer from local recurrence, metastasis and a high degree of normal tissue toxicities (*8–10*). In the case of prostate cancer, data from two randomized trials suggests that increased radiation dose is associated with improved cancer control, but radiation dose-escalation is generally limited by the toxicity from the anterior rectal wall and urethra receiving dose levels beyond tolerance (*11*, *12*). Following initial radiation in prostate cancer, between 20-30% of men may experience Prostate Specific Antigen (PSA) failure (*11*). For those with a local-only recurrence, salvage brachytherapy offers a second chance for a cure, but leads to a high rate of rectal toxicity including up to a 13% rate of prostate-rectum fistulas requiring colostomy in one prospective phase II study (*10*, *13*). Although boosting radiation dosage is an alternative, this is limited by normal tissue toxicity and other factors including tumor or patient movement (*14–18*). Clearly there is a need to improve current treatment strategies to enhance the efficacy of radiation with lower doses in the tumor tissue but with minimal toxicity to adjacent normal tissues (*19*).

In this chapter, we focus on how novel nanoparticle-based formulations have shown tremendous potential in addressing the challenges associated with RT. A variety of examples of nanoparticles with single, as well as multiple functionalities within the oncology field are included. The topics covered by this chapter include the role of different types of nanoparticle-based formulations in radiosensitizing tumor tissues, targeting molecular pathways by means of nanoparticles, reducing non-specific radiation toxicity and enhancing imaging efficacy for better disease staging.

Role of Nanoparticles in Radiation Therapy

The advent of nanoparticles has revolutionized research in the field of medicine in diagnostics and therapy (*20*, *21*). Owing to the unique properties associated with nanoparticles, there are several advantages for the application of nanoparticles in the field of medicine which include (a) multimodal imaging (optical, PET, MR) capability in a single nanoplatform allowing for cross validation and quantification across different imaging platforms (*22*, *23*). (b) superior targeting to the specific diseased sites using various biomolecules (peptides, antibodies, aptamers etc.) (*24*). (c) 'theranostic' properties which provide imaging and therapeutic ability using the same platform (*25*). (d) ease of modulation of surface properties which allows for surface functionalization with various imaging and targeting agents (*26*). and (e) size tunability which governs pharmacokinetics and biodistribution in systemic circulation in vivo (*27*, *28*).

A better understanding of the interaction of nanoparticles in biological systems has laid a foundation for designing smart nanoparticles which can address the issues associated with RT. Designing such nanoparticle-based platforms that are capable of longer retention in systemic circulation and of delivering the therapeutics to targeted sites requires an understanding of the physico-chemical interactions between the nanoparticles and the biological systems. The new generations of nanoparticles are engineered with considerations to the disease type, microenvironment of the disease site, mode of interaction with non-target organs and the fate of these nanoparticles in an *in vivo* environment (*29*, *30*). Several nanoparticle-based formulations have been developed over the years which have shown potential in either enhancing the effective radiation dose or reducing the normal tissue toxicities. There are several different mechanisms by which nanoparticles have shown promise in improving the RT in different cancer models. The role of nanoparticles, in conjunction with improving the efficacy of RT, can be categorized into four major subcategories:

1. Increasing Tumor Response by Radiosensitizing Nanoparticles

As the name suggests, radiosensitization is the use of agents, either drugs or nanoparticles, to increase the sensitivity of the tumor cells to radiation (*31*, *32*). Radiosensitization using nanoparticles is dependent on the type and design of nanoparticle. These properties determine the mechanism by which nanoparticles will radiosensitize the tumor tissue. Nanoparticles can themselves act as radiosensitizers (high atomic number nanoparticles) or they can act as a delivery vehicle for various known radiosensitizers (metronidazole, tirapazamine, gemcitabine, docetaxel etc.) (*30*, *33–35*). In both cases, the efficacy of radiosensitization is determined by the targeting efficiency of the nanoparticles to the tumor site. The nanoparticles can be targeted by passive targeting via the enhanced permeability and retentivity, or EPR effect, or by active targeting using specific biomarkers which are over-expressed on tumor cells (*36–39*). Efficient targeting of radiosensitizing nanoparticles leads to a higher uptake of nanoparticles at the tumor site and thus an increased sensitivity of only cancer cells to radiation while sparing the normal cells from radiotoxicity.

In The Science and Function of Nanomaterials: From Synthesis to Application; Harper-Leatherman, et al.;

Nanoparticle-based platforms that radiosensitize cancer cells by different mechanisms are outlined below.

1a. High Atomic Number Nanoparticles

Increases in radiation sensitivity, specifically in tumor cells, has been studied over the last 25 years using various high atomic number (Z) materials. The first report of radiation dose enhancement using high Z-materials dates back to 1980, in which iodine (I) was used for sensitizing mammalian cells by means of the photoelectric effect (*40*). Since then, high Z-materials like gold, platinum, gadolinium, silver, and iron in different forms have been tested for enhancing the efficacy of radiation therapy.

Mechanism of Interaction

These high Z-materials are known to interact with high energy X-rays or gamma rays by different mechanisms which primarily include selective absorption/scattering and photoelectric scattering (*41*). Thus the interaction between the materials and the radiation is highly dependent on the X-ray energy, the atomic number and the density of the material. The interaction of X-rays with these high Z-materials involves three major processes: the photoelectric effect, Compton scattering and pair production. The different interactions which occur when X-rays of different energies interact with a high Z-material are shown in Figure 1.

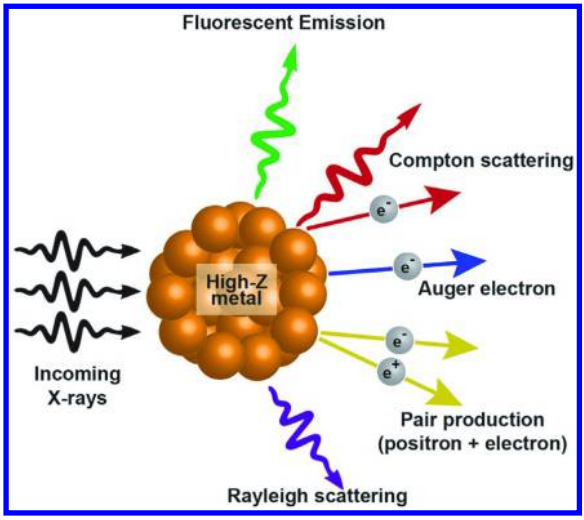

Figure 1. Interaction of X-rays with high-Z material nanoparticles. (Reproduced with permission from reference (41). Copyright (2014) Pioneer Bioscience Publishing Company.)

The primary photoelectric absorption process leads to ejection of an inner-shell orbital electron, destabilizing the atom. Stability is restored by the transfer of a higher energy outer-shell electron to the inner shell and the release of extra energy as characteristic X-rays (or fluorescent photons). This released energy is further absorbed locally by an outer-orbital electron and is emitted as Åuger electrons from the atoms (secondary photoelectric effect) (*42–45*).

Since this photoelectric effect is dependent on the energy of the photon and atomic number of the absorbing material, the relationship between the two can be approximated to be proportional to $(Z/E)^3$ where E is the energy of the incident photon and Z is the atomic number of the absorbing material (*46*). Higher energy incident photons lead to Compton interactions (involving only free electrons present in outmost shell) and pair production interactions (involving interaction of photon with electromagnetic field of atomic nucleus).

X-ray generators provide power to the X-ray tube and allow operators to control three key parameters: X-ray tube voltage (kV), tube current (mA), and exposure time. Tube voltage affects the X-ray energy. X-rays are produced when electrons with energies of 20-150 kiloelectron volts (KeV) are stopped in matter, causing the energetic electrons to convert their energy directly into a photon. Electrons accelerated to the positive anode gain a kinetic energy of voltage considered electron voltage (eV). The amount of kinetic energy gained is determined solely by the value of the applied peak voltage (Vp). As the energy of the X-ray tube increases, the maximum number of X-ray photons increases, and therefore X-ray photon energy (KeV) increases. These values determine the available exposure of the X-ray beam and its intensity, strength, or amount of radiation present. The radiation energy absorbed is related to the available exposure, and the material or tissue in the radiation field. Absorbed dose is measured in grays (Gy) (see appendix 2 for unit definitions) and measures the amount of radiation energy absorbed per unit mass of medium. Absorbed dose is commonly used to represent the dosing of radiotherapy. The energy of ionizing radiation is measured in electronvolts (eV) which can be classified as either ‘diagnostic’ X-rays in kilovoltage (kV) range for imaging and treating superficial sites like skin cancer or ‘therapeutic’ X-rays in Megavoltage (MV) range (4-25 MV) for treating deep seated tumors. The interaction of high Z-materials like gold nanoparticles with radiation dominates at energies less than 0.5 MeV. With tissue material the interacting energy is less than 0.03 MeV.

The combinations of photoelectrons, Auger electrons, scattered X-rays, Compton electrons, fluorescence photons and positrons results in a localized ionization and delivery of a precise lethal dose of radiation in their immediate vicinity. This is particularly attractive when these processes can be achieved by means of using high Z-nanomaterials. The inherent unique properties of nanoparticles can effectively add to the radiosensitization of the diseased site. The excellent targeting ability of the nanoparticles to the tumor cells allows for intracellular generation of these ionizing electrons and reactive species upon interaction with X-rays (*47*). Since the nanoparticles preferentially target the tumor cells, normal tissue is spared from the unwanted radiation toxicity. In the presence of targeted nanoparticles, the effective localized dose due to radiosensitization will be much higher than the calculated dose for the tumor cells

In The Science and Function of Nanomaterials: From Synthesis to Application; Harper-Leatherman, et al.;

without the nanoparticles (*48*, *49*). The production of secondary electrons and free radicals (generated as a result of the ionization of water molecules) inside tumor cells results in breaking the chemical bonds of proteins, DNA and other biomolecules leading to apoptosis and ultimately cell death (*50*). Usually these secondary electrons are responsible for DNA single strand breaks or more lethal double strand breaks (*8*). Thus, the radiation dose enhancement present in tumor cells from targeted high Z-nanoparticles, like gold, can result in better efficacy in controlling the tumor progression and thereby improving the therapeutic outcome tremendously.

a. Gold Nanoparticle (GNP) Formulations in Radiation Therapy

There are several nanoparticle based formulations which are studied for enhancing the radiation dose locally either in vitro or in vivo. However, gold nanoparticles (Z=79) stand out among all other nanoparticle formulations because of their inherent unique properties. Several advantages associated with gold nanoparticles that make them ideal candidates for use in radiation therapy include: (a) high biocompatibility and inertness (*51*). (b) ability to absorb more radiation than any other high Z-material between 20 to 100KeV, three times more radiation as compared to iodine (*52*). (c) the ease of fabrication and size tunability (dose enhancement factor (DEF) depends on the size of the nanoparticles) (*53*, *54*). (d) the surface of the gold nanoparticles can be easily passivated with different ligands which, not only determine the systemic circulation time, but also can be utilized for conjugating different imaging and targeting agents (*55*, *56*). (e) highly efficient targeting to the tumor sites can be achieved using GNPs with conjugated biomolecules (*57*). and (f) the added advantage of conjugating imaging modality to the nanoparticle surface can lead to a system which can measure the effectiveness of treatment in real time concomitantly using non-invasive imaging techniques (*30*, *58*, *59*).

In Vitro Radiosensitization

Gold was first used as a radiosensitizer back in 1998 when Regulla et al. showed radiation dose enhancement in cells using gold sheets (*60*). Further, Herold et al. used gold microspheres for dose enhancement and radiosensitization using CHOK1, EMT-6 and DU145 cell lines with kilovoltage X-ray photons. A DEF of 1.42 with 1% gold particle concentration was achieved (*61*). Studies by Zheng et al. have shown that the enhancement of radiation is primarily due to low energy electrons produced by gold nanoparticles with the enhancement effect being directly proportional to the number of GNPs in the vicinity of DNA (*62*). Brun et al. studied the effect of size and concentration of GNPs to enhance radiation dose (*63*). Their results showed a 6-fold enhancement with the large size (92nm) particles at higher concentration using 50 KeV photons. Several other reports also showed enhancement using GNPs in conjunction with radiation (*64–69*). Our group has also explored the use of GNPs as radiosensitizers in low

dose rate gamma radiation therapy using I-125 brachytherapy seeds (*48*). We have found as high as 130% increase in therapeutic efficacy with 50 nm GNPs. In vitro radiosensitization of the cervical cancer cell line HeLa using 50 nm, as well as third generation GNPs (2 nm core size) showed higher damage with a combination of GNPs and radiation at KeV and MeV (*30*, *70–73*). The different results quoted above stem from differing key parameters during investigations including nanoparticle shape, size and concentration, type of cell line, and radiation energy and type. An attempt has been made by a few researchers to comprehensively evaluate the affecting parameters including DNA:GNP molar ratio, GNP diameter and incident X-ray energy. However, the results are limited in scope (*53*, *74*).

In Vivo Radiosensitization

Several in vivo therapeutic studies were also reported using GNPs as radiosensitizers. The pioneering work of Hainfield et al. triggered the use of GNPs in combination with radiation (*35*, *75*, *76*). The study involved the use of mice with subcutaneous EMT-6 mammary carcinoma injected intravenously with 1.9 nm GNPs. The results showed a long term survival for 86% of the mice treated with GNPs and radiation, as opposed to only 20% survival for the mice treated with radiation alone at the same dose. Chang et al. followed the previous work using clinically relevant MV radiation energies in B16F10 melanoma mice models treated with 13 nm GNPs (*77*). Those results showed a prolonged survival for mice treated with GNP and a megavoltage radiation beam. It is worth noting here that this study involved the use of bigger-sized nanoparticles at lower concentrations with a time interval of 24 hours between the GNPs administration and irradiation. The previous study used very high concentrations of GNPs (2.7g/kg of body weight) with an interval of only 15 min between injection of nanoparticles and irradiation.

It is quite evident from these studies that the pharmacokinetics of nanoparticles plays a critical role in determining the efficacy of radiosensitization/ treatment. The smaller particles (1.9 nm) tend to clear faster, within 15 min via renal excretion, thus a very high concentration is required for intravenous injections. The larger-sized nanoparticles (13 nm) undergo hepatobiliary excretion and require further surface modifications to improve the pharmacokinetics by using amphiphilic molecules, like polyethylene glycol (PEG), which suppress the non-specific opsonization process and enhance circulation time of the nanoparticles (*27*, *28*). Thus, following a similar strategy several in vitro and in vivo studies were focused on PEGylated GNPs as radiosensitizers using different radiation sources 6.5KeV, 6MV, 15MV, 3MeV (*49*, *67*, *74*, *78*, *79*). Chithrani et al. have studied the size dependent radiosensitization using GNPs and reported that 50 nm GNPs showed highest dose enhancement based on a higher degree of internalization of these nanoparticles in comparison to smaller sizes (*53*, *54*).

b. Multifunctional GNPs in Radiosensitization

A multifunctional GNP-based formulation where GNPs were functionalized with different gadolinium chelates for use in imaging, as well as radiosensitization, was reported using 83KeV radiation source (*80*). The studies showed that 2.4 nm dithiolated-diethylene triamine pentaacetic acid-GNPs (DTDTPA-GNPs) injected in rats bearing 9L gliosarcoma were able to penetrate the blood brain barrier with a larger survival rate (33 days) than the non-treated animals (17 days). Although the formulation was found to be slightly toxic, this was the first example where multifunctionality of nanoparticles was exploited for simultaneous imaging and radiation therapy. Furthermore, Hainfield et al. have combined different treatment modalities by using hyperthermia and RT using 1.9 nm GNPs as radiosensitizers in radiation resistant murine squamous carcinoma (SCCVII) mouse models (*76*). Recently, another study by Zaki et al. reported the use of 1.9 nm GNPs encapsulated in PEG-PCL polymeric micelles (*81*). In this study, the multifunctionality of GNPs in CT imaging and therapy by radiosensitization was utilized in HT-1080 human fibrosarcoma mouse models. CT (Computed Tomography) is a technology that uses computer-processed X-rays to produce tomographic images (virtual 'slices') of specific areas of the scanned object, allowing the user to see inside without cutting. The results showed improved delineation of tumor margins 24 hours post intravenous administration of polymeric micelles and also resulted in a 1.7-fold improvement in median survival time. Masood et al. have used gold nanorods complexed with SiRNA to efficiently deliver siRNA for radiosensitization in head and neck cancer (*82*). The studies showed that the GNR-siRNA nanoplexes injected intratumorally into subcutaneous HNSCC tumors in mice, prior to radiation therapy, resulted in over 50% tumor regression compared to control (GNR-siRNA nanoplex and radiation treated) groups even at radiation doses much lower than those commonly required in clinical RT.

Although every study performed with different GNP-based formulations with radiation therapy have shown promising results, these studies still have several drawbacks. The evaluation of the type of nanoparticles used previously for the radiation treatment can, not only help in addressing these limitations, but can also lead to careful assessment of nanoparticle designs based on the interaction of these nanoparticles with biological systems. These evaluations led to the fabrication of a new generation of nanoparticles which are constructed after considering the disease type, microenvironment of the diseased site, fate of nanoparticles and non-specific toxicity to the normal tissues (*29*). Currently, third generation nanoparticles are being engineered based on the evaluations of the previous formulations. Researchers are considering the limitations associated with the first two generations of nanoparticles which were more focused only on surface modification (first generation) stealth behavior, and targeting (second generation). Our group has recently reported a third generation gold nanoparticle platform (AuRad™) for applications in RT (*30*). Preliminary in vitro results showed that nanoparticles can efficiently be used for imaging cervical cancer HeLa cells using fluorescence imaging eliciting 2.8 fold cell kill enhancement when treated with radiation at 220 KVp. In vivo imaging studies showed highly

efficient targeting of orthotopic pancreatic tumors in mice. Further therapeutic studies with KVp and MV radiation sources are underway.

c. Other High Z-Nanoparticles in Radiosensitization

Although GNPs have been most widely used for dose enhancements in RT, particles with several other high Z-materials have shown potential as radiosensitizers as well. The Tillement research group has extensively worked on ~1.1 nm diameter Gadolinium (Gd) based-nanoparticles where a gadolinium oxide core passivated by a polysiloxane shell further conjugated with chelating agent DTPA was designed for imaging and RT (*83*, *84*). The net surface charge of the nanoparticles was close to 3 mV. These nanoparticles have shown efficient dose enhancement in 9L gliosarcoma-bearing rats with a median survival time of 90 days when nanoparticles were injected intravenously and treated with radiation. Comparatively, the animals treated with radiation alone showed a survival time of only 47 days. Other nanoparticle based-formulations which have been explored in enhancing RT include silver, titanium oxide, hafnium oxide, iron oxide, and fullerenes (*85–88*). The properties of GNPs show superiority as nanoparticles for use in RT and are thus by far the most widely studied nanoparticle formulation for improving the therapeutic outcome in RT.

1b. Radiosensitizer Delivery via Nanoparticles

The use of nanoparticles as delivery vehicles has triggered the development of new nanoparticle-based formulations using a variety of drugs. Some of these formulations include the encapsulation of conventional radiosensitizing drugs which include paclitaxel, docetaxel (DTX), and gemcitabine using polymeric nanoparticles (*89–91*). The poor solubility of most of the chemotherapeutic/radiosensitizing drugs and their broad distribution in both tumor and normal tissues, which causes treatment related toxicities, requires a suitable delivery vehicle and therefore polymeric nanoparticles have been studied extensively in delivering a variety of chemotherapeutic drugs. The advantages associated with nanoparticle-based drug delivery systems include (a) efficient encapsulation of these poorly soluble drugs in biocompatible and biodegradable matrices, (b) efficient accumulation in a tumor either by the EPR effect or active targeting, sparing the normal tissues and decreasing associated toxicity, (c) long circulation time improving the pharmacokinetics of the encapsulated drug, and (d) slow and sustained release of the encapsulated drug from the nanoparticles.

Several reports in the literature showed that these nanoparticles were used as carriers for various radiosensitizing molecules. Poly(lactic-co-glycolic acid) (PLGA) nanoparticles encapsulated with DTX were evaluated for radiosensitizing properties. The results indicated that these PLGA-DTX nanoparticles injected in murine KB xenografts irradiated with a 12 Gy dose of radiation were more efficient in retarding tumor growth rate as compared to non-targeted or DTX-free formulations (*92*). Another study exploiting the properties of nanoparticles used

PLGA nanoparticles encapsulating DTX, Indium-111 and Yttrium-90 (Y-90) to formulate a ChemoRad platform (*93*). The results showed a higher degree of cell kill with the targeted delivery of ChemoRad nanoparticles in prostate cancer cells when both DTX and Y-90 were encapsulated together in nanoparticles.

Paclitaxel, which is a known chemotherapeutic and radiosensitizing drug, was also delivered using nanoparticles in combination with a hypoxic radiosensitizer, Etanidazole using PLGA nanoparticles (*94*). The results, not only showed efficient susceptibility of the cancer cells to radiation, but also radiosensitization of the hypoxic cells. Another formulation of paclitaxel, Genexol-PM, also showed efficient radiosensitization of non-small cell lung cancer with reduced toxicity to normal lung tissues (*95*).

The encapsulation of abandoned molecules like Wortmannin in lipid-polymer nanoparticle platforms showed the potential of nanoparticulate delivery which overcomes the challenges associated with drug delivery without a polymer carrier (*96*). The results indicated an efficient radiosensitization even at low concentrations of Wortmannin encapsulated in nanoparticles in murine xenograft animal models.

1c. INCeRT (Implantable Nanoplatforms for Chemo-Radiation Therapy) Implants for IGRT (Image Guided Radiation Therapy)

The radiosensitization of diseased sites by means of nanoparticles is not restricted to the use of nanoparticles as carriers or as radiosensitizers in themselves. The nanoparticles can also be used in the form of smart implants which can act as depots with sustained release of radiosensitizing nanoparticles. These implants are particularly attractive in radiotherapy treatment modalities like brachytherapy (BRT) and external beam radiation therapy (XRT). In both modes of RT, inert objects may be placed in the prostate for the technical purpose of controlling the spatial distribution and accuracy of radiation to the prostate. Inert radio-opaque fiducials are frequently implanted to guide the delivery of XRT treatments, while inert and biocompatible spacers are used in BRT to maintain the desired source configuration (*97–100*). These implanted spacers and fiducials are critical technical components for radiation delivery but have ‘zero’ direct therapeutic benefits at present (*99*).

It has been proposed that the XRT fiducials and BRT spacers offer the opportunity for in-situ delivery of drugs as part of currently routine minimally invasive radiation therapy procedures. Modeling of the drug distributions that could be achieved by transforming the inert fiducials or spacers into drug reservoirs, which are capable of sustained drug release over periods appropriate to radiation therapy, indicates that significant portions of the prostate could be radiosensitized while maintaining a localized drug distribution. Thus, here exists an excellent opportunity to fabricate these inert spacers in such a way that it improves the therapeutic ratio of the brachytherapy procedure by delivering a radiosensitizer to the prostate without systemic toxicity. Figure 2 describes the schematic presentation of the INCeRT platform. Our group has previously

conducted a theoretical evaluation of prostate brachytherapy spacers containing slow-release polymers that elute the radio-sensitizer DTX (*100*).

The coating of radio-opaque gold fiducials in XRT with radiosensitizing nanoparticles could facilitate a localized delivery of radiosensitizing nanoparticles to tissues. Localized delivery combined with slow sustained release of radiosensitizing nanoparticles from coated fiducials can enhance the therapeutic efficacy of IGRT by providing a biological in situ dose painting of tumor tissue with nanoparticles.

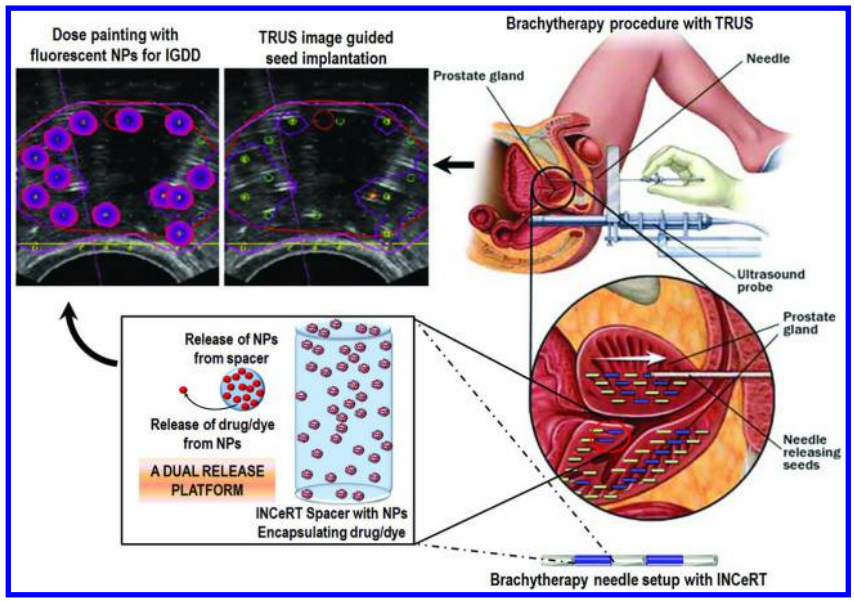

Figure 2. Schematics of INCeRT spacers for combined chemo-radiation therapeutic application in prostate cancer. (Reproduced with permission from reference (102). Copyright (2014) Publisher Mayo Foundation for Medical Education and Research.)

Our group has previously reported the temporal release kinetics of the PLGA nanoparticles encapsulating coumarin-6 from a chitosan matrix coated on fiducials (*101*). The results showed that the dosage and rate of release of these nanoparticles coated on fiducials can be tailored to maximize the therapeutic benefit. These results support the concept of highly localized delivery via nanoparticles. Furthermore, we have extended the BIS-IGRT platform to BRT spacers by using polymer PLGA as the matrix and adding fluorescent silica nanoparticles encapsulating DTX (*102*). The silica nanoparticles embedded in the PLGA matrix were formulated to maintain the physico-chemical properties of the clinical BRT spacers. These INCeRT implants possess functional properties allowing further imaging in real time using optical fluorescence and provide an additional chemo-radiation therapeutic intervention (*102*). The results obtained from INCeRT spacers implanted subcutaneously in mice showed that the release profile of the nanoparticles can be modulated by varying the size of nanoparticles

incorporated in the polymer matrix (smaller size resulted in faster diffusion). Another modified version of the BRT spacers, where GNPs were incorporated in the PLGA matrix, has been fabricated by our group. The preliminary in vivo therapeutic efficacy and toxicology studies with the INCeRT spacers doped with DTX showed a tremendous potential of these spacers in treating prostate cancer at lower radiation doses. These spacers are fabricated specifically for intended use in clinical settings and thus successful preclinical studies can be easily translated to clinics in the near future.

Further in vivo therapeutic efficacy studies are currently underway with these implantable platforms in combination with RT. Wang et al. have also reported the modification of inert BRT spacers by doping them with micro/nanoparticles encapsulating various antibiotics and radiosensitizing drugs (*103*).

Several advantages associated with nanoparticle-based smart implants for application in radiation therapy include:

a. Ease of fabrication with biodegradable polymers and morphological similarity to the clinically used spacers.
b. Wide variety of radiosensitizing nanoparticles can be used.
c. Application to various radiation treatment modalities including BRT, SABR, IMRT, IGRT, PT, heavy ion therapy, and fast neutron therapy.
d. Efficient localized drug delivery (nearly 100%) at the target site reducing non-specific accumulation of the drug in other organs and thus minimal toxicities to other organs.
e. Complete delivery of the drug to the tumor results in negligible systemic toxicity compared with systemic administration of the drug.
f. A dual release platform: the rate of the drug release governed by the rate of release of the nanoparticles from the spacer's polymer matrix and the release of the drug from the nanoparticles. This dual release platform provides an efficient slow sustained release of the drug at the target site over longer time durations.
g. Spatial distribution of the drug over a larger portion of the tumor tissue. The movement of nanoparticles released from the spacers into the tumor interstitial spaces determines the uniform distribution of the drug over the entire tumor tissue.
h. Nanoparticle-based spacers do not require any additional clinical intervention to implant in the desired region of the prostate as these modified spacers will just replace the spacers currently used in surgical procedures.

2. Targeting Molecular Pathways (Radiation Resistance)

Despite advances in the area of treatment planning, clinical techniques and emergence of new treatment modalities, there are a number of patients who still suffer local recurrence after radiation therapy. Some of these factors leading to recurrence of cancer can be minimized and explained by advanced tumor stage, inaccurate radiation delivery to tumor and tumor heterogeneity (*8*). However, many questions can only be answered based on the understanding of the tumor

biology. Three main biological factors were shown to be very critical in improving the outcome of radiation therapy: the extent of hypoxia, ability of surviving cells to repopulate within the treatment time frame, and the development of resistance of tumor cells (*104–107*). Modulation and targeting these factors by means of using inhibitors can efficiently improve outcome of treatment (*108*). The use of nanoparticles can efficiently target the tumor site not only to modulate the microenvironment resulting in sensitization of hypoxic areas of tumor, but also nanoparticles can be used to deliver inhibitors which target specific biological processes like DNA repair. The schematics of various pathways and DNA damage responses in response to ionizing radiations are shown in Figure 3.

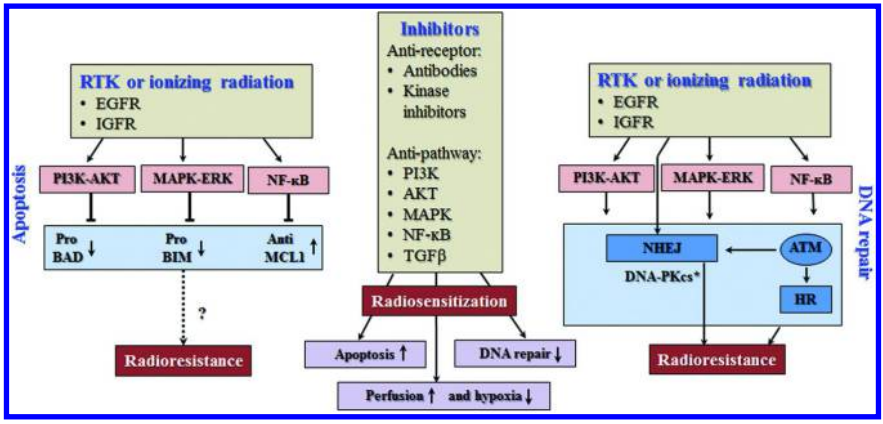

Figure 3. Targeting signaling pathways using nanoparticles to enhance the radiosensitization. (Reproduced with permission from reference (8). Copyright (2014) Nature Publishing Group.)

Advancement in the field of radiation biology has led to better understanding of tumor response to ionizing radiations. Radiation is primarily known to inflict DNA damage to tumor cells via different mechanisms which include single-strand breaks (SSBs), double strand breaks (DSBs), oxidized based damage, and abasic site formation (*109*). The failure to repair these lesions in the genetic material results in tumor regression. However, the DNA lesions caused by radiation triggers DNA damage responses (DDR) which ultimately activate intracellular signaling pathways (*110*, *111*). Several cell cycle check points assess the repair and propagation of damaged DNA to next progeny. The defective DDR and DNA repair genes leads to mutations like BRCA1, BRCA2, ATM, TP53, CDKN2A (*112*, *113*). These mutations and defects govern the tumor response to RT, thus targeting these repair pathways and checkpoint responses can drastically change the future of radiation therapy.

2a. Targeting DNA Damage Repair Responses (DDR)

There are several checkpoints which can be targeted to improve the response of tumor cells to RT sparing the normal cells. These include targeting the

proliferative nature of the tumor, inhibition of replication processes or inhibition of repair processes. Poly(ADP-ribose) polymerase (PARP) regulates the base excision repair (BER) and SSBs repair induced by radiation. Thus inhibition of PARP1 leads to formation of DSBs and thus increases the lethality leading to cell death. Various PARP inhibitors are currently being evaluated in different clinical trials with radiotherapy (*114*, *115*). However, the delivery of these inhibitors still poses a major challenge and thus this is where the potential of nanoparticles in delivering and targeting these pathways can be utilized.

There are very limited numbers of studies currently available in which nanoparticles were used as delivery vehicles for these inhibitors along with RT. One such example is reported by our group in which a lipid nanoparticle-based formulation of Olaparib, a potent PARP inhibitor, was used to improve RT (*116*). In vitro results have shown more than 90% cell death with a combination of nano-olaparib and radiation as opposed to only 20% when cells were treated with a similar concentration of free olaparib with the same radiation dose of 4 Gy in prostate cancer PC3, LNCaP and VCaP cell lines. Further studies with a combinatorial formulation in which olaparib and cisplatin were incorporated inside the nanoparticles showed greater cell death when compared with the free drugs (olaparib and cisplatin) in the presence of radiation.

Another study by Ullal et al. reports the conjugation of different PARP inhibitors (olaparib, veliparib, and iniparib) to iron oxide nanoparticles (*117*). Although the study was primarily focused on the drug-target binding mechanisms rather than therapy, it showed that these nanoparticle constructs can be employed to study the pharmacodynamics of these molecularly targeted drugs, ex vivo, through competitive target-drug binding. In addition, Li et al. have shown the liposomal encapsulation of curcumin with oxiplatin to induce a dose dependent growth inhibition in human colorectal cancer LoVo cell lines via apoptosis induced by PARP cleavage (*118*).

2b. Targeting Molecular Pathways

Ionizing radiation is known to activate growth factor receptors (EGFR) which in turn can lead to a cascade of events triggering molecular signaling pathways. These signaling pathways which include PI3K-AKT, MAPK-ERK, nuclear factor NF-κB and transforming growth factor-β (TGF- β) can affect radiosensitivity by decreasing apoptosis and increasing DDR, thus promoting radiation resistance in tumor cells (*119*). Targeting these signaling pathways can lead to resistance reversal using different molecular inhibitors. Until recently, very limited studies were reported that directly address the delivery of inhibitors using nanoparticles along with radiation. New studies using nanoparticle formulations targeting molecular signaling pathways have provided interesting data.

Curcumin is a diarylheptanoid, one of the natural phenols, recently explored for its chemotherapeutic, as well as radiosensitizing properties. The use of nanoparticles not only improved the delivery of curcumin but also showed better therapeutic efficacy. Qiao et al. have shown that curcumin inhibits the constitutive and radiation induced expression of the PI3K-AKT-dependent NF-κB pathway

(*120*). Yallapu et al. have also observed higher sensitivity of cisplatin resistant ovarian cancer cells to both cisplatin and radiation following pretreatment with curcumin, which can be attributed to the down regulation of Bcl-X_L, Mcl-1 and cleavage of caspase 9 and PARP (*121*). To improve the therapeutic efficacy, authors have developed targeted PLGA nanoparticle systems encapsulating curcumin and have shown effective inhibition of A2780CP ovarian cancer cells.

Ping et al. studied a PLGA nanoparticle based formulation encapsulating antisense EGFR on cell survival and radiosensitivity in head and neck squamous carcinoma SCCVII cell line (*122*). The results showed a synergistic inhibition effect when EGFR-PLGA nanoparticles and radiation were given to the cells. The nanoparticles and radiation alone did not show any significant effects on cells. The enhanced radiosensitivity can be attributed to the efficient inhibition of EGFR-mediated pathways by release of EGFR from nanoparticles.

Another molecular target for inhibition which received attention to reverse resistance of cancer cells is Survivin (*123*). Several studies have demonstrated targeting of Survivin using small interfering RNAs, anti-sense oligonucleotides or small molecular repressors which lead to higher sensitivity of tumors towards chemo- and radiation therapy. Gaca et al. have studied the use of a human serum albumin based nanoparticle formulation of Survivin miRNA (*124*). In vitro results with colorectal cancer cells, SW480 showed 50% reduced surviving expression in cells and improved radiosensitization when combined with ionizing radiation. The radiosensitization achieved by Survivin is presumed to be multifaceted through caspase-dependent/independent pathways involving DNA protein kinases.

There are several different nanoparticle formulations which target these signaling pathways, however those formulations are yet to be tested along with radiation therapy (*125–127*). The rapid growth in the number of nanoparticle based formulations for targeting these signaling pathways clearly indicates the potential of nanoparticles in delivering therapeutic molecules, and thus will play a tremendous role in the future for improving sensitization and reversal of resistance of tumor cells towards different therapeutic approaches.

3. Reducing Non-Specific Radiation Toxicity to Normal Tissues

Following radiotherapy, many patients experience side effects such as pain or swelling, mild neutropenia, and telangiectasia, a sunburn-type appearance of the skin. These early side effects occur in rapidly proliferating tissue and usually disappear within a few weeks of treatment. The major concern of radiotherapy is the emergence of late-reacting tissue damage in healthy organs, which can take months to manifest. At the onset of radiation exposure, free radicals are formed though ionizing reactions that are highly reactive with DNA and RNA, causing mutagenesis and cell death. Cellular oxidative damage is initiated by the generation of reactive oxygen species (ROS), which mechanistically change the oxidative state of cells and result in damage to mitochondrial function. While healthy cells have protective and repair mechanisms to combat these effects, they are not capable of blocking all of the damage which ultimately leads to normal tissue death.

Because of these long-term effects, reducing radiation toxicity in patients treated with radiotherapy is mandatory to protect normal tissues from radiation-induced damage. Two major strategies to do so include: 1) the use of radioprotectants to help defend healthy tissue from damage, and 2) the use of radiosensitizing agents at tumor sites to enhance the effects of radiation. Each of these treatment methods has side effects and toxicities of their own. However, the use of nanotechnology can reduce toxicity of the radioprotectants and sensitizing agents, enhance targeting to selected tissue, and possibly reduce the radiation dose required for treatment.

3a. Use of Nanoparticle-Based Radioprotectants

Radioprotectants are substances which protect healthy tissues from radiation-induced damage (*128*). An ideal radioprotectant should selectively protect normal tissues without affecting tumor cells and exert minimum toxicity. The only approved radioprotectant in the clinic to-date is Amifostine (Ethyol, WR-2721), a prodrug, the active free thiol metabolite, WR-1065, of which has been shown to prevent both radiation-induced cell death and mutagenesis while facilitating the repair of normal cells (*129*, *130*). Amifostine, however, has major limitations such as its short half-life, daily dosing requirements, a toxicity based route of administration, and high costs. Patients often have considerable side effects including hypotension (found in 62% of patients), hypocalcaemia, diarrhea, nausea, and vomiting using Amifostine (*129*, *131*). Considerable research effort was made to use nanoparticle-based radioprotectants to combat these effects. More recently, an oral nanoparticle formulation of WR-1065 has been tested in pre-clinical models. WR-1065 was added to PLGA, a biocompatible and a biodegradable polymer for oral delivery; however testing in mice proved particle delivery to be insufficient in a 30 day survival study in comparison to the current standard of systemic treatment (*132*, *133*).

Carbon nanospheres, or fullerenes, and their water soluble derivatives exert anti-oxidative properties and reduce DNA damage in irradiated cells (*132*). The addition of the hydroxyl moiety to the carbons of fullerenes (e.g. $C_{60}(OH)_{24}$, dendrofullerene DF-1, 60-fullerenol) leads to a water soluble molecule with potent free radical scavenger activity (*129*, *132*). A study involving rats reported fullerenol $C_{60}(OH)_{24}$ administered at a high dose 30 minutes before total body irradiation of 7 Gy resulted in radioprotection similar to that provided by amifostine (*134*). The tolerance of the drug and its selectivity remains unknown.

Cerium oxide nanoparticles (CeO_2) are promising radioprotectants (*135*). The unique structure involving the valence and oxygen defects of CeO_2 nanoparticles promotes cell longevity and antioxidant properties that occur with cellular uptake, and prevents the accumulation of ROS thereby preventing activation of apoptotic response and cell death. CeO_2 nanoparticles, synthesized using microemulsion methods, consist of a cerium core surrounded by an oxygen lattice that acts as a scavenger for reactive oxygen and nitrogen species that are generated as a result of ionizing radiation. This scavenging property has been shown to inhibit caspase 3 activation in irradiated colonic crypt tissue, as well as capsase 3 and 7

In The Science and Function of Nanomaterials: From Synthesis to Application; Harper-Leatherman, et al.;

activation in irradiated lung fibroblasts in culture (*136*, *137*). These nanoparticles are also known to increase in vitro super oxide dismutase 2 (SOD2) expression in a dose dependent manner in normal human colon cells. CeO_2 nanoparticles have large surface energy derived from a high surface area to volume ratio and contain many more oxygen vacancies (valence states can reverse from +3 to +4) which allow them to be much more efficient than endogenous antioxidants (*132*). Both in vitro and in vivo studies have concluded CeO_2 nanoparticles offer significant protection from ionizing radiation, while demonstrating low toxicity and no serious side-effects. Cerium oxide nanoparticles have been shown to protect the gastrointestinal epithelium and lung tissue against radiation damage in mice and have been shown to be effective radioprotectants in pre-clinical studies (*132*, *136*, *137*).

3b. Targeting Radiosensitizing Nanoparticles to Tumor Sites

Radiosensitization is the leading concept behind chemoradiotherapy, or the concurrent administration of chemotherapy and radiotherapy, which is a standard treatment regimen for many cancers including head and neck, lung, esophageal, gastric, rectal, anal, and cervical cancers (*92*, *138*). Currently, clinical radiosensitizers are comprised mainly of chemotherapeutics (e.g. DTX); however, these small molecules are limited by solubility issues and undesirable side effects, leading to the development of new nanoparticle-based formulations (*139*).

Many research groups have formulated DTX-based nanoplatforms, as DTX has been clinically shown to be one of the most effective radiosensitizers. However, it can cause severe cardiac toxicity. Nanoparticle therapeutic carriers are capable of targeted treatments of cancers as they can be actively (surface ligands) or passively targeted (enhanced permeability and retention (EPR) effect) (*92*, *139*). BIND Therapeutics are currently in phase 2 clinical trials with their nano-radiosensitizer, BIND-014. BIND-014 is a polymer (PLA-PEG (Polylactic acid-Polyethylene glycol conjugate) or PLGA-PEG) based nanoparticle containing chemotherapeutic DTX, and a surface ligand targeting PSMA (prostate specific membrane antigen), a transmembrane glycoprotein that preferentially expresses on prostate cancer cells (*140*, *141*). The BIND Therapeutics company has demonstrated that this formulation has favorable pharmacokinetics and demonstrates safety in humans, while selectively inhibiting tumor growth to reduce systemic toxicities.

Many similar polymer-based nanoparticles have been formulated and used in pre-clinical studies that demonstrate efficacy of nanoparticle formulations of DTX for cancer treatment which enabled the rapid translation of the technology (*92*). Polymers are generally chosen for their biocompatibility and biodegradable properties. Werner et al. demonstrated that folate targeting PLGA/DTX nanoparticles preferentially accumulate in tumor tissue over non-targeted PLGA/DTX nanoparticles (*92*). The incubation time of the radiosensitizer prior to radiation therapy affected the outcome. As nanoparticles tend to release drugs slowly, optimal effects were seen with incubation times of up to 12 hours in vivo as compared to DTX's one hour incubation time, demonstrating that timing of

irradiation can be critical to the efficacy of radiosensitization. This suggests that each nanoparticle formulation has an optimal time for radiosensitization which can be crucial in designing more translatable platforms.

Highly specific tumor-targeting can be achieved by surface conjugation of antibodies to markers overexpressed in tumors (e.g. HER2, folate, EGF). While they have been shown to enhance radiation therapy in cancer, GNP also serve as high-Z imaging contrast agents for real-time dose tracking (*142*). Despite the differences in research parameters, GNPs have been shown to be highly effective in radiosensitization of many cancers. They have even crossed the blood brain barrier for targeted glioblastoma multiform tumor radiosensitization (*143*, *144*). Although their multifunctional potential and mechanistic safety at varying radiation doses still needs to be explored, active studies are currently underway to move these potential theranostic agents into the clinic (*142*).

3c. Better Treatment Planning System

Cancer chemoradiotherapy strategies are increasingly becoming more innovative and effective as knowledge of cellular and molecular tumor biology, tumor pathophysiology, and tumor microenvironment becomes more understood. Characterizing the tumor microenvironment prior to and post treatment is crucial in optimizing radiotherapy. As tumors are highly heterogeneous and treatment response varies greatly based on the patient's genetics, the concept of personalized medicine has been extremely attractive to clinicians. A multi-modal approach requires careful pretreatment strategizing for efficient and timely therapy monitoring to maximize patient outcome on an individual basis.

Functional and molecular imaging techniques play a key role for exploring and understanding the underlying mechanisms of cancer biology and pathways to optimize the best form of treatment for each individual. These imaging techniques allow for non-invasive characterization of tissues in vivo using different modalities (e.g. CT, MRI, PET, OI) (*145*). Molecularly targeted agents can focus on tumor cell proliferation, angiogenesis, and cell death. Molecular MRI applies targeted gadolinium (Gd) or iron (Fe)-based contrast agents for depiction of molecular processes in vivo using antibodies, peptides, or peptidomimetics. Gd-based nanoparticles can be conjugated to biological targeting moieties to achieve highly specific binding (*145*). Serres et al. developed a targeted iron oxide nanoparticle that enables imaging of endothelial vascular cell adhesion molecule-1 (VCAM-1), a molecule upregulated on vessels of cerebral metastases. Using the targeted particles, it was possible to detect brain metastases substantially earlier than with the current clinical Gd-based contrast agent. It was concluded that this approach represents a highly sensitive method for the early detection of brain metastasis with the potential for clinical translation (*146*).

4. Enhancing Imaging Efficacy

The success of radiation therapy relies immensely on the accuracy of imaging. The three basic steps involved in modern day radiotherapy are imaging,

treatment planning and treatment delivery (*147*). The imaging steps provide patient's structural and anatomical information using computed tomography (CT) (*148*). This information is transferred to a treatment planning system in which tumor lesions are identified and target volume is defined. After a complex assessment of several factors, the patient is irradiated. Thus, both the steps of planning and delivery are entirely dependent on the quality and accuracy of the imaging. The precision in defining the target volume determines the outcome of treatment, as well as non-specific toxicity to normal tissues. The uncertainty in target volume can be minimized by careful assessment of morphology, movement, and molecular profiling of the tumor (*149*).

The morphology of the tumor can help define the gross target volume (GTV) using advanced CT, ultrasound and MR imaging. Increasing the accuracy of GTV not only requires high resolution multimodal imaging techniques using combined PET/CT and SPECT imaging systems, but also requires novel contrast enhancement imaging agents to generate 2D/3D images of the tumor. The use of multimodality imaging provides a more reliable tumor volume, eventually leading to a better definitive local control.

The role of nanoparticles in providing multimodal imaging platforms has been well-studied and several promising platforms have been reported (*84*, *150–152*). Here, the focus will be on the imaging platform in conjunction with radiation therapy. Each imaging modality has its own advantage associated with localization, morphology and pathology. Thus, the use of multimodal imaging provides more reliable data on tumor morphology and accurate diagnosis.

X-ray Imaging Contrast Enhancing Agents

The basic principle of contrast enhancement relies on increasing the visibility of internal organs by changing the contrast between different tissues. The contrast agents for X-ray imaging absorb the incoming X-rays either more or less than absorption by other tissues (*153*). As described earlier, the absorption rate of X-rays depends on the atomic number and density of the materials used. Thus, again high Z-materials demonstrate superior X-ray attenuation ability to higher K-edge effect (*154*). The K-edge effect can be described as a photoelectric effect which occurs due to the absorption of photons which have energy just above the binding energy of the K-shell electron of the atom interacting with photons. For example, when the energy of incoming X-rays exceeds the binding energy of the K-shell electron of the Iodine, then only these electrons can be ejected from the atom and thus lead to the K-edge absorption phenomena.

4a. Gold Nanoparticles as CT Contrast Agents

Gold nanoparticles have several advantages over conventional iodine based contrast agents such as high stability, higher Z-number and absorption coefficient (5.16 cm^2/g and 1.94 cm^2/g respectively) (*75*, *155*). Gold is known to have 2.7 times more contrast per unit weight than iodine. Hainfield et al. have use GNPs

for contrast enhancements in mice injected intravenously with 1.9nm GNPs (*75*). Kim et al. and Cai et al. have used PEGylated GNPs as vascular contrast enhancement agents with plasma half-life of 12 hrs and 14.6 hrs respectively (*156*, *157*). The multimodality of GNPs was exploited recently by Miladi et al. where GNPs were fabricated by conjugating MR contrast agents on the surface of GNPs (*158*). Ultrasmall GNPs were modified with DTDTPA, a Gd chelating agent, to impart CT and MR imaging capability. The study showed the assessment of irradiation was based on the MR imaging in rats with 9L-gliosarcomas. Several other reports were focused on developing GNPs based CT/MR contrast agents by conjugating various ligands on GNPs surface (*154*, *159*).

Similarly, instead of Gd, which imparts positive contrast in MR, a hybrid nanoparticle system composed of a gold shell and iron oxide (negative contrast agent) core was reported (*160*). Sun et al. studied gold nanorods functionalized with Gd chelates for MR and CT bimodal imaging and showed significant enhancement in both CT and MR signal with functionalized GNRs (*161*). The further extension of incorporation of different imaging modalities into a single platform was studied by Schooneveld et al. in which GNP cores were stabilized by silica shells which were further conjugated with the optical contrast agent, cy5.5, and MR contrast agent, Gd chelates (*162*). The studies showed highly sensitive in vivo signal enhancement in the liver by 24% and 50% using MRI and CT at very low concentrations of nanoparticles. Apart from GNPs, silver and platinum based nanoparticles were also reported as contrast enhancement agents in X-ray imaging (*163*, *164*).

4b. Rare Earth Doped Nanoparticles as Contrast Agents

The K-edge value for rare earth element like ytterbium (Yb) (61 KeV) matches with the X-ray spectrum and thus nanoparticles doped with Yb can provide higher X-ray absorption than Au, platinum (Pt), bismuth (Bi), or tantalum (Ta) based CT contrast agents at 120 KVp (*165*). The upconversion nanoparticles doped with Yb and Gd, not only provided CT contrast enhancements, but also were capable of upconversion luminescence which provided greater penetration depths, reduced background and lowered phototoxicities. Since iodine is used clinically as CT contrast agent, the conjugation of iodine precursor 5-amino-2,4,6-triiodoisophthalic acid to upconversion nanoparticles was reported by Zhang et al. The studies reported that the intravenous injection of UCNPs@SiO_2-I/PEG (upconversion nanoparticles with a coating of SiO_2-I conjugate) showed a prolonged circulation of iodine with an added fluorescence imaging modality using upconversion luminescence (*166*). Cheung et al. reported the use of Gd-based nanoparticles consisting of $NaGdF_4$ or a mixture of GdF_3 and CeF_3 stabilized by polyacrylic acid for combined MRI and CT imaging (*167*). The results showed that nanoaggregates displayed higher attenuation at energies below 30 keV and above 50 keV when compared with iopromide and Gd^{3+}-DTPA complex at all X-ray energies. Poly vinly pyrrolidone (PVP) stabilized Gd_2O_3 microparticles were shown earlier as excellent contrast enhancement agents in CT by Havoron et al (*168*).

Recently, a binary contrast agent based on combining the two different CT contrast agents in a single nanoplatform was reported by Liu et al (*169*). This formulation combines a high K-edge yerbium (Yb) (61 KeV) which is responsive to higher voltage and barium (Ba) (37 KeV) which is responsive to a low voltage (*169*). This example clearly demonstrated the potential of nanoparticles in combining different species with varying properties in a unique platform which have superior properties compared to the individual components. The binary contrast agent composed of $BaYbF_5$@SiO_2@PEG ($BaYbF_5$ core nanoparticles coated with layer of SiO_2 futher coated with PEG) not only provided much higher CT contrast efficacy compared to clinical iodinated agents and nanoparticle formulation with a single contrast element, but also maintained high X-ray attenuation at different voltages.

4c. Bismuth-Based Nanoparticles as Contrast Agents

The Weissleder group reported polymer coated Bi_2S_3 nanoparticles for contrast enhancement in CT (*170*). The oleic acid stabilized 2-3 nm sized nanoparticles were further stabilized in aqueous media by the ligand exchange method using PVP. The intravenous administration of these PVP–Bi_2S_3 nanoparticles showed contrast enhancements of up to 1 hour in the heart and 4 hours in the liver and spleen, whereas when compared with Iobitridol, no enhancement was observed even at 3 minutes post intravenous administration. Sailor et al. also reported targeted Bi_2S_3 nanoparticles for imaging breast cancer (*171*). The bismuth (Bi) encapsulated polymeric nanoparticle formulation was studied by Lanza's group. They showed several-fold enhancement in the CT signal, in vivo, at very low concentrations (*172*).

Apart from GNPs and Bi, platinum (Pt)-, holmium (Ho)- and tantalum (Ta)-based nanoparticles have also been investigated as CT contrast agents (*164*, *173*, *174*). However, despite good contrast enhancement in imaging, acceptable safety profiles and long circulation times in vivo, there are several parameters which need to be optimized to further enhance the efficacy of these new generations of nanoparticles. The size, shape, and surface properties of nanoparticles determines the interaction of nanoparticles with biological systems and thus it is critical to engineer these nanoparticles by considering the parameters associated with applications in which these nanoparticles will be used.

Biological Fate and Toxicological Implications of Nanoparticles

The engineering of nanoparticles to achieve multifunctionality has led to complex nanoparticle based formulations. These complex formulations must be assessed not only in terms of their functional properties like therapeutic or imaging efficacy, but also in terms of safety and compatibility in biological systems. The three basic components which play a tremendous role in determining the biological fate of a drug subtance, pharmacokinetics, and immune compatibility include size, shape and surface properties (*30*). Apart from this, a careful

In The Science and Function of Nanomaterials: From Synthesis to Application; Harper-Leatherman, et al.;

nanoparticle design should consider the disease type, microenvironment of the disease site, mode of interaction with non-target organs and the fate of these nanoparticles in an in vivo environment (*29*, *30*).

It has been established that small sized nanoparticles (less than 6 nm) clear via renal excretion post intravenous administration whereas larger nanoparticles (greater than 6 nm) accumulate in the RES (Reticuloendothelial System) leading to less tumor accumulation and undesirable side effects (*27*). Larger sized nanoparticles with appropriate surface functionalization with amphiphilic polymers like polyethylene glycol (PEG) are above the renal filtration threshold and possess long blood half-lives. The fate of these nanoparticles relies either on the degradation of nanoparticles to smaller components which can be excreted via the renal route or gradual RES uptake which follows a slow hepatobiliary excretion (*28*, *175*).

The surface of the nanoparticles can be carefully grafted with amphiphilic polymers like polyethylene glycol to modulate the distribution and pharmacokinetics of the nanoparticles in systemic circulation (*176*). The surface properties also determine if the nanoparticles will elicit any immunogenic responses once injected in systemic circulation. The composition of nanoparticles, especially those containing heavy metals, which are known to cause acute or chronic toxicities, must be assessed carefully for any adverse reproductive risks, immunotoxicity, and carcinogenicity to minimize unintended side effects (*177*). Biodistribution and clearance profiles are of paramount importance for such side effects (*178*). Currently, third generation nanoparticles are being engineered based on the difficult lessons concerning specific limitations of particles for different biological applications learned from the previous two generations' engineering (*30*).

Conclusions

The development of nanoparticles for applications in radiation oncology is still in the early stages, possibly due to the challenge of preparing nanoparticles especially for this purpose. In targeting different diseased sites for delivering small molecular inhibitors, drugs and imaging agents must fulfill the following criteria simultaneously: (1) excellent biocompatibility; (2) high contrast efficacy; (3) cost effectiveness; (4) small size; 5) long in vivo circulation time; and (6) long-term colloidal stability in the physiological environment. As research technology continues to improve, high-throughput screening is capable of testing thousands of potential therapeutic candidates. As seen from the results with different nanoparticles, therapeutic effects vary greatly based on nanoparticle formulation (size, surface chemistry, targeting moieties, and drug concentration) and dose timing. As new research tools develop and individual tumor microbiology is characterized, optimized nanotherapeutics can be expected to provide a novel approach for safer and more effective personalized treatments in radiation oncology.

Appendix 1

Table 1. List of Abbreviations

RT	Radiation Therapy
IMRT	Intensity-Modulated Radiation Therapy
IGRT	Image Guided Radiation Therapy
SABR	Stereotactic Body Radiation Therapy
PT	Proton Therapy
XRT	External Beam Radiation Therapy
PSA	Prostate Specific Antigen
BRT	Brachytherapy
DEF	Dose Enhancement Factor
GNPs	Gold Nanoparticles
DTX	Docetaxel
DTPA	Diethylene Triamine Pentaacetic Acid
PLGA	Poly(lactic-co-glycolic acid)
KB	Head and Neck tumor cell line
INCeRT	Implantable Nanoplatforms for Chemo-Radiation Therapy
BIS-IGRT	Biological In Situ-Image Guided Radiation Therapy
SOD2	Super Oxide Dismutase 2
AKT	Protein kinase B
PI3-K	Phosphatidylinositol-4,5-bisphosphate 3-kinase
MAPK	Mitogen-Activated Protein Kinases
ERK	Extracellular Signal-Regulated Kinases
miRNA	Micro-RNA
EGFR	Epidermal Growth Factor Receptor
CT	Computed Tomography
MRI	Magnetic Resonance Imaging
PET	Positron Emission Tomography
OI	Optical Imaging
VCAM-1	Vascular Cell Adhesion Molecule-1
GTV	Gross Target Volume
PVP	Poly vinly pyrrolidone

Continued on next page.

Table 1. (Continued). List of Abbreviations

RES	Reticuloendothelial System
PEG	polyethylene glycol

Appendix 2

Table 2. Energy Units in Radiation Oncology

Energy Unit	*Expression in joules*
1 KeV	1.602X10-16 J
1MeV	1.602X10-13 J
1 Vp	1 J/C
1 Gy	1 J/kg

References

1. Del Regato, J. A. *Radiological Oncologists: The Unfolding of a Medical Specialty*; Radiology Centennial; Reston, VA, 1993.
2. Eisenberg, R. L. *Radiology: An Illustrated History*; Mosby Year Book: St. Louis, MO, 1992.
3. Delaney, G.; Jacob, S.; Featherstone, C.; Barton, M. *Cancer* **2005**, *104*, 1129–1137.
4. Owen, J. B.; Coia, L. R.; Hanks, G. E. *Int. J. Radiat. Oncol. Biol. Phys.* **1992**, *24*, 983–986.
5. Radford, I. R. *Int. J. Radiat. Biol. Relat. Stud. Phys. Chem. Med.* **1985**, *48*, 45–54.
6. Halliwell, B.; Aruoma, O. I. *FEBS Lett.* **1991**, *281*, 9–19.
7. Tsiamas, P.; Liu, B.; Cifter, F.; Ngwa, W. F.; Berbeco, R. I.; Kappas, C.; Theodorou, K.; Marcus, K.; Makrigiorgos, M. G.; Sajo, E.; Zygmanski, P. *Phys. Med. Biol.* **2013**, *58*, 451–464.
8. Begg, A. C.; Stewart, F. A.; Vens, C. *Nat. Rev. Cancer* **2011**, *11*, 239–253.
9. Bhide, S. A.; Nutting, C. M. *BMC Med.* **2010**, *8*, 25–29.
10. Nguyen, P. L.; D'Amico, A. V.; Lee, A. K.; Suh, W. W. *Cancer* **2007**, *110*, 1417–1428.
11. Zietman, A. L.; Bae, K.; Slater, J. D.; Shipley, W. U.; Efstathiou, J. A.; Coen, J. J.; Bush, D. A.; Lunt, M.; Spiegel, D. Y.; Skowronski, R.; Jabola, B. R.; Rossi, C. J. *J. Clin. Oncol.* **2010**, *28*, 1106–1111.
12. Kuban, D. A.; Tucker, S. L.; Dong, L.; Starkschall, G.; Huang, E. H.; Cheung, M. R.; Lee, A. K.; Pollack, A. *Int. J. Radiat. Oncol., Biol., Phys.* **2008**, *70*, 67–74.
13. Nguyen, P. L.; Chen, M. H.; D'Amico, A. V.; Tempany, C. M.; Steele, G. S.; Albert, M.; Cormack, R. A.; Carr-Locke, D. L.; Bleday, R.; Suh, W. W. *Cancer* **2007**, *110*, 1485–1492.

14. Peeters, S. T.; Heemsbergen, W. D.; Van Putten, W. L.; Slot, A.; Tabak, H.; Mens, J. W.; Lebesque, J. V.; Koper, P. C. *Int. J. Radiat. Oncol., Biol., Phys.* **2005**, *61*, 1019–1034.
15. Litzenberg, D. W.; Balter, J. M.; Hadley, S. W.; Sandler, H. M.; Willoughby, T. R.; Kupelian, P. A.; Levine, L. *Int. J. Radiat. Oncol., Biol., Phys.* **2006**, *65*, 548–553.
16. Li, H. S.; Chetty, I. J.; Enke, C. A.; Foster, R. D.; Willoughby, T. R.; Kupellian, P. A.; Solberg, T. D. *Int. J. Radiat. Oncol., Biol., Phys.* **2008**, *71*, 801–812.
17. Sovik, A.; Malinen, E.; Olsen, D. R. *Int. J. Radiat. Oncol., Biol., Phys.* **2009**, *73*, 650–658.
18. Burri, R. J.; Stone, N. N.; Unger, P.; Stock, R. G. *Int. J. Radiat. Oncol., Biol., Phys.* **2010**, *77*, 1338–1344.
19. Keall, P. J.; Mageras, G. S.; Balter, J. M.; Emery, R. S.; Forster, K. M.; Jiang, S. B.; Kapatoes, J. M.; Low, D. A.; Murphy, M. J.; Murray, B. R.; Ramsey, C. R.; Van Herk, M. B.; Vedam, S. S.; Wong, J. W.; Yorke, E. *Med. Phys.* **2006**, *33*, 3874–3900.
20. Brigger, I.; Dubernet, C.; Couvreur, P. *Adv. Drug Delivery Rev.* **2002**, *54*, 631–651.
21. Thakor, A. S.; Gambhir, S. S. *CA-Cancer J. Clin.* **2013**, *63*, 395–418.
22. Rieter, W. J.; Kim, J. S.; Taylor, K. M.; An, H.; Lin, W.; Tarrant, T.; Lin, W. *Angew. Chem.* **2007**, *46*, 3680–3682.
23. Kumar, R.; Nyk, M.; Ohulchanskyy, T. Y.; Flask, C. A.; Prasad, P. N. *Adv. Funct. Mater.* **2009**, *19*, 853–859.
24. Moghimi, S. M.; Hunter, A. C.; Murray, J. C. *Pharmacol. Rev.* **2001**, *53*, 283–318.
25. Lee, D. E.; Koo, H.; Sun, I. C.; Ryu, J. H.; Kim, K.; Kwon, I. C. *Chem. Soc. Rev.* **2012**, *41*, 2656–2672.
26. Kumar, R.; Roy, I.; Hulchanskyy, T. Y.; Goswami, L. N.; Bonoiu, A. C.; Bergey, E. J.; Tramposch, K. M.; Maitra, A.; Prasad, P. N. *ACS Nano* **2008**, *2*, 449–456.
27. Choi, H. S.; Liu, W.; Misra, P.; Tanaka, E.; Zimmer, J. P.; Ipe, B. I.; Bawendi, M. G.; Frangioni, J. V. *Nat. Biotechnol.* **2007**, *25*, 1165–1170.
28. Kumar, R.; Roy, I.; Ohulchanskky, T. Y.; Vathy, L. A.; Bergey, E. J.; Sajjad, M.; Prasad, P. N. *ACS Nano* **2010**, *4*, 699–708.
29. Albanese, A.; Tang, P. S.; Chan, W. C. W. *Annu. Rev. Biomed. Eng.* **2012**, *14*, 1–16.
30. Kumar, R.; Korideck, H.; Ngwa, W.; Berbeco, R. I.; Makrigiorgos, G. M.; Sridhar, S. *Transl. Cancer. Res.* **2013**, *2*, 228–239.
31. Lawrence, T. S.; Blackstock, A. W.; McGinn, C. *Semin. Radiat. Oncol.* **2003**, *13*, 13–21.
32. Wilson, G. D.; Bentzen, S. M.; Harari, P. M. *Semin. Radiat. Oncol.* **2006**, *16*, 2–9.
33. Shewach, D. S.; Lawrence, T. S. *Invest. New Drugs* **1996**, *14*, 257–263.
34. Werner, M. E.; Copp, J. A.; Karve, S.; Cummings, N. D.; Sukumar, R.; Li, C. X.; Napier, M. E.; Chen, R. C.; Cox, A. D.; Wang, A. Z. *ACS Nano* **2011**, *5*, 8990–8998.

35. Hainfeld, J. F.; Slatkin, D. N.; Smilowitz, H. M. *Phys. Med. Biol.* **2004**, *49*, N309–N315.
36. Maeda, H. *Adv. Enzyme Regul.* **2001**, *41*, 189–207.
37. Mitra, S.; Gaur, U.; Ghosh, P. C.; Maitra, A. N. *J. Controlled Release* **2001**, *74*, 317–323.
38. Wang, M.; Thanou, M. *Pharmacol. Res.* **2010**, *62*, 90–99.
39. Debbage, P. *Curr. Pharm. Des.* **2009**, *15*, 153–172.
40. Matsudaira, H.; Ueno, A.; Furuno, I. *Radiat. Res.* **1980**, *84*, 144–148.
41. Kwatra, D.; Venugopal, A.; Shrikant, A. *Transl. Cancer. Res.* **2013**, *2*, 330–342.
42. Larson, D.; Bodell, W. J.; Ling, C.; Phillips, T. L.; Schell, M.; Shrieve, D.; Troxel, T. *Int. J. Radiat. Oncol., Biol., Phys.* **1989**, *16*, 171–176.
43. Howell, R. W. *Int. J. Radiat. Biol.* **2008**, *84*, 959–975.
44. Pignol, J. P.; Rakovitch, E.; Beachey, D.; Le Sech, C. *Int. J. Radiat. Oncol.* **2003**, *55*, 1082–1091.
45. Takakura, T. *Radiat. Environ. Biophys.* **1989**, *28*, 177–184.
46. Cheung, J. Y.; Tang, F. H. *Health Phys.* **2007**, *93*, 267–272.
47. Chattopadhyay, N.; Cai, Z. L.; Pignol, J. P.; Keller, B.; Lechtman, E.; Bendayan, R.; Reilly, R. M. *Mol. Pharmaceutics* **2010**, *7*, 2194–2206.
48. Ngwa, W.; Korideck, H.; Kassis, A. I.; Kumar, R.; Sridhar, S.; Makrigiorgos, G. M.; Cormack, R. A. *Nanomedicine* **2013**, *9*, 25–27.
49. Rahman, W. N.; Wong, C. J.; Ackerly, T.; Yagi, N.; Geso, M. *Australas. Phys. Eng. Sci. Med.* **2012**, *35*, 301–309.
50. Misawa, M.; Takahashi, J. *Nanomedicine* **2011**, *7*, 604–614.
51. Lasagna-Reeves, C.; Gonzalez-Romero, D.; Barria, M. A.; Olmedo, I.; Clos, A.; Sadagopa Ramanujam, V. M.; Urayama, A.; Vergara, L.; Kogan, M. J.; Soto, C. *Biochem. Biophys. Res. Commun.* **2010**, *393*, 649–655.
52. Hainfeld, J. F.; Dilmanian, F. A.; Slatkin, D. N.; Smilowitz, H. M. J *Pharm. Pharmacol.* **2008**, *60*, 977–985.
53. Chithrani, D. B.; Jelveh, S.; Jalali, F.; Van Prooijen, M.; Allen, C.; Bristow, R. G.; Hill, R. P.; Jaffray, D. A. *Radiat. Res.* **2010**, *173*, 719–728.
54. Chithrani, B. D.; Ghazani, A. A.; Chan, W. C. W. *Nano Lett.* **2006**, *6*, 662–668.
55. Chithrani, B. D.; Chan, W. C. W. *Nano. Lett.* **2007**, *7*, 1542–1550.
56. Hauck, T. S.; Ghazani, A. A.; Chan, W. C. W. *Small* **2008**, *4*, 153–159.
57. Choi, C. H. J.; Alabi, C. A.; Webster, P.; Davis, M. E. *Proc. Natl. Acad. Sci. U.S.A.* **2010**, *107*, 1235–1240.
58. Shukla, R.; Bansal, V.; Chaudhary, M.; Basu, A.; Bhonde, R. R.; Sastry, M. *Langmuir* **2005**, *21*, 10644–10654.
59. Mukherjee, P.; Bhattacharya, R.; Wang, P.; Wang, L.; Basu, S.; Nagy, J. A.; Atala, A.; Mukhopadhyay, D.; Soker, S. *Clin. Cancer Res.* **2005**, *11*, 3530–3534.
60. Regulla, D. F.; Hieber, L. B.; Seidenbusch, M. *Radiat. Res.* **1998**, *150*, 92–100.
61. Herold, D. M.; Das, I. J.; Stobbe, C. C.; Iyer, R. V.; Chapman, J. D. *Int. J. Radiat. Biol.* **2000**, *76*, 1357–1364.

62. Zheng, Y.; Hunting, D. J.; Ayotte, P.; Sanche, L. *Radiat. Res.* **2008**, *169*, 19–27.
63. Brun, E.; Sanche, L.; Sicard-Roselli, C. *Colloids. Surf., B.* **2009**, *72*, 128–134.
64. Zhang, X. D.; Wu, D.; Shen, X.; Chen, J.; Sun, Y. M.; Liu, P. X.; Liang, X. J. *Biomaterials* **2012**, *33*, 6408–6419.
65. Cho, S. H. *Phys. Med. Biol.* **2005**, *50*, N163–N173.
66. Jones, B. L.; Krishnan, S.; Cho, S. H. *Med. Phys.* **2010**, *37*, 3809–3816.
67. Rahman, W. N.; Bishara, N.; Ackerly, T.; He, C. F.; Jackson, P.; Wong, C.; Davidson, R.; Geso, M. *Nanomedicine* **2009**, *5*, 136–142.
68. Zhang, X.; Xing, J. Z.; Chen, J.; Ko, L.; Amanie, J.; Gulavita, S.; Pervez, N.; Yee, D.; Moore, R.; Roa, W. *Clin. Invest. Med.* **2008**, *31*, E160–E167.
69. Kong T, Z. J.; Wang, X.; Yang, X.; Jing, Y.; McQuarrie, S.; McEwan, A.; Roa, W.; Chen, J.; Xing, J. Z. *Small* **2008**, *4*, 1537–1543.
70. Berbeco, R. I.; Korideck, H.; Ngwa, W.; Kumar, R.; Patel, J.; Sridhar, S.; Johnson, S.; Price, B. D.; Kimmelman, A.; Makrigiorgos, G. M. *Radiat. Res.* **2012**, *178*, 604–608.
71. Berbeco, R. I.; Ngwa, W.; Makrigiorgos, G. M. *Int. J. Radiat. Oncol.* **2011**, *81*, 270–276.
72. Ngwa, W.; Makrigiorgos, G. M.; Berbeco, R. I. *Phys. Med. Biol.* **2012**, *57*, 6371–6380.
73. Butterworth, K. T.; Coulter, J. A.; Jain, S.; Forker, J.; McMahon, S. J.; Schettino, G.; Prise, K. M.; Currell, F. J.; Hirst, D. G. *Nanotechnology* **2010**, *21*, 295101–295109.
74. Jain, S.; Coulter, J. A.; Hounsell, A. R.; Butterworth, K. T.; McMahon, S. J.; Hyland, W. B.; Muir, M. F.; Dickson, G. R.; Prise, K. M.; Currell, F. J.; O'Sullivan, J. M.; Hirst, D. G. *Int. J. Radiat. Oncol.* **2011**, *79*, 531–539.
75. Hainfeld, J. F.; Slatkin, D. N.; Focella, T. M.; Smilowitz, H. M. *Br. J. Radiol.* **2006**, *79*, 248–253.
76. Hainfeld, J. F.; Dilmanian, F. A.; Zhong, Z.; Slatkin, D. N.; Kalef-Ezra, J. A.; Smilowitz, H. M. *Phys. Med. Biol.* **2010**, *55*, 3045–3059.
77. Chang, M. Y.; Shiau, A. L.; Chen, Y. H.; Chang, C. J.; Chen, H. H.; Wu, C. L. *Cancer Sci.* **2008**, *99*, 1479–1484.
78. Liu, C. J.; Wang, C. H.; Chen, S. T.; Chen, H. H.; Leng, W. H.; Chien, C. C.; Wang, C. L.; Kempson, I. M.; Hwu, Y.; Lai, T. C.; Hsiao, M.; Yang, C. S.; Chen, Y. J.; Margaritondo, G. *Phys. Med. Biol.* **2010**, *55*, 931–945.
79. Cho, S. H.; Jones, B. L.; Krishnan, S. *Phys. Med. Biol.* **2009**, *54*, 4889–4905.
80. Alric, C.; Serduc, R.; Mandon, C.; Taleb, J.; Le Duc, G.; Le Meur-Herland, A.; Billotey, C.; Perriat, P.; Roux, S.; Tillement, O. *Gold Bull.* **2008**, *41*, 90–97.
81. Al Zaki, A.; Joh, D.; Cheng, Z. L.; De Barros, A. L. B.; Kao, G.; Dorsey, J.; Tsourkas, A. *ACS Nano* **2014**, *8*, 104–112.
82. Masood, R.; Roy, I.; Zu, S.; Hochstim, C.; Yong, K. T.; Law, W. C.; Ding, H.; Sinha, U. K.; Prasad, P. N. *Integr. Biol.* **2012**, *4*, 132–141.
83. Miladi, I.; Duc, G. L.; Kryza, D.; Berniard, A.; Mowat, P.; Roux, S.; Taleb, J.; Bonazza, P.; Perriat, P.; Lux, F.; Tillement, O.; Billotey, C.; Janier, M. *J. Biomater. Appl.* **2013**, *28*, 385–394.

84. Le Duc Geraldine, M. I.; Alric, C.; Mowat, P.; Braeuer-Krisch, E.; Bouchet, A.; Khalil, E.; Billotey, C.; Janier, M.; Lux, F.; Epicier, T.; Perriat, P.; Roux, S.; Tillement, O. *ACS Nano* **2011**, *5*, 9566–9574.
85. Ma, J.; Xu, R.; Sun, J.; Zhao, D.; Tong, J.; Sun, X. *J. Nanosci. Nanotechnol.* **2013**, *13*, 1472–1475.
86. Maggiorella, L.; Barouch, G.; Devaux, C.; Pottier, A.; Deutsch, E.; Bourhis, J.; Borghi, E.; Levy, L. *Future Oncol.* **2012**, *8*, 1167–1181.
87. Huang, G.; Chen, H.; Dong, Y.; Luo, X.; Yu, H.; Moore, Z.; Bey, E. A.; Boothman, D. A.; Gao, J. *Theranostics* **2013**, *3*, 116–126.
88. Shen, L. F.; Chen, J.; Zeng, S.; Zhou, R. R.; Zhu, H.; Zhong, M. Z.; Yao, R. J.; Shen, H. *Mol. Cancer Ther.* **2010**, *9*, 2123–2130.
89. Morgan, M. A.; Parsels, L. A.; Maybaum, J.; Lawrence, T. S. *Clin. Cancer Res.* **2008**, *14*, 6744–6750.
90. Lawrence, T. S.; Eisbruch, A.; Shewach, D. S. *Semin. Oncol.* **1997**, *24*, S7-24–S7-28.
91. Tishler, R. B.; Schiff, P. B.; Geard, C. R.; Hall, E. J. *Int. J. Radiat. Oncol., Biol., Phys.* **1992**, *22*, 613–617.
92. Werner, M. E.; Copp, J. A.; Karve, S.; Cummings, N. D.; Sukumar, R.; Napier, M.; Chen, R. C.; Cox, A. D.; Wang, A. Z. *ACS Nano* **2011**, *5*, 8990–8998.
93. Wang, A. Z.; Yuet, K.; Zhang, L.; Gu, F. X.; Huynh-Le, M.; Radovic-Moreno, A. F.; Kantoff, P. W.; Bander, N. H.; Langer, R.; Farokhzad, O. C. *Nanomedicine* **2010**, *5*, 361–368.
94. Jin, C.; Bai, L.; Wu, H.; Tian, F.; Guo, G. *Biomaterials* **2007**, *28*, 3724–3730.
95. Werner, M. E.; Cummings, N. D.; Sukumar, R.; Sethi, M.; Wang, E. C.; Moore, D. T.; Dees, E. C.; Wang, A. Z. *Int. J. Radiat. Oncol., Biol., Phys.* **2013**, *86*, 463–468.
96. Karve, S.; Werner, M. E.; Sukumar, R.; Cummings, N. D.; Copp, J. A.; Wang, E. C.; Li, C.; Sethi, M.; Chen, R. C.; Pacold, M. E.; Wang, A. Z. *Proc. Natl. Acad. Sci. U.S.A.* **2012**, *109*, 8230–8235.
97. Lee, W. R. *Rev. Urol.* **2004**, *6*, S49–S56.
98. Friedland, J. L.; Freeman, D. E.; Masterson-McGary, M. E.; Spellberg, D. M. *Technol. Cancer Res. Treat.* **2009**, *8*, 387–392.
99. Sylvester, J. E.; Grimm, P. D.; Eulau, S. M.; Takamiya, R. K.; Naidoo, D. *Brachytherapy* **2009**, *8*, 197–206.
100. Cormack, R. A.; Sridhar, S.; Suh, W. W.; D'Amico, A. V.; Makrigiorgos, G. M. *Int. J. Radiat. Oncol., Biol., Phys.* **2010**, *76*, 615–623.
101. Nagesha, D. K.; Tada, D. B.; Stambaugh, C. K.; Gultepe, E.; Jost, E.; Levy, C. O.; Cormack, R.; Makrigiorgos, G. M.; Sridhar, S. *Phys. Med. Biol.* **2010**, *55*, 6039–6052.
102. Kumar, R.; Belz, J.; Markovic, S.; Korideck, H.; Ngwa, W. F.; Niedre, M.; Berbeco, R. I.; Cormack, R.; Makrigiorgos, G. M.; Sridhar, S. *Mol. Cancer Ther.* **2013**, *12*, A82.
103. Wang, Z.; Werner, M. E.; Byrne, J. D.; Chen, R. C.; Karve, S. S.; DeSimone, J. Delivery for Brachytherapy and Associated Methods. International PCT Patent Application No. PCT/US2010/053357, 2011.

104. Nordsmark, M.; Bentzen, S. M.; Rudat, V.; Brizel, D.; Lartigau, E.; Stadler, P.; Becker, A.; Adam, M.; Molls, M.; Dunst, J.; Terris, D. J.; Overgaard *Radiother. Oncol.* **2005**, *77*, 18–24.
105. Kim, J. J.; Tannock, I. F. *Nat. Rev. Cancer* **2005**, *5*, 516–525.
106. West, C. M.; Davidson, S. E.; Roberts, S. A.; Hunter, R. D. *Br. J. Cancer* **1993**, *68*, 819–823.
107. Withers, H. R.; Taylor, J. M.; Maciejewski, B. *Acta. Oncol.* **1988**, *27*, 131–146.
108. Ahn, G. O.; Tseng, D.; Liao, C. H.; Dorie, M. J.; Czechowicz, A.; Brown, J. M. *Proc. Natl. Acad. Sci. U.S.A.* **2010**, *107*, 8363–8368.
109. Jackson, S. P.; Bartek, J. *Nature* **2009**, *461*, 1071–1078.
110. Caldecott, K. W. *Nat. Rev. Genet.* **2008**, *9*, 619–631.
111. O'Driscoll, M.; Jeggo, P. A. *Nat. Rev. Genet.* **2006**, *7*, 45–54.
112. Kastan, M. B. *Mol. Cancer Res.* **2008**, *6*, 517–524.
113. Negrini, S.; Gorgoulis, V. G.; Halazonetis, T. D. *Nat. Rev. Mol. Cell Biol.* **2010**, *11*, 220–228.
114. Chalmers, A. J.; Lakshman, M.; Chan, N.; Bristow, R. G. *Semin. Radiat. Oncol.* **2010**, *20*, 274–281.
115. Loser, D. A.; Shibata, A.; Shibata, A. K.; Woodbine, L. J.; Jeggo, P. A.; Chalmers, A. J. *Mol. Cancer Ther.* **2010**, *9*, 1775–1787.
116. Tangutoori, S.; Koridec, H.; Makrigiorgos, M.; Cormack, R.; Sridhar, S. *Mol. Cancer Ther.* **2013**, *12*, A81.
117. Ullal, A. V.; Reiner, T.; Yang, K. S.; Gorbatov, R.; Min, C.; Issadore, D.; Lee, H.; Weissleder, R. *ACS Nano* **2011**, *5*, 9216–9224.
118. Li, L.; Ahmed, B.; Mehta, K.; Kurzrock, R. *Mol. Cancer Ther.* **2007**, *6*, 1276–1282.
119. Kirshner, J.; Jobling, M. F.; Pajares, M. J.; Ravani, S. A.; Glick, A. B.; Lavin, M. J.; Koslov, S.; Shiloh, Y.; Barcellos-Hoff, M. H. *Cancer Res.* **2006**, *66*, 10861–10869.
120. Qiao, Q.; Jiang, Y.; Li, G. *J. Pharmacol. Sci.* **2013**, *121*, 247–256.
121. Yallapu, M. M.; Maher, D. M.; Sundram, V.; Bell, M. C.; Jaggi, M.; Chauhan, S. C. *J. Ovarian Res.* **2010**, *3*, 11–22.
122. Ping, Y.; Jian, Z.; Yi, Z.; Huoyu, Z.; Feng, L.; Yuqiong, Y.; Shixi, L. *Med. Oncol.* **2010**, *27*, 715–721.
123. Pennati, M.; Millo, E.; Gandellini, P.; Folini, M.; Zaffaroni, N. *Curr. Top. Med. Chem.* **2012**, *12*, 69–78.
124. Gaca, S.; Reichert, S.; Rodel, C.; Rodel, F.; Kreuter, J. *J. Microencapsulation* **2012**, *29*, 685–694.
125. Phase Ib/II Study of Neoadjuvant Chemoradiotherapy With CRLX-101 and Capecitabine for Locally Advanced Rectal Cancer. http://clinicaltrials.gov/show/NCT02010567 (accessed July 2014).
126. Harfouche, R.; Basu, S.; Soni, S.; Hentschel, D. M.; Mashelkar, R. A.; Sengupta, S. *Angiogenesis* **2009**, *12*, 325–338.
127. Patankar, N. A.; Waterhouse, D.; Strutt, D.; Anantha, M.; Bally, M. B. *Invest. New Drugs* **2013**, *31*, 46–58.
128. Stone, H. B.; Moulder, J. E.; Coleman, C. N.; Ang, K. K.; Anscher, M. S.; Barcellos-Hoff, M. H.; Dynan, W. S.; Fike, J. R.; Grdina, D. J.;

Greenberger, J. S.; Hauer-Jensen, M.; Hill, R. P.; Kolesnick, R. N.; Macvittie, T. J.; Marks, C.; McBride, W. H.; Metting, N.; Pellmar, T.; Purucker, M.; Robbins, M. E.; Schiestl, R. H.; Seed, T. M.; Tomaszewski, J. E.; Travis, E. L.; Wallner, P. E.; Wolpert, M.; Zaharevitz, D. *J. Radiat. Res.* **2004**, *162*, 711–728.
129. Vávrová, J.; Řezáčová, M.; Pejchal, J. *J. Appl. Biomed.* **2012**, *10*, 1–8.
130. Baker, C. H. *Transl. Cancer Res.* **2013**, *2*, 343–358.
131. France, H. G., Jr.; Jirtle, R. L.; Mansbach, C. M., 2nd *Gastroenterology* **1986**, *91*, 644–650.
132. Koukourakis, M. I. *Brit. J. Radiol.* **2012**, *85*, 313–330.
133. Pamujula, S.; Kishore, V.; Rider, B.; Agrawal, K. C.; Mandal, T. K. *Int. J. Radiat. Biol.* **2008**, *84*, 900–908.
134. Trajkovic, S.; Dobric, S.; Jacevic, V.; Dragojevic-Simic, V.; Milovanovic, Z.; Dordevic, A. *Colloids Surf., B.* **2007**, *58*, 39–43.
135. Tarnuzzer, R. W.; Colon, J.; Patil, S.; Seal, S. *Nano Lett.* **2005**, *5*, 2573–2577.
136. Colon, J.; Herrera, L.; Smith, J.; Patil, S.; Komanski, C.; Kupelian, P.; Seal, S.; Jenkins, D. W.; Baker, C. H. *Nanomedicine-Uk* **2009**, *5*, 225–231.
137. Colon, J.; Hsieh, N.; Ferguson, A.; Kupelian, P.; Seal, S.; Jenkins, D. W.; Baker, C. H. *Nanomedicine* **2010**, *6*, 698–705.
138. Seiwert, T. Y.; Salama, J. K.; Vokes, E. E. *Nat. Clin. Pract. Oncol.* **2007**, *4*, 156–171.
139. Sanna, V.; Roggio, A. M.; Posadino, A. M.; Cossu, A.; Marceddu, S.; Mariani, A.; Alzari, V.; Uzzau, S.; Pintus, G.; Sechi, M. *Nanoscale Res. Lett.* **2011**, *6*, 260–268.
140. Hrkach, J.; Hoff, D. V.; Ali, M. M.; Andrianova, E.; Auer, J.; Campbell, T.; Witt, D. D.; Figa, M.; Figueiredo, M.; Horhota, A.; Low, S.; McDonnell, K.; Peeke, E.; Retnarajan, B.; Sabnis, A.; Schnipper, E.; Song, J. J.; Song, Y. H.; Summa, J.; Tompsett, D.; Troiano, G.; Hoven, T. V. G.; Wright, J.; LoRusso, P.; Kantoff, P. W.; Bander, N. H.; Sweeney, C.; Farokhzad, O. C.; Langer, R.; Zale, S. Preclinical Development and Clinical Translation of a PSMA-Targeted Docetaxel Nanoparticle with a Differentiated Pharmacological Profile. *Sci. Transl. Med.* **2012**, *4*, 128ra39.
141. BIND Therapeutics. http://www.bindtherapeutics.com/pipeline/BIND014.html (accessed 2012).
142. Dorsey, J. F.; Sun, L.; Joh, D. Y.; Witztum, A.; Zaki, A. A.; Kao, G. D.; Alonso-Basanta, M.; Avery, S.; Tsourkas, A.; Hahn, S. M. *Transl. Cancer Res.* **2013**, *2*, 280–291.
143. Mesbahi, A. Reports of practical oncology and radiotherapy. *J. Great Poland Cancer Center in Poznan and Polish Society of Radiation Oncology* **2010**, *15*, 176–180.
144. Joh, D. Y.; Sun, L.; Stangl, M.; Al Zaki, A.; Murty, S.; Santoiemma, P. P.; Davis, J. J.; Baumann, B. C.; Alonso-Basanta, M.; Bhang, D.; Kao, G. D.; Tsourkas, A.; Dorsey, J. F. *PLoS One* **2013**, *8*, e62425–e62434.
145. Cyran, C. C.; Paprottka, P. M.; Eisenblatter, M.; Clevert, D. A.; Rist, C.; Nikolaou, K.; Lauber, K.; Wenz, F.; Hausmann, D.; Reiser, M. F.; Belka, C.; Niyazi, M. *Radiat. Oncol.* **2014**, *9*, 3.

146. Serres, S.; Soto, M. S.; Hamilton, A.; McAteer, M. A.; Carbonell, W. S.; Robson, M. D.; Ansorge, O.; Khrapitchev, A.; Bristow, C.; Balathasan, L.; Weissensteiner, T.; Anthony, D. C.; Choudhury, R. P.; Muschel, R. J.; Sibson, N. R. *Proc. Natl. Acad. Sci. U.S.A.* **2012**, *109*, 6674–6679.
147. Khan, F. M. *The Physics of Radiation Therapy*, 3rd ed.; Lippincott Williams & Wilkins: Philadelphia, PA, 2003.
148. Chernak, E. S.; Rodriguez-Antunez, A.; Jelden, G. L.; Dhaliwal, R. S.; Lavik, P. S. *Radiology* **1975**, *117*, 613–614.
149. Parker, R. P.; Hobday, P. A.; Cassell, K. J. *Phys. Med. Biol.* **1979**, *24*, 802–809.
150. Lee, D.-E.; Koo, H.; Sun, I-C.; Ryu, J. H.; Kim, K.; Kwon, I. C. *Chem. Soc. Rev.* **2012**, *41*, 2656–2672.
151. Rieter, W. J.; Kim, J. S.; Taylor, K. M.; An, H.; Lin, W.; Tarrant, T.; Lin, W. *Angew. Chem., Int. Ed.* **2007**, *46*, 3680–3682.
152. Kumar, R.; Nyk, M.; Ohulchanskyy, T. Y.; Flask, C. A.; Prasad, P. N. *Adv. Funct. Mater.* **2009**, *19*, 853–859.
153. Kalender, W. A. *Phys. Med. Biol.* **2006**, *51*, R29–R43.
154. Popovtzer, R.; Agrawal, A.; Kotov, N. A.; Popovtzer, A.; Balter, J.; Carey, T. E.; Kopelman, R. *Nano Lett.* **2008**, *8*, 4593–4596.
155. Jakhmola, A.; Anton, N.; Vandamme, T. F. *Adv. Healthcare Mater.* **2012**, *1*, 413–431.
156. Kim, D.; Park, S.; Lee, J. H.; Jeong, Y. Y.; Jon, S. *J. Am. Chem. Soc.* **2007**, *129*, 12585–12585.
157. Cai, Q. Y.; Kim, S. H.; Choi, K. S.; Kim, S. Y.; Byun, S. J.; Kim, K. W.; Park, S. H.; Juhng, S. K.; Yoon, K. H. *Invest. Radiol.* **2007**, *42*, 797–806.
158. Miladi, I.; Alric, C.; Dufort, S.; Mowat, P.; Dutour, A.; Mandon, C.; Laurent, G.; Brauer-Krisch, E.; Herath, N.; Coll, J. L.; Dutreix, M.; Lux, F.; Bazzi, R.; Billotey, C.; Janier, M.; Perriat, P.; Le Duc, G.; Roux, S.; Tillement, O. *Small* **2014**, *10*, 1116–1124.
159. Luo, T.; Huang, P.; Gao, G.; Shen, G. X.; Fu, S.; Cui, D. X.; Zhou, C. Q.; Ren, Q. S. *Opt. Express* **2011**, *19*, 17030–17039.
160. Kim, D.; Yu, M. K.; Lee, T. S.; Park, J. J.; Jeong, Y. Y.; Jon, S. *Nanotechnology* **2011**, *22*, 155101–155107.
161. Sun, H.; Yuan, Q.; Zhang, B.; Ai, K.; Zhang, P.; Lu, L. *Nanoscale* **2011**, *3*, 1990–1996.
162. van Schooneveld, M. M.; Cormode, D. P.; Koole, R.; van Wijngaarden, J. T.; Calcagno, C.; Skajaa, T.; Hilhorst, J.; 't Hart, D. C.; Fayad, Z. A.; Mulder, W. J. M.; Meijerink, A. *Contrast Media Mol. Imaging* **2010**, *5*, 231–236.
163. Liu, H.; Sun, K.; Zhao, J. L.; Guo, R.; Shen, M. W.; Cao, X. Y.; Zhang, G. X.; Shi, X. Y. *Colloid Surf., A.* **2012**, *405*, 22–29.
164. Chou, S. W.; Shau, Y. H.; Wu, P. C.; Yang, Y. S.; Shieh, D. B.; Chen, C. C. *J. Am. Chem. Soc.* **2010**, *132*, 13270–13278.
165. Liu, Y. L.; Ai, K. L.; Liu, J. H.; Yuan, Q. H.; He, Y. Y.; Lu, L. H. *Angew. Chem., Int. Ed.* **2012**, *51*, 1437–1442.
166. Zhang, G.; Liu, Y. L.; Yuan, Q. H.; Zong, C. H.; Liu, J. H.; Lu, L. H. *Nanoscale* **2011**, *3*, 4365–4371.

167. Cheung, E. N. M.; Alvares, R. D. A.; Oakden, W.; Chaudhary, R.; Hill, M. L.; Pichaandi, J.; Mo, G. C. H.; Yip, C.; Macdonald, P. M.; Stanisz, G. J.; van Veggel, F. C. J. M.; Prosser, R. S. *Chem. Mater.* **2010**, *22*, 4728–4739.
168. Havron, A.; Davis, M. A.; Selter, S. E.; Paskins-Hurlburt, A. J.; Hessel, S. J. *J. Comput. Assisted Tomogr.* **1980**, *4*, 642–648.
169. Liu, Y. L.; Ai, K. L.; Liu, J. H.; Yuan, Q. H.; He, Y. Y.; Lu, L. H. *Adv. Healthcare Mater.* **2012**, *1*, 461–466.
170. Rabin, O.; Perez, J. M.; Grimm, J.; Wojtkiewicz, G.; Weissleder, R. *Nat. Mater.* **2006**, *5*, 118–122.
171. Kinsella, J. M.; Jimenez, R. E.; Karmali, P. P.; Rush, A. M.; Kotamraju, V. R.; Gianneschi, N. C.; Ruoslahti, E.; Stupack, D.; Sailor, M. J. *Angew. Chem., Int. Ed.* **2011**, *50*, 12308–12311.
172. Pan, D.; Williams, T. A.; Senpan, A.; Allen, J. S.; Scott, M. J.; Gaffney, P. J.; Wickline, S. A.; Lanza, G. M. *J. Am. Chem. Soc.* **2009**, *131*, 15522–15527.
173. Oh, M. H.; Lee, N.; Kim, H.; Park, S. P.; Piao, Y.; Lee, J.; Jun, S. W.; Moon, W. K.; Choi, S. H.; Hyeon, T. *J. Am. Chem. Soc.* **2011**, *133*, 5508–5515.
174. Bonitatibus, P. J.; Torres, A. S.; Goddard, G. D.; FitzGerald, P. F.; Kulkarni, A. M. *Chem. Commun.* **2010**, *46*, 8956–8958.
175. Choi, H. S.; Ipe, B. I.; Misra, P.; Lee, J. H.; Bawendi, M. G.; Frangioni, J. V. *Nano Lett.* **2009**, *9*, 2354–2359.
176. Schipper, M. L.; Iyer, G.; Koh, A. L.; Cheng, Z.; Ebenstein, Y.; Aharoni, A.; Keren, S.; Bentolila, L. A.; Li, J.; Rao, J.; Chen, X.; Banin, U.; Wu, A. M.; Sinclair, R.; Weiss, S.; Gambhir, S. S. *Small* **2009**, *5*, 126–134.
177. Oberdörster, G. *Int. Arch. Occup. Environ. Health* **2001**, *74*, 1–8.
178. Klaassen, C. D. *Casarett & Doull's Toxicology: The Basic Science of Poisons*; McGraw-Hill; New York: 2001.

Chapter 6

Silver Nanoparticle Films as Hydrogen Sulfide Gas Sensors with Applications in Art Conservation

Rui Chen* **and Paul M. Whitmore**

Institute for the Preservation of Cultural Heritage,
Yale University, West Campus, P.O. Box 27393,
West Haven, Connecticut 06516, United States
***E-mail: rui.chen@yale.edu**

We give a brief review of our research investigating the reaction between silver nanoparticles (Ag NPs) and hydrogen sulfide gas (H_2S), developing Ag NP films as H_2S gas sensors and examining the applications of Ag NP films in art conservation. The reaction between Ag NPs and H_2S demonstrates an initial reaction rate that follows a first-order reaction rate law and is proportional to the 1.3 power of the sulfide gas concentration. This relationship can be used to determine the H_2S gas concentration under ambient conditions. Through examination of several applications in art conservation, Ag NP films are shown to not only detect emission of H_2S from degraded materials under ambient conditions, but to also substitute for Ag foil and quantify the H_2S emission in the Oddy test, which tests materials for their safety in proximity to cultural property.

Introduction

Hydrogen sulfide (H_2S) gas is highly toxic by inhalation, and its ability to cause olfactory fatigue and overcome one's sense of smell puts workers in danger when working in gas-producing and accumulating areas such as gas wells and coal pits. In addition, H_2S poses significant risks of damage to materials, particularly those used to create cultural property in museums (*1–3*). It is known that H_2S can blacken lead pigments, tarnish silver objects, and form black sulfide compounds on copper alloy objects (*2*).

In The Science and Function of Nanomaterials: From Synthesis to Application; Harper-Leatherman, et al.;

The source of H_2S in the museum environment is local air pollution and emission from degraded materials. It has been recognized that many materials can produce volatile compounds as they deteriorate. Such emissions from storage and display materials can put artifacts at risk, and visual material stability evaluations known as Oddy tests are often done to identify the materials that can pose such a risk. Artifacts themselves can also be sources of volatile compounds. Recent studies have aimed at using those emissions as indicators of degradation or condition (*4*, *5*). Little is known about the factors that control the production and release of these volatile compounds during the aging of a material, particularly during aging under ambient conditions. In order to examine the emissions from artifacts, one needs reliable, sensitive, and specific measurements of gaseous compounds. While there are analytical technologies that will make this possible, ideally one would also like a robust, low-cost, and facile measurement method for detecting cumulative emissions of very low concentrations. Due to the chemical reaction between silver and H_2S, silver in different states such as silver ions dispersed in Nafion coatings and silver thin films has been applied for the detection of H_2S (*6–8*). Meanwhile, research on silver nanoparticles (Ag NPs) as H_2S gas sensors and their applications in art conservation has been pursued in our group.

In recent years applications of Ag NPs have been widely explored. For example, Ag NPs have been studied for use as antimicrobial agents in medical devices and antimicrobial control systems (*9*). Van Duyne's group pioneered a wide investigation on the possibility of Ag NPs to be used as optical biosensors, chemical sensors, and for surface enhanced Raman spectroscopy (*10*, *11*). In addition, Ag NPs have been studied for applications in nanosensor systems for gases. For example, Ag NPs on single walled carbon nanotubes acted as electrochemical sensors for H_2S gas (*12*). Ag NPs also were applied on conducting polymer nanotubes to detect ammonia gas (*13*) and on titania thin films to detect nitrogen dioxide (*14*). The gas-sensing mechanisms of Ag NPs are generally based on two aspects: 1) Ag NPs influence the electrical properties of nanocomposites; 2) the interaction of Ag NPs with the target analyte leads to a change in optical absorption due to the localized surface plasmon resonance (LSPR), which is a collective oscillation of the conduction electrons of nanoparticles excited by light. Therefore, if a chemical reaction associated with those conduction electrons occurs on the metal particle, changes to the LSPR should be expected.

Our research on Ag NPs as gas sensors is based on the chemical reaction between Ag and H_2S. Our previous study (*15*) demonstrated the high reactivity of Ag NPs to H_2S gas and that the gas–solid reaction of H_2S on Ag NPs causes a rapid decrease in the intensity of LSPR absorption upon exposure, due to free electrons of Ag NPs being converted to bound electrons of Ag_2S. Given the sensitivity of LSPR to free conduction electrons, it seemed possible that quantitative analysis on the reaction extent can be achieved by monitoring the change of intensity of LSPR absorption. Hence, we initially investigated the feasibility of Ag NP films as a sensitive, quantitative, visual sensor to detect H_2S gas generated in material stability evaluations (Oddy tests) (*16*). Also our most recent report (*17*) revealed the kinetic results of reaction between H_2S and Ag NPs and a relationship between

In The Science and Function of Nanomaterials: From Synthesis to Application; Harper-Leatherman, et al.;

reaction rate and gas concentration, which makes it possible to determine low concentrations of H_2S gas at ambient conditions. In this paper, we summarize our previous studies on developing H_2S gas sensors based on Ag NPs and report for the first time some applications of the sensors for measuring low concentrations of H_2S, a gas known to be produced from proteinaceous materials as they degrade.

Fabrication of Ag NP films

Suspensions of spherical Ag NPs can be prepared either in water or methanol. In both solvent systems, silver nitrate was reduced by sodium borohydride and the formed silver cluster was stabilized by polyvinylpyrrolidone. The syntheses were described in our previous reports (*15*, *16*).

A general procedure for fabrication of Ag NP films was reported previously by our group (*15*). A slight but critical modification was made when the Ag NPs were suspended in methanol (*16*). Polyethylenimine (PEI) was used as bifunctional linker to bind Ag NPs on a glass substrate. The procedure allows Ag NP films to be reproducibly assembled on various glass substrates such as glass cover slips or inner walls of glass cuvettes. When Ag NP films were applied as a sensor, generally the films were prepared on glass cover slips. In the kinetic study on the reaction between Ag NPs and H_2S, the Ag NPs were fabricated on the inner surfaces of the cuvettes so that the cuvettes served as both reaction vessels and film substrates. The structural features of Ag NP films prepared in this procedure, characterized in detail (*15*, *16*), shows that PEI formed evenly distributed, discontinuous isolated domains with a size of about 10 nm and then Ag NPs were randomly anchored on those PEI domains and a uniform monolayer was formed over macroscopic areas. Their AFM surface topography images (Figure 1) demonstrate the uniform distribution of PEI domains and Ag NPs (mean diameter of 7.4 nm), and the increase in the Z-range of Ag NP assembly image indicated that the particles were anchored on the top of PEI layer (*15*).

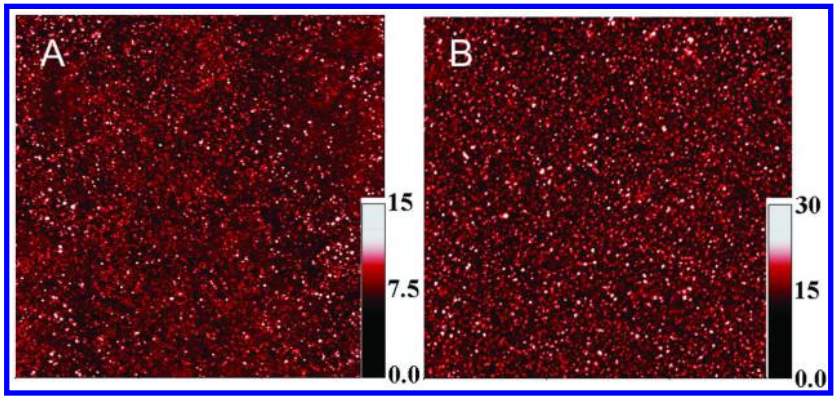

Figure 1. AFM images (size: 3 μm × 3 μm) of (A) a PEI-treated glass coverslip and (B) Ag NP assembled film on the glass. (Reproduced by permission of IOP Publishing from reference (15). 2008 © IOP Publishing. All right reserved.)

In The Science and Function of Nanomaterials: From Synthesis to Application; Harper-Leatherman, et al.;

Highlights of Reaction of Ag NP Films with H_2S Gas at Various Gas Concentrations

The reaction between Ag NP films and H_2S gas was investigated in detail (*15*, *17*). Ag NP films were assembled on the inner surfaces of optical glass cuvettes and masked by a black card with a 2 mm tall opening slit. The slit allowed the reactions occurring only at the top of the films (≤ 2 mm) to be recorded, thus minimizing the effects of inhomogeneous exposure on the measured kinetics. All the Ag NP films were yellow and displayed a single LSPR absorption with a peak wavelength between 405 – 410 nm. Given the sensitivity of the LSPR to the population of free electrons on Ag NPs and in order to assess the response of Ag NP films to H_2S, the change in the LSPR intensity at its peak absorption wavelength was recorded immediately upon exposure. In addition, to eliminate the effects from moisture and oxygen on the reaction between Ag NPs and H_2S in our initial investigation, the H_2S gas samples at various gas concentrations such as 1% (v/v), 0.1% (v/v), 100 ppmv – 1 ppmv, 500 ppbv and 100 ppbv were prepared by diluting pure H_2S, 100 ppmv H_2S (in nitrogen) and 5ppmv H_2S (in nitrogen) with ultra-high purity nitrogen.

1. Fast Response of Ag NP Film to H_2S Gas

As expected, the reaction on Ag NPs took place rapidly upon exposure to H_2S, demonstrated by a rapid decrease in the LSPR intensity at its peak absorption wavelength. As the reaction proceeded, the LSPR intensity continuously decreased until no further change in intensity occurred, that is, leveling-off intensity was reached, which was attributed to the complete conversion to Ag_2S (*15*). As was demonstrated in our previous report, the intensity decrease at the LSPR peak wavelength is a true indication of the absorption loss and is not due to a shift in the absorption away from that wavelength (*15*). A parameter approximately representing a percentage of unreacted Ag on the particles (i.e. the reaction extent), was defined as $$A\% = \frac{A_t - A_\infty}{A_0 - A_\infty} \times 100\%$$ where A_0 is the initial absorbance at peak wavelength of LSPR of the Ag NP film recorded prior to the gas being introduced, A_t is the absorbance of the reacted film at the time t, and A_∞ is the leveling-off absorbance when the film is completely reacted. Through the range of investigated gas concentrations, it was noted that the higher the gas concentration, the faster the Ag NP films responded (Figure 2). For example, it took less than 1 min to reach 20% loss in intensity (i.e. A% = 80%) when the gas concentration was higher than 20 ppmv and about 15 min when the gas concentration was 1 ppmv.

In The Science and Function of Nanomaterials: From Synthesis to Application; Harper-Leatherman, et al.;

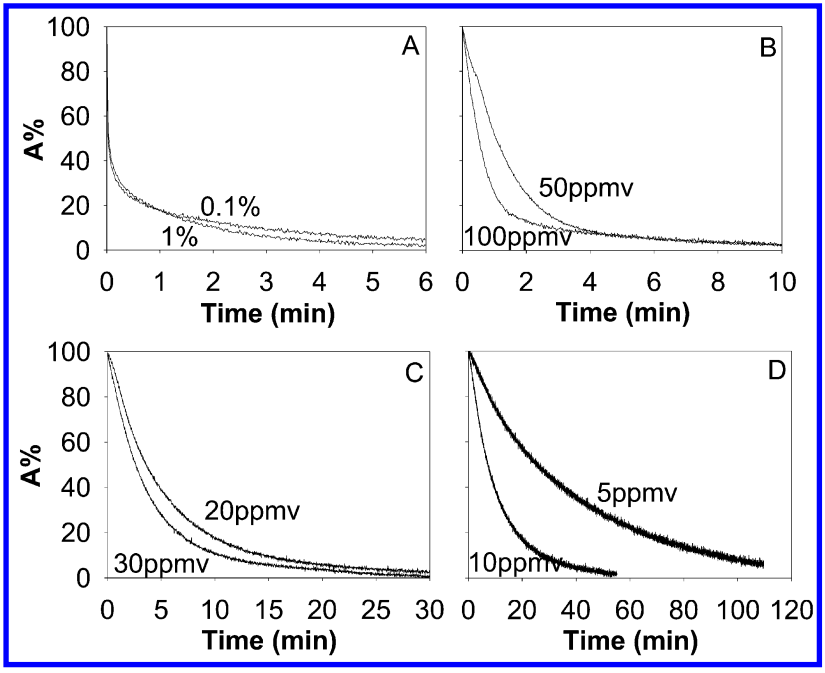

Figure 2. The decreasing LSPR intensity of the Ag NP films with reaction time at different gas concentrations. A%, the percentage of remaining LSPR intensity of the Ag NP films (related to the amount of unconverted Ag on the surface of the particles), is defined as $A\% = \frac{A_t - A_\infty}{A_0 - A_\infty} \times 100$ *, where* A_0 *is the initial absorbance of LSPR peak of Ag NPs before the film is exposed to the gas,* A_t *is the absorbance of LSPR peak at the time t,* A_∞ *is the absorbance at the peak wavelength when the reaction is complete, which is attributed to the absorption of the formed* Ag_2S*. (Reproduced with permission from reference (17). Copyright (2013) Elsevier.)*

2. Linear Relationship between the Initial Reaction Rate and H_2S Gas Concentrations

Further investigation of the kinetics of the reaction at gas concentrations in the ppmv range (Figure 3) revealed that the reaction initially followed a reaction rate law first-order in Ag and subsequently slowed down and deviated from the initial linear (first-order) relationship (*16*). The deviation of the late-stage reaction rate may be a result of Ag NP particle domains not being equally exposed to H_2S, for example by obstruction of PEI domains; also it may be attributed to diffusion of H_2S gas through surface Ag_2S to reach the unreacted interior of Ag NPs. For H_2S at higher gas concentrations, such as 0.1% (v/v), 1% (v/v) and 100%, the initial first-order reaction rate ended within the first second and the reaction proceeded at the deviated reaction rate soon after it started.

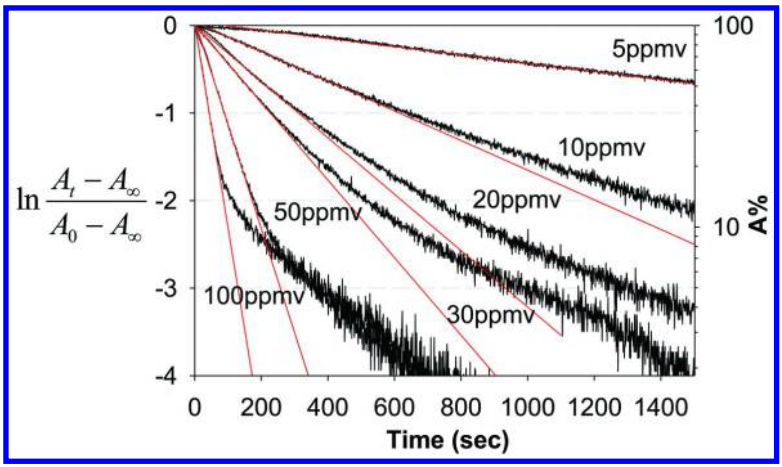

Figure 3. The semi-logarithm of the LSPR intensity ratio of the reacting Ag NP films versus time when exposed to H_2S at varied gas concentrations. The straight lines represent a linear relationship of the data when the reaction follows the first-order reaction law. The values plotted on the right y axis represent the percentage of remaining LSPR intensity. (Reproduced with permission from reference (17). Copyright (2013) Elsevier.)

From the integrated equation of the first-order reaction rate in the initial reaction, a relationship between apparent rate constant k′ and initial gas concentration $[H_2S]_0$ was elucidated (*17*) as an equation, $\frac{A_t - A_\infty}{A_0 - A_\infty} = -k't$, where $k' = k[H_2S]_0^{1.3}$. In Figure 3, the value of k′ was given by the slope of the straight line defined by the initial measurements and represented the reaction rate. Apparently, the higher the gas concentration was, the faster the reaction proceeded in the initial stage. According to the above equation and definition of k′, a linear relationship between k′ and $[H_2S]_0$ was established in a logarithm function, $\log k' = \log k + 1.3 \log[H_2S]_0$. Figure 4 exhibited this linear relationship in a common logarithm scale down to 100 ppbv. Derivation of k′ from the kinetic curve can thus be used to determine the H_2S gas concentration.

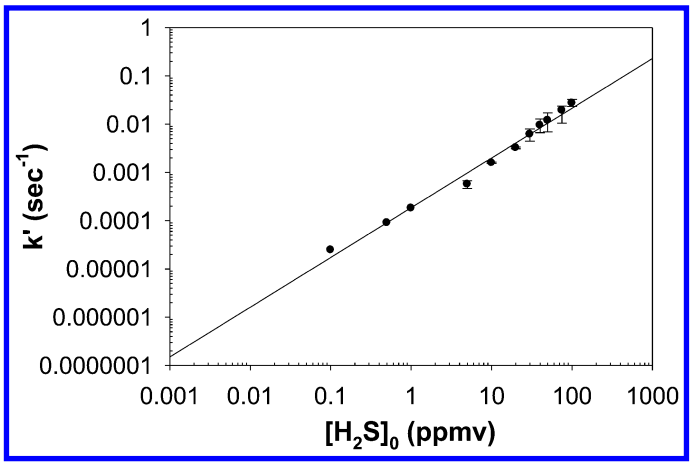

Figure 4. The linear relationship of k' to initial gas concentration $[H_2S]_0$ in a log-log plot. The slope of the linear regression is the order of $[H_2S]$ in the reaction. (Some data adapted with permission from reference (17). Copyright (2013) Elsevier.)

3. Negligible Interference of Other Volatile Compounds on the Reaction of Ag NPs with H_2S

Separate exposure tests were performed to other possible constituents in ambient environments, such as atmospheric oxygen, water vapor and volatile organic compounds, as well as other gases expected to react readily with silver, such as ammonia or hydrochloric acid (HCl) vapor (*17*). A comparison of the reaction kinetics between Ag NP films with H_2S gas in pure nitrogen and in air dilutions indicated that atmospheric oxygen had no significant impact on the reaction rate and order. In the investigations with water vapor and organic volatile compounds such as acetone and ethanol, the response of Ag NP films showed slight increases in intensity of those LSPR peaks and no change in the shape of LSPR absorptions. Such responses of LSPR spectra are believed to be due to the change in refractive index of the nanoparticle environment and the changes were less pronounced when the Ag NPs were surrounded by the vapors than immersed in the liquid of those materials. Similarly, the response of Ag NP films to gaseous ammonia initially increased the intensity of the LSPR, but it was followed by no further change over a period as long as 5 days. The reaction of Ag NP films with HCl vapor over a concentrated solution was completed after 2 days, much slower than the reaction with H_2S at 1ppmv which was completed after only 7 hours. Significant concentrations of such gases having strong basic or acidic properties are not likely to be encountered in an indoor museum environment due to limited intake of outdoor air and chemical filtration on the HVAC system. Therefore, sulfidation would be the dominant reaction if Ag NPs are exposed to low levels of H_2S and HCl. As a result of these investigations, it can be concluded that the

In The Science and Function of Nanomaterials: From Synthesis to Application; Harper-Leatherman, et al.;

slight change in the LSPR spectrum from exposure to low ambient concentrations of these compounds should not interfere with the determination of H_2S gas concentration in the environment when Ag NP films are used as a sensor.

Applications of Ag NP Films as H_2S Gas Sensor in Art Conservation

1. Monitor for Sulfide Gas Emitted through Photochemical Aging of Wool Fabrics (*18*)

Wool is a proteinaceous material composed of about 19 amino acids. Among them are sulfur-containing amino acids methionine, cysteine and cystine. During UV (wavelength < 380nm) irradiation, free radical photochemical reactions take place on the three amino acids and produce H_2S gas (*19*). For example, the disulfide bond in cystine breaks, and then with the help of atmospheric water, hydrogen sulfide is formed. Therefore the generation of H_2S depends on the amount of these three amino acids, the chain scission rate, and the ambient atmosphere. Ag NP films were applied here to examine the release of H_2S after radiation aging. The goal is to understand how much H_2S will be emitted from aged wool fabrics because this emission could pose a risk to collection objects in museums. Samples of wool fabric were exposed to UV-B fluorescent lamps (peak emission at 313 nm) for various periods. The samples with a size of 1 cm^2 were then removed and enclosed with a Ag NP film formed on the inside surface of glass cuvettes (volume of 5 cm^3) mounted in a spectrometer so the LSPR absorbance could be continuously recorded. Using the protocol described above, the change in LSPR absorption peak was measured and, through a linear regression of the initial stage of the reaction, an apparent rate constant was obtained and is proportional to concentration of H_2S gas. Thus, an average gas concentration of H_2S can be estimated from the calibration curve. Figure 5 shows a relationship between UV aging time and the emission concentration of H_2S from exposed wool fabrics (*18*). At the early stage of UV irradiation, H_2S was released from the wool and its emission increased as the irradiation proceeded. The emission rate seemed to reach a steady state before it decreased. When the irradiation time was over 500 hours, the H_2S emission stayed low but did not completely vanish. This relationship indicated that Ag NP films are able to measure the emission of H_2S from even small samples of aged wool. The H_2S concentrations generated by entire artifacts in larger display or storage volumes are currently under investigation.

In The Science and Function of Nanomaterials: From Synthesis to Application; Harper-Leatherman, et al.;

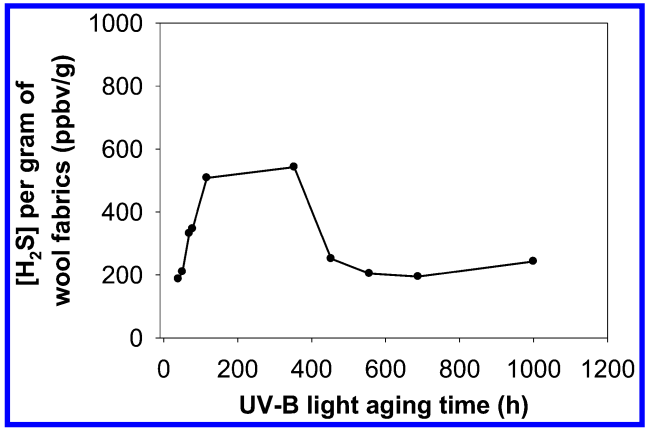

Figure 5. A plot of the emission concentration of H_2S from exposed wool fabrics versus UV aging time.

2. Examination of the Daguerreotype Case Microenvironment (*18*)

The daguerreotype was the first photographic process to come into widespread use between the early 1840s and late 1850s (*20*). In brief, the daguerreotype process can be described as the following: silver-plated copper (or brass) sheet was treated with halogen gas (iodine, bromine, chlorine) to become light-sensitized, followed by exposing the silver plate in a camera, and then developing the image with mercury vapor and washing off the remaining silver halide. The delicate image and silver surface is subject to tarnishing from exposure to air, so the plate must be kept under glass in a sealed enclosure, usually housed in small leather cases lined with silk velvet. Although such daguerreotype packages are effective in protecting the plate from atomospheric contaminants, corrosion caused by chemical reactions of the silver metal with its environment leads to continuing degradation of the image. M. S. Barger and W. B. White (*20*) listed and discussed possible mechanisms and also pointed out that the atomosphere inside the case and the cover glass were more reactive than early daguerreotypists would have ever suspected. Like wool, silk is also a proteinaceous material that has sulfur-containing amino acids (methionine and cystine) in its composition (*19*). It can be expected that H_2S gas might be generated when silk degrades.

Four daguerreotypes from the personal collection of one of the authors (Figure 6) were selected for study, representing various states of preservation: 1 was in excellent condition with little tarnishing and a distinct background and image; 2 showed the evidence of damage from corrosion along the edges but tarnishing on its background was not evident; 3 and 4 showed obvious tarnished backgrounds, especially in 4 where the background had been blackened deeply so that it is hard to find the boundary between the image and the background. Ag NP films were place into the four daguerreotype cases for over six months and the data recorded from the first three weeks were used to calculate initial reaction rates and to determine the gas concentrations. The concentrations of H_2S gas detected by Ag NP films are listed in Table I (*18*). The gas concentration in case 1 was not evident because

In The Science and Function of Nanomaterials: From Synthesis to Application; Harper-Leatherman, et al.;

the absorption of the Ag NP film did not show significant change in intensity. The estimation indicates that cases 2, 3, and 4 emitted H_2S in varied concentration. The measured concentration of H_2S emitted into the interior microenvironment seems correlated to the condition of the daguerreotypes images: the higher the sulfur gas level the more deteriorated the image. The condition of the image is thought to be predominantly a measure of the integrity of the seals around the edges of the glass covers. However it is interesting to consider whether those seals might become compromised more easily from prolonged exposure to high levels of the gases emitted by the degrading lining fabrics.

Figure 6. Four daguerreotypes within their cases that were examined for the H_2S concentrations in the interior microenvironment with Ag NP films.

Table I. Concentrations of H_2S gas detected by Ag NP films in each daguerreotype case

Daguerreotype cases	*[H_2S] (ppbv)*
1	not evident
2	33.0
3	80.7
4	151.1

3. Substitution of Ag Foil in Material Stability Evaluation – Oddy Test

The Oddy test is a widely applied practical method in museums to evaluate stability of display, storage, and shipping materials, which may emit gases that can damage materials, particularly metals, used in works of art. In a general procedure, a material is incubated in a sealed vial with enough water to produce 100% humidity and three metal coupons (copper, silver and lead) are used for detecting the emission of harmful compounds. After 28 days of heating at 60°C, the metal coupons are visually examined for evidence of corrosion due to off-gassing from the test material. An Oddy test of wool fabric shows the Ag foil starting to show a pinkish hue indicating visible tarnish by sulfide gas at day 3. Further reaction changed the pinkish hue gradually to blue at days 4 and 5, but additional exposure did not significantly change the coupon's tarnished appearance (*16*). Obviously, the Oddy test is time-consuming, and the extent of corrosion on the metal coupons is difficult to evaluate as well as not being easily quantifiable. Besides our attempt to improve the Oddy test, other improvements have been reported such as applying silver and copper nanofilms in the Oddy test system as substitutes and rating the corrosion extent by digital image processing (*21*, *22*).

Given the fast response of Ag NP films to sulfide gas and easy quantitative monitoring of the reaction extent, Ag NP films were examined as substitutes for the Ag coupon in the Oddy test. With no test sample in the system, Oddy test conditions seemed to alter the spectral profile in a way that suggested better Ag NP dispersion over the film (particle stacking may have originally occurred): disappearance of the shoulder peak and increase in the LSPR intensity. The intensity increased in the first week of the humid thermal treatment and remained relatively constant for over a month. Figure 7 showed that the Ag NP films had good stability under the Oddy test conditions and can be used to detect sulfide gas in the Oddy tests.

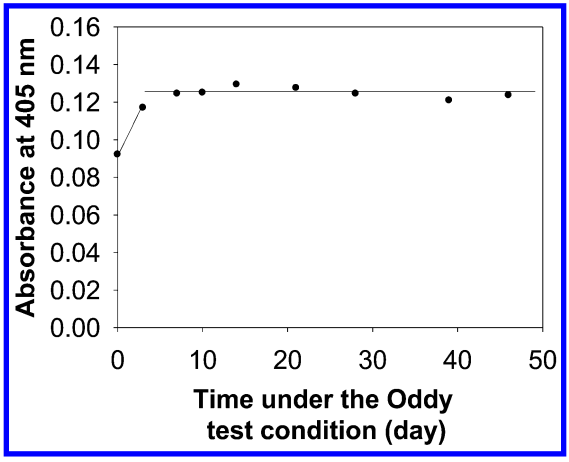

Figure 7. Stability study on Ag NP film under the Oddy test conditions: a plot of absorbance of the LSPR peak at 405 nm versus the time periods. (Reproduced with permission of Cambridge University Press from reference (16). Copyright © 2008 Material Research Society.)

In The Science and Function of Nanomaterials: From Synthesis to Application; Harper-Leatherman, et al.;

Ag NP films were substituted for Ag foil in the Oddy test of a piece of wool fabric. The reaction of Ag NP film with H_2S emitted from the wool was monitored by measuring a change in intensity of the LSPR absorption (Figure 8a). Unlike the difficult determination of the extent of corrosion on Ag foil, the reaction extent on Ag NP films was quantified from spectra measurements and shown in Figure 8b. By adjusting the Ag NP density on the film, the reaction on Ag NP films with emitted H_2S can be complete by day 3 of the Oddy test of the wool sample, with the film becoming virtually colorless. In comparison, at this early stage of the test the Ag foil was just beginning to show perceptible tarnishing. It is evident that the Ag NP films are both quantitative and sensitive as an optical sensor for sulfide gas, and they should be considered viable alternatives for Ag foil in the Oddy tests.

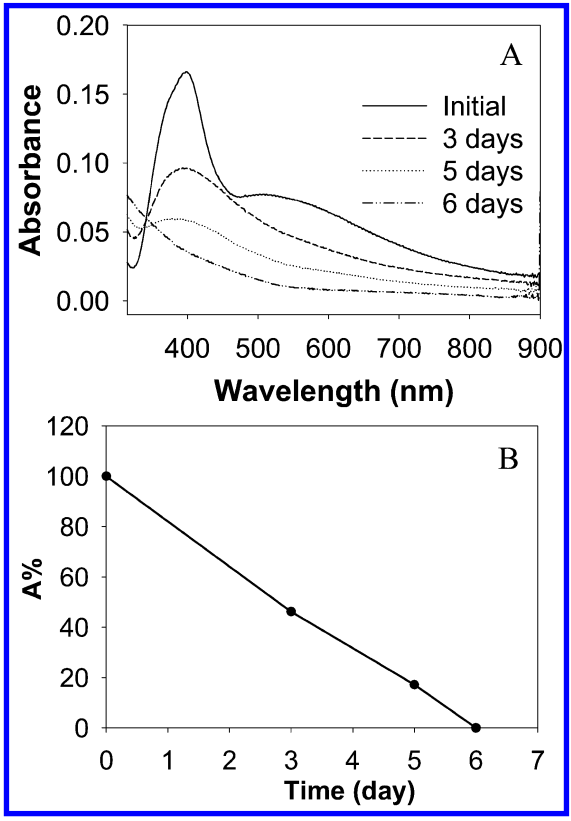

Figure 8. (A) UV-vis spectra of Ag NP film during the exposure to sulfide gas in the Oddy test of a wool fabric sample. (B) Reaction extent on Ag NP film calculated for the above exposure. (Reproduced with permission of Cambridge University Press from reference (16). Copyright © 2008 Material Research Society.)

In The Science and Function of Nanomaterials: From Synthesis to Application; Harper-Leatherman, et al.;

Conclusion

Ag NP films were developed as optical sensors for H_2S gas based on the reaction between Ag and H_2S, which is easily tracked by the intensity change in LSPR absorption. Kinetics studies on the reaction between Ag NPs and H_2S revealed the initial reaction rate followed the first reaction rate law and is proportional to the gas concentration on a logarithm scale. This relationship allows the determination of the H_2S concentration from measurement of the initial reaction rate on Ag NP films. The gas concentrations have been calculated when Ag NP films were exposed to UV-degraded wool fabrics and naturally aged silk of daguerrotypes. The H_2S emission from the aged materials can be used to assess a risk of damage to nearby metal objects. Ag NP films also showed advantages as sensitive, quantitative substitutes for Ag foil in the Oddy test. Therefore, this designed Ag NP sensor can be a useful means to study sulfur gas emission and the risk of sulfide gas damage to collection objects in the field of art conservation.

Acknowledgments

This research work was supported by a grant from the Andrew W. Mellon Foundation.

References

1. Ankersmit, H. A.; Tennent, N. H.; Watts, S. F. *Atmos. Environ.* **2005**, *39*, 695–707.
2. Bradley, S. *J. Am. Inst. Conserv.* **2005**, *44*, 159–173.
3. Ryhl-Svendsen, M. *J. Cult. Herit.* **2008**, *9*, 285–293.
4. Ramalho1, O.; Dupont, A.-L.; Egasse, C.; Lattuati-Derieux, A. *e-Preserv. Sci.* **2009**, *6*, 53–59.
5. Gibson, L. T.; Ewlad-Ahmed, A.; Knight, B.; Horie, V.; Mitchell, G.; Robertson, C. J. *Chem. Cent. J.* **2012**, *6* (1−22), 42.
6. Jarosz, A. P.; Yep, T.; Mutus, B. *Anal. Chem.* **2013**, *85*, 3638–3643.
7. Hawkins, S. J.; Ratcliffe, N. M.; Sagastizabal, A. *Anal. Chim. Acta* **1998**, *359*, 125–132.
8. Weyde, E. *Photogr. Sci. Eng.* **1972**, *16*, 283–286.
9. Kim, J. S.; Kuk, E.; Yu, K. N.; Kim, J. H.; Park, S. J.; Lee, H. J.; Kim, S. H.; Park, Y. K.; Hwang, C. Y.; Kim, Y. K.; Lee, Y. S.; Jeong, D. H.; Cho, M. H. *Nanomedicine* **2007**, *3*, 95–101.
10. Jensen, T. R.; Malinsky, M. D.; Haynes, C. L.; Van Duyne, R. P. *J. Phys. Chem. B* **2000**, *104*, 10549–10556.
11. Haynes, C. L.; Van Duyne, R. P. *J. Phys. Chem. B* **2001**, *105*, 5599–5611.
12. Fam, D. W. H.; Tok, A. I. Y.; Palaniappan, A.; Nopphawan, P.; Lohani, A.; Mhaisalkar, S. G. *Sens. Actuators, B* **2009**, *138*, 189–192.
13. Yang, X.; Li, L.; Yan, F. *Sens. Actuators, B* **2010**, *145*, 495–500.
14. Serra, A.; Re, M.; Palmisano, M.; Vittori Antisari, M.; Filippo, E.; Buccolieri, A.; Manno, D. *Sens. Actuators, B* **2010**, *145*, 794–799.

15. Chen, R.; Nuhfer, N. T.; Moussa, L.; Morris, H. R.; Whitmore, P. M. *Nanotechnology* **2008**, *19* (1−11), 455604.
16. Chen, R.; Nuhfer, N. T.; Moussa, L.; Morris, H. R.; Whitmore, P. M. In *Materials Issues in Art and Archaeology VIII*; Vandiver, P. B., McCarthy, B., Tykot, R. H., Sil, J. L. R., Casadio, F., Eds.; Volume 1047, Materials Research Society Symposia Proceedings; Cambridge University Press: Cambridge, U.K., 2008; pp 1047-Y04-04.
17. Chen, R.; Morris, H. R.; Whitmore, P. M. *Sens. Actuators, B* **2013**, *186*, 431–438.
18. Research presented in this section has not been published previously. The results were included in presentations given at the 39th Annual Meeting of American Institute for Conservation (AIC), Philadephia, 2011, and the ACS Northeast Regional Meeting, New Haven, 2013.
19. Tímár-balázsy, Á.; Eastop, D. *Chemical Principles of Textile Conservation*; Butterworth-Heinemann: Oxford, U.K., 1998; pp 43−55.
20. Barger, M. S.; White, W. B. *The Daguerreotype: Nineteenth-Century Technology and Modern Science*; The Johns Hopkins University Press: Baltimore, MD, 2000; pp 2, 160−182.
21. Wang, S.; Kong, L.; An, Z.; Chen, J.; Wu, L.; Zhou, X. *Stud. Conserv.* **2011**, *56*, 138–153.
22. Hodgkins, R. E.; Centeno, S. A.; Bamberger, J. A.; Tsukada, M.; Schrott, A. *e-Preserv. Sci.* **2013**, *10*, 71–76.

Chapter 7

Development of Calcium Carbonate Double-Coated with Chitosan-Adipic Acid as a Promising Antibacterial Filler

Yecheng He, Baofeng Lin,* and Haizhong Zou

College of Chemistry and Chemical Engineering, Guangxi University, Nanning, 530004, Guangxi, China
***E-mail: linbf941@gxu.edu.cn**

The aim of the present work was to investigate a new use of chitosan in the modification of calcium carbonate ($CaCO_3$) particles in order to confer specific antibacterial functionality to the particles. Adipic acid was used to introduce carboxyl groups onto the surface of $CaCO_3$ particles. $CaCO_3$ particles double-coated with chitosan-adipic acid (abbreviated as CAC) were prepared through the ionic interaction between the 2 site amino group of chitosan and the carboxyl group of adipic acid. The structure of CAC was characterized by Fourier transform infrared spectroscopy (FTIR), thermogravimetric analysis (TGA) and scanning electron microscopy (SEM). The zeta potential and contact angle of CAC were studied to evaluate particle interfacial properties. FTIR and TGA analyses showed that chitosan and adipic acid on CAC were combined through electrostatic interactions. When the chitosan concentration was more than 5%, the surface of the $CaCO_3$ particles were coated completely. When chitosan was applied at a 9% concentration to make CAC, the zeta potential increased from –27.58 mV for unmodified particles to +13.11 mV for CAC due to the increased positive charge from chitosan. In a similar way,

In The Science and Function of Nanomaterials: From Synthesis to Application; Harper-Leatherman, et al.;

the specific surface area increased from 2.846 m^2/g to 4.709 m^2/g, the average particle size decreased from 11.21 μm to 7.49 μm, and the contact angle increased from 0° to 87°. CAC had antibacterial capacity when evaluated with *E. coli* and *S. aureus*. The approach in this study provides a method for fabricating chitosan-adipic acid-modified $CaCO_3$ particles, an antibacterial filler for potential applications.

Introduction

Fillers are particles added to materials (e.g. plastics, composite materials, or concrete) to lower the consumption of more expensive binder materials or to improve some properties of the materials (*1*). Calcium carbonate ($CaCO_3$) is one of the most widely used fillers in materials as diverse as rubber, plastics, paper, paint, and pharmaceuticals. The addition of a filler was initially seen mainly as a means of reducing the compound cost, but as the relative cost of polymers decreased, attention focused on potential property improvements to materials that fillers could impart (*2*). Nano-fillers have attracted tremendous interest because of desired properties such as electronic mobility, thermal conductivity, and optical properties. Therefore, much effort has been made to take advantage of their properties in polymer matrices (*3*). Nano-fillers are doping agents distributed in the matrix of a composite, whose individual elements have at least one dimension in the nanoscale (*4*). Nano-filler dispersion has been a challenge in polymer nanocomposite fabrication. The active surface and large surface area of nano-fillers make them very likely to aggregate inside a matrix (*3*). As one of the most important nano-fillers, $CaCO_3$ nanoparticles have been widely studied and utilized in academic and industry applications because of superior mechanical properties, high thermal stability, commercial availability and substantial improvement in polymer properties that they impart as fillers (*2*). However, recent research found that high filler loading may adversely affect processability, ductility and strength of a compound. Additionally, the fabrication and dispersion of $CaCO_3$ microparticles and nanoparticles remains a difficult problem. This may be due to particle agglomeration and the immiscibility between inorganic particles and the polymer matrix leading to the deterioration of polymer properties. $CaCO_3$ microparticles and nanoparticles have large specific surface areas and high surface tensions making them difficult to homogenize as well. It is, therefore, of great interest to functionalize the surface of calcium carbonate particles to improve their applicability as fillers (*5–8*).

Past research has proved that surface modification may improve the dispersion of calcium carbonate particles as fillers and strengthen the interaction between filler and substrate (*2*). For instance, the behavior of coated calcium carbonate particles under heating was of great value for its industrial applications (*9*). The main types of surface modifiers that have been applied during production are fatty acids and organo-silane coupling agents (*10*). Industrial coating with fatty acids is done in water because of the low cost and simplicity of the process (*10*). However, previous studies on the surface characterization of calcium

In The Science and Function of Nanomaterials: From Synthesis to Application; Harper-Leatherman, et al.;

carbonate particles coated with stearic acid involved synthetic conditions such as high speed mixing for dry-coating or dissolving stearic acid in toluene for wet-coating (*10*). During coating with solutions of a stearin salt in water, no matter what the concentration used, a considerable part of the surface of calcium carbonate was incompletely coated with stearin (*10*). Silane coupling agents are chemical substances capable of reacting with both the reinforcement and the resin matrix of a composite material and may also bond inorganic fillers or fibers to organic resins, promoting strong interface bonding. Coupling agents can play an important role in improving the compatibility and adhesion between polar material and non-polar polymeric matrices (*11*). However, some coupling agents may lead to environmental pollution. To overcome some of stearic acid's drawbacks, as described above, adipic acid, an important and cheap precursor for the production of nylon-6,6 (*12*), has been used to modify calcium carbonate particles, leaving an active functional group on the surface of particles.

Chitosan, a hydrophilic biopolymer industrially obtained by N-deacetylation of chitin, displays unique polycationic, chelating, film-forming properties due to the presence of active amino and hydroxyl functional groups (*13*) and can be applied as an antimicrobial agent against fungi, bacteria, and viruses (*14*). Chitosan exhibits higher antibacterial activity against Gram-positive bacteria than Gram-negative bacteria does. The antibacterial activity of chitosan has been shown to be affected by many factors. For instance, the molecular weight, solvent, and pH values all were found to affect antibacterial properties (*15*). Nicu et al. evaluated alkyl-chitosan derivatives with $CaCO_3$ (polymer:$CaCO_3$ ratio of 30:70) as paper coating materials in developing water barrier properties (*16*).

The purpose of our current study is to demonstrate that the surface of calcium carbonate ($CaCO_3$) particles can be double-coated with adipic acid and chitosan to make the particle surfaces simultaneously organophilic and antibacterial. Adipic acid was employed to bridge $CaCO_3$ and chitosan to lower the synthetic cost. In general, double coating has the potential to lead to improved particle mechanical properties and has been shown to lead to better performance of particles in such applications as corrosion prevention and drug delivery (*17*). For instance, double-layer coating on magnesium alloy has been shown to be a promising way to prevent the corrosion of magnesium in harsh service environments (*18*). A double-layered coating on silicon nitride provides lower optical reflection and better surface passivation compared to single-layered silicon nitride (*19*). Multilayers of sodium poly(styrene sulfonate) and aliphatic poly(urethane-amine) coated on $CaCO_3$ nanoparticles have potential as smart drug delivery vehicles (*20*). Double-layer coating also has its challenges due to possible unwanted interactions between the two coating compounds compared to single-layer coating. However, we demonstrate in this report that $CaCO_3$ microparticles have been successfully double-coated with chitosan-adipic acid.

CAC were characterized by Fourier transform infrared spectroscopy (FTIR), thermogravimetric analysis (TGA) and scanning electron microscopy (SEM). The zeta potential, specific surface area, particle size and contact angle were also studied to evaluate the interfacial properties of CAC. Antibacterial activity was studied, and the results show that CAC has promise as a useful antibacterial filler.

Experimental Section

Materials

Calcium carbonate with a particle size of 11 μm was purchased from Guangxi Wuming Xianfeng Co. Ltd (Nanning, China). Chitosan was supplied by Beihai Halobios Co. Ltd., (Beihai, China), with a deacetylation degree of 76% and molecular weight of 1.24×10^5 Daltons.

Preparation of CAC

$CaCO_3$ particles were coated by adipic acid and chitosan through layer by layer self-assembly. 10 g of $CaCO_3$ particles were added to 100 mL of water in a 250 mL three-necked flask while vigorously stirring. 10 mL of 0.5% adipic acid aqueous solution was then added dropwise into the $CaCO_3$ dispersion while stirring at 70 °C to form the adipic acid layer. After 1 hour, the particles were filtered off, washed three times with distilled water and dried in air. The single coated $CaCO_3$ (adipic acid-coated) particles were dispersed in 100 mL of water to form the initial suspension. 1 g of chitosan was dissolved in 100 mL of 2% adipic acid aqueous solution. The chitosan layer was coated onto the particles by adding the initial suspension into the chitosan solution while stirring for 1 hour at 70 °C. The particles were rinsed with distilled water and dried. Calcium carbonate particles double-coated with chitosan (1, 3, 5, 7 or 9 wt %) and adipic acid (0.5, 1.5, 2.5, 3.5 or 4.5 wt %) were coded as CAC1, CAC2, CAC3, CAC4 and CAC5.

Infrared Spectroscopy

The Fourier transform IR (FTIR) spectra of samples were recorded with a Shimadzu IR spectrophotometer (model 8300) in the range of 500 and 4000 cm^{-1} as a KBr pellet with 4 cm^{-1} resolution, acquiring 50 scans for each spectrum.

Thermogravimetric Analysis

Thermogravimetric analysis (TGA) was performed using a Q5000IR analyzer. The samples of 5 mg were examined in nitrogen atmosphere from 25 to 600 °C at a heating rate of 20 °C/min.

Scanning Electron Microscopy

The morphology of the fractured surfaces of the specimens was examined with a scanning electron microscope (SEM; ev018, Zeiss, Germany). A layer of gold was sputter-coated uniformly over all surfaces before SEM observations. The SEM micrographs were collected at an acceleration voltage of 20 kV.

Zeta Potential

The zeta potential was determined by JS94G+ microelectrophoresis apparatus (Shanghai Zhongchen Digital Technique Equipment Ltd Co, Shanghai, China).

In The Science and Function of Nanomaterials: From Synthesis to Application; Harper-Leatherman, et al.;

Samples were diluted to 0.1 wt % suspension with de-ionized distilled water and subjected to treatment in an ultrasonic bath for 10 minutes. Sonication was carried out in a KQ100DB ultrasonic bath of Kunshan Ultrasonic Instruments Co., Ltd. under 40 kHz and 10 W for 2 min.

Average Particle Size and Specific Surface Area

The average particle size was determined by centrifugal photo-sedimentation using Stokes Law at 20 °C by the Sedimentation-Photometry method (*21*) (SHIMADZU Sa-cp3 Particle Size Analyzer) of aqueous solutions made by dissolving 0.1% particle in ion-exchanged water. This method is based on the measurement of the settling rate for particles under gravitational or centrifugal acceleration in a quiescent liquid. The specific surface area of the particles was measured by the Brunauer–Emmett–Teller method of N_2 adsorption–desorption at −196°C with an Jwbk112 surface area analyzer.

Static Contact Angle

Static water contact angle measurements were tested using JY-82 contact angle analyzer at room temperature (relative humidity 57% at 25°C) by the static sessile drop method (*22*). Before testing, the sample was dried at 60°C for 5 hours, then pressed into a tablet with a diameter of 1 cm with 30 MPa of force. A drop of distilled water was placed on the surface of the sample and the contact angle was measured.

Organification Degree

The amount of chitosan-adipic acid coated on $CaCO_3$ was obtained by measuring the weight loss of CAC after pyrolysis (*23*). Organification degree (OD) indicated the approximate weight percent of adipic acid and chitosan in the CAC (*24*). CAC with different organification degrees and naked $CaCO_3$ were accurately weighed and placed inside the furnace heated to 600 °C until those samples were calcined to constant weight (about 5 hours). The experiment was repeated three times for each sample. Organification degree of CAC was calculated according to the following equation:

$$OD = \frac{m_1 - m_2}{m_1} \times 100\% - (1 - \alpha)$$

Where m_1 and m_2 are the weight of the samples before and after calcining, and α is the mass-loss rate of naked $CaCO_3$ under the same conditions.

Stability of Coating Layer

CAC particles were diluted to 5 wt % suspensions with de-ionized distilled water. The suspensions were mechanically stirred (about 120 rpm) or sonicated (40 kHz and 100 W) for 10, 20, 30, 40, or 50 minutes and then filtered. The residues

In The Science and Function of Nanomaterials: From Synthesis to Application; Harper-Leatherman, et al.;

of CAC were washed by distilled water, placed in an air-circulating oven until dry and filtered through a 200-mesh size sieve to remove dust and small particles. The organification degree of sieved CAC was then measured. CAC5 samples were ground for 10, 20 and 30 minutes and then characterized by SEM.

Antibacterial Assay

Antibacterial activity of CAC against *E. coli* and *S. aureus* was evaluated by using the optical density (O.D.) method as follows. Minimum inhibitory concentration (MIC) for chitosan against several *E. coli* and *S. aureus* are 20, 100, 498, 1000 and 20, 100, 700 or more than 800 ppm, respectively (*25*). Samples (0.1 wt %) were separated in peptone saline (0.1 wt % peptone, 0.05 wt % NaCl, 0.03 wt % beef extract powder) and respectively diluted to 100 mL. The pH was adjusted to pH 6.5 with 1 M NaOH. The suspensions were autoclaved at 121 °C for 15 min (about 205 kPa). 1 mL of bacterial suspension was added to each CAC suspension. The suspensions were shaken in a thermostatic shaker for 24 hours at 37 °C. The solutions were measured for their absorption at 610 nm using a UV–Visible spectrophotometer (UV-6100, MAPADA, Shanghai). The experiment was repeated three times for each sample. The number of cfu was determined by counting microscopically with a hemocytometer, a device used to count cells (XB.K.25.,Shanghai Qiujing Biochemical Reagents Co., Ltd.).

Results and Discussion

FT-IR Analysis

FT-IR spectroscopy was used to characterize the organic groups and the chemical bonds of the particles. Figure 1 shows FT-IR spectra of chitosan (a), adipic acid (b), naked $CaCO_3$ (c), adipic acid-coated $CaCO_3$ (d), and CAC (e). In the case of chitosan (a), a broad band observed at 3452 cm^{-1} can be assigned to the stretching vibrations of O–H and N–H (*26*), while the band at 1652 cm^{-1} represents the presence of the carbonyl of the amide group stretching vibrations (*27*). In the spectrum of $CaCO_3$(c), the peaks appearing at 1431 and 874 cm^{-1} were attributed to asymmetric C–O stretching and out-of-plane deformation of CO_3 (*28*). In the case of adipic acid-coated $CaCO_3$ (d), all of the characteristic bands of $CaCO_3$ were observed in addition to new sharp peaks at 2920 and 2850 cm^{-1}. These peaks were assigned to C–H stretching vibration of $–CH_2$ groups and indicated that adipic acid reacted with $CaCO_3$. In the case of CAC(e), compared with the spectrum of chitosan and adipic acid-coated $CaCO_3$, the peak shifted from 1652 $cm^{-1}$to 1638 cm^{--1} and an extra carboxylate anion band appeared at 1560 cm^{-1}, indicating electrostatic interactions between adipic acid and chitosan (*27*). It is reasonable to conclude that chitosan was crosslinked with adipic acid by ionic interactions (*29*, *30*) and successfully coated on adipic acid modified $CaCO_3$.

In The Science and Function of Nanomaterials: From Synthesis to Application; Harper-Leatherman, et al.;

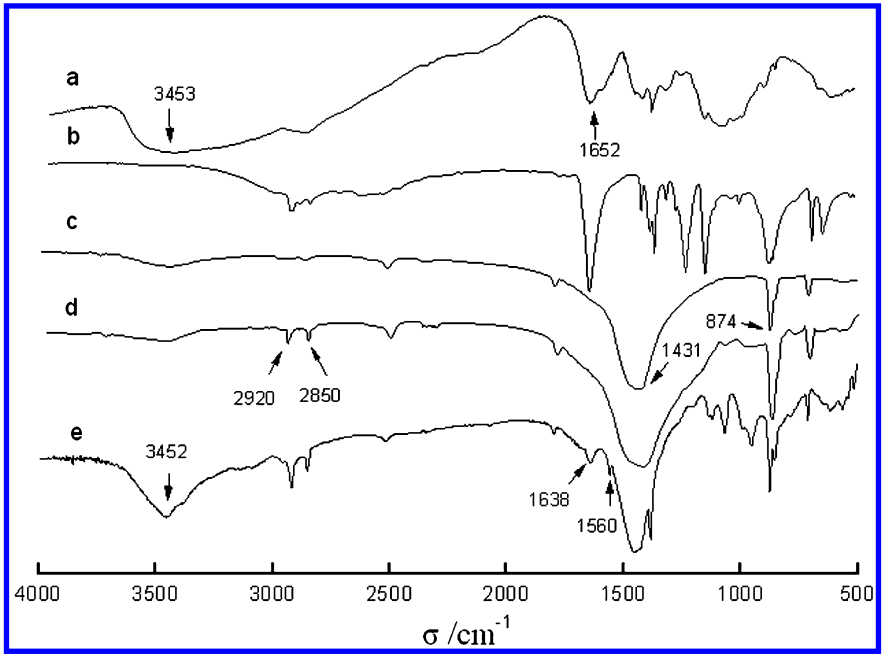

Figure 1. FTIR spectra of chitosan (a), adipic acid (b), $CaCO_3$ (c), adipic acid coated $CaCO_3$ (d) and CAC (e).

Thermogravimetric Analysis

The thermal stability of CAC was studied by TGA analysis. Figure 2 shows the mass changing rate curve characteristics of $CaCO_3$ (a), chitosan (b) adipic acid (c) and CAC (d). The weight loss of $CaCO_3$ was about 2% between 500 °C and 600 °C (Figure 2a) and the decomposition of calcium carbonate began at about 600 °C (*31*). It was observed that chitosan's degradation started at about 250 °C, whereas in CAC, light weight loss was observed between 280 and 330 °C which was associated with the degradation of the chitosan layer and evaporation of adipic acid (*32*). Adipic acid had completely evaporated at about 266 °C (Figure 2c) (*32*). As can be seen, a shift of the degradation temperature of chitosan towards higher temperature was clearly evidenced on CAC, compared with pure chitosan. The morphology and cross-linked organization of chitosan chains on CAC are different than pure chitosan, leading to enhanced thermal stability of chitosan as evident from the increased thermal degradation temperature (*33*). These results also proved that chitosan was coated via ionic bonds. The chitosan-adipic acid content of CAC5 particles was estimated to be about 9% based on the thermograms.

In The Science and Function of Nanomaterials: From Synthesis to Application; Harper-Leatherman, et al.;

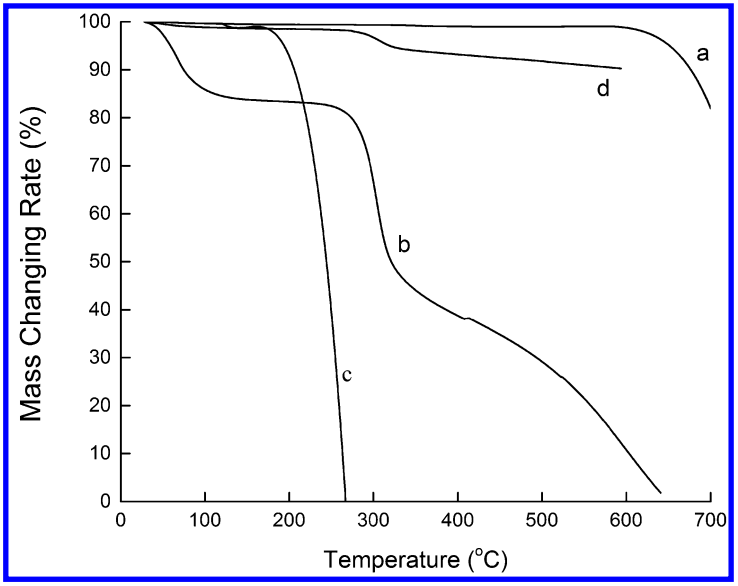

Figure 2. Thermogravimetric curves of $CaCO_3$ (a), chitosan (b), adipic acid (c) and CAC (d).

Morphology

Information about shape and size of the particles was provided by SEM. Figure 3 shows the SEM micrographs of naked $CaCO_3$ (a), chitosan (b), CAC1 (c), CAC2 (d), CAC3 (e), CAC4 (f) and CAC5 (g). Uncoated $CaCO_3$ can be characterized by the presence of a rough surface with many sharp edges and corners. After the coating, the surface morphologies totally changed. Coated particles appeared to have a more rugged and porous surface. The surface morphologies also varied as the concentration of chitosan was varied. The chitosan layer covered most of the surface of the $CaCO_3$ in Figure 3e.

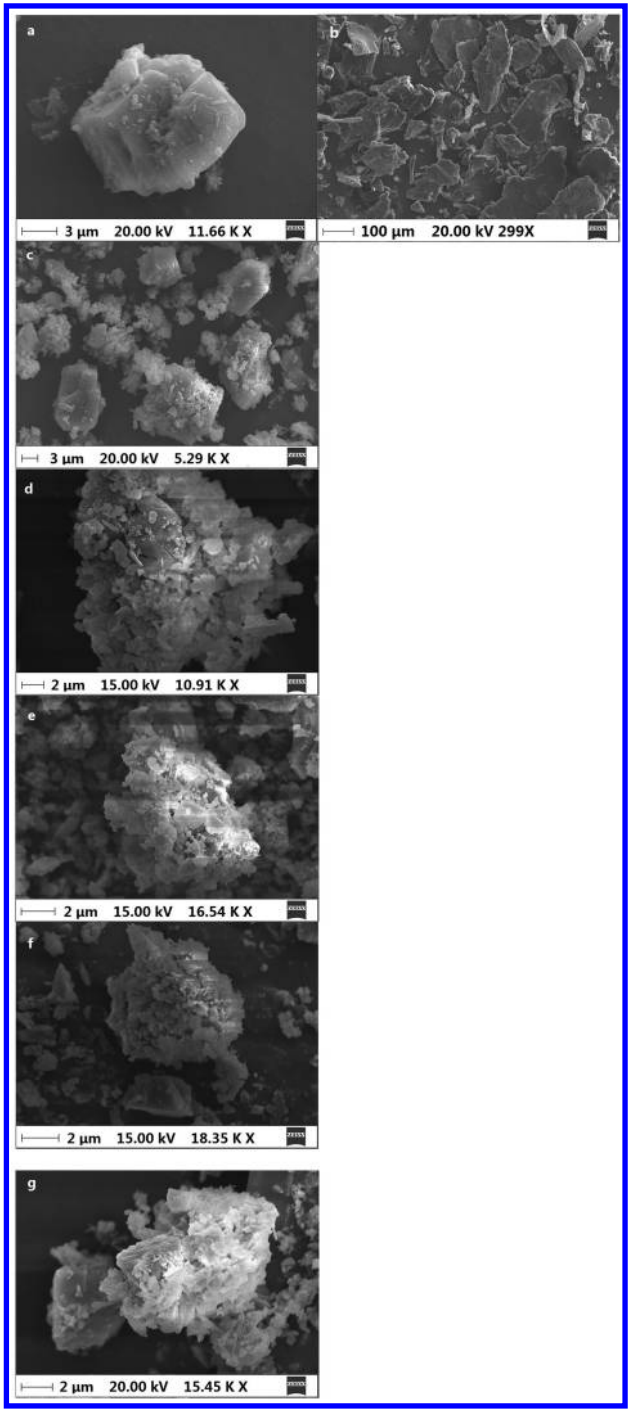

Figure 3. SEM pictures of $CaCO_3$ (a), chitosan (b), CAC1 (c), CAC2 (d), CAC3(e), CAC4 (f) and CAC5 (g).

Zeta Potential

Zeta potential (ζ-potential), which is related to surface charge of the particle, can greatly affect particle stability in suspension (*13*). To further verify the chitosan coating on the $CaCO_3$ samples, the ζ-potential of various samples in aqueous solutions was measured. Table 1 summarizes the ζ-potential of $CaCO_3$ and coated $CaCO_3$ prepared with different weight percentages of chitosan. The ζ-potential of $CaCO_3$ aqueous emulsion was –27.58 mV. After coating, the ζ-potential of particles increased from an initial value of –25.02 mV to +13.11 mV indicating that chitosan appears to play an important role in the change in ζ-potential of $CaCO_3$ particles in aqueous suspension. Chitosan carries positive charge whereas $CaCO_3$ particles are negatively charged. The change in ζ-potential from a negative to a positive value suggests that chitosan is located at the outermost layer of the particles (*34*).

Table 1. Effects of chitosan concentration on ζ-potential of CAC

Samples	*$CaCO_3$*	*CAC1*	*CAC2*	*CAC3*	*CAC4*	*CAC5*
ζ-Potential (mV)	–27.58	–25.02	–20.69	–18.81	–6.34	+13.11

Average Particle Size and Specific Surface Area

The influence of chitosan on average particle size and specific surface area of particles was also investigated. The results are presented in Figure 4. Average particle size depended on the concentration of chitosan used for coating. The particle size (diameter) of coated $CaCO_3$ ranged from 10.84 μm to 7.49 μm, which was lower than that of naked $CaCO_3$ which had an average diameter of 11.21 μm. Increasing the concentration of chitosan from 1% to 9% resulted in a decrease in particle size. On the other hand, the specific surface area of the particles was higher after coating. The specific surface area of $CaCO_3$ was 2.846 m^2/g. The specific surface area of coated $CaCO_3$ increased from 3.289 m^2/g to 4.709 m^2/g on increasing the amount of chitosan from 1% to 9%. The smaller particle size and higher particle specific surface area can be attributed to the interaction between $CaCO_3$, adipic acid and chitosan. Before coating, the average diameter of $CaCO_3$ particles was around 11 μm possibly due to partial aggregation of particles. Double-coating the particles breaks up any aggregates into smaller particles with higher surface areas. There is greater separation between particles with improved dispersibility of CAC in water.

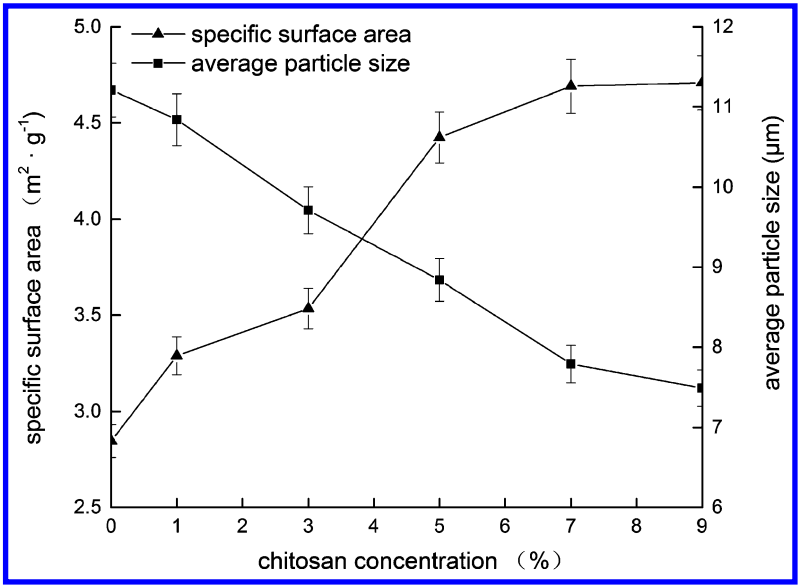

Figure 4. Effects of chitosan concentration on specific surface area of CAC and average particle size.

Contact Angle

Table 2 shows the static contact angle of $CaCO_3$, chitosan, and CAC. The data indicates that the samples became more hydrophobic after the addition of chitosan. As a result, the contact angles increased from 0° to 87° which indicates that calcium carbonate was double-coated with chitosan-adipic acid successfully. Surface modification of coated $CaCO_3$ particles with hydrophobic chitosan could help to prevent particle agglomeration and improve the miscibility between the inorganic particles and the polymer matrix, so that this antibacterial filler can be used widely in pharmacy, health care, and the food industry.

Table 2. Contact angle of different samples

Samples	*$CaCO_3$*	*CAC1*	*CAC2*	*CAC3*	*CAC4*	*CAC5*	*Chitosan*
Contact angle (deg)	0	80	82	83	85	87	100

Stability of Coating Layer

The mechanical stabilities of the coatings in water were determined by the application of mechanical stirring and consecutive ultrasonic treatments (*35*). In Figure 5, the organification degree curves are smooth, implying that CAC particles coated with chitosan-adipic acid are stable. The chitosan-adipic acid layer did not decrease after strring and sonication.

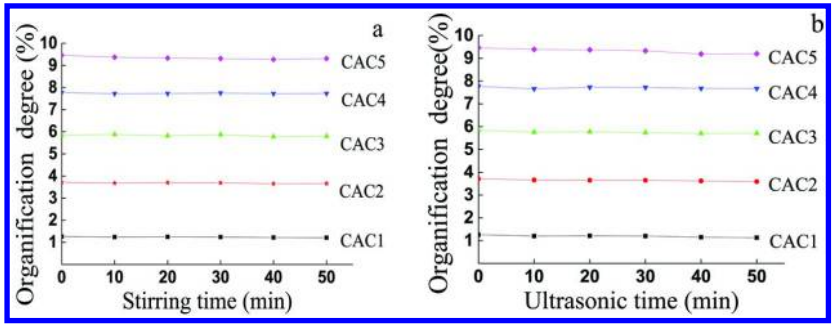

Figure 5. Effect of stirring (a) and ultrasonic time (b) on organification degree.

FTIR spectra for CAC5 after stirring and sonication are shown in Figure 6. There were no new peaks, no significant peak shifts, and no disappearance of peaks observed suggesting that the structure of CAC after mechanical disruption in aqueous solution is maintained. The results of mechanical stirring and sonication revealed that strong ionic interactions are present between chitosan-adipic acid and $CaCO_3$ and that the coating of CAC could not be destroyed easily.

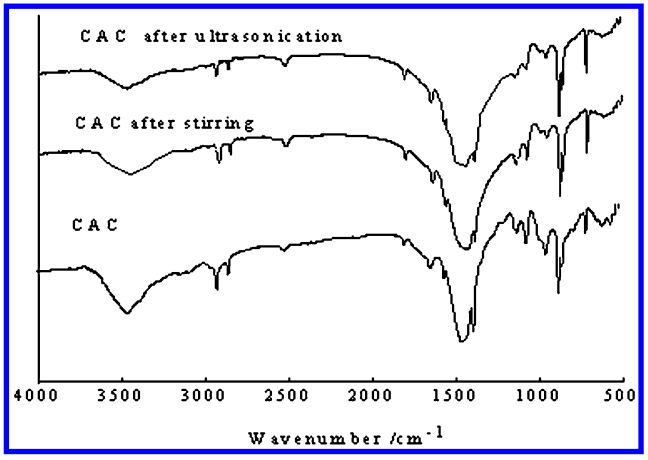

Figure 6. FT-IR spectra of CAC after strring and ultrasonication.

The SEM micrographs of the surface of CAC5, before and after grinding, are shown in Figure 7. The SEM micrograph in Figure 7a shows that CAC5 was initially completely coated with chitosan. Grinding the sample for 10 minutes resulted in the coating being partially shed (Figure 7b). After 20 minutes of grinding, the coating was more noticeably shed (Figure 7c), and after the full 30 minutes of grinding, the coating was almost fully shed (Figure 7d). Although some ionic bonds between $CaCO_3$ and chitosan-adipic acid appear to remain after short amounts of mechanical disruption, it does appear possible to almost completely destroy the coating with prolonged grinding.

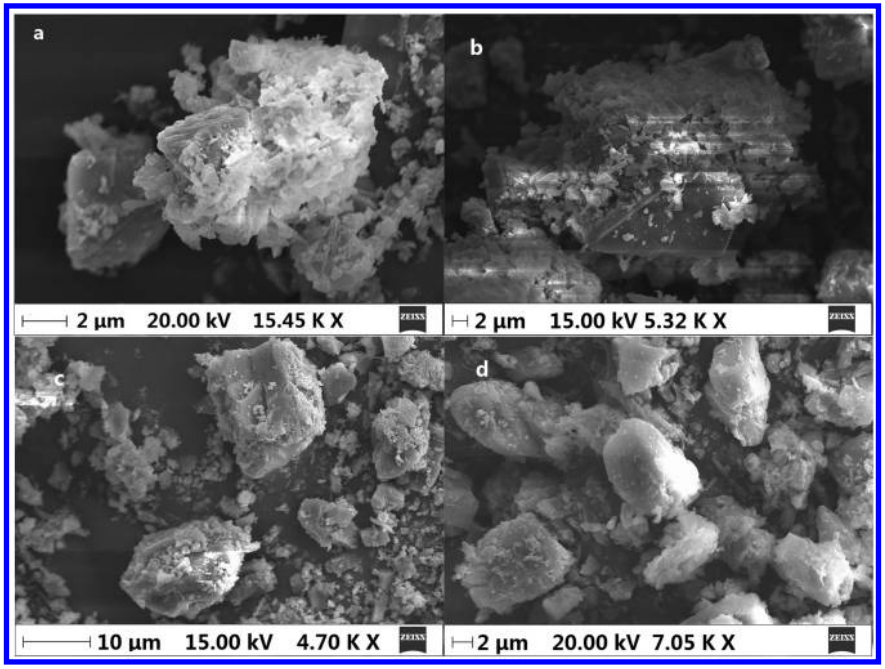

Figure 7. SEM picture of CAC5 after grinding for 0 (a), 10 (b), 20 (c) and 30 (d) minutes.

Antibacterial Properties

Chitosan exhibits antimicrobial activity by causing disruption of cell membranes due to its cationic properties (*36*). The antibacterial activity of different CAC particles and of chitosan alone to *S. aureus* and *E. coli* is shown in Table 3.

The MIC of the chitosan for *S. aureus* and *E. coli* ranged from 20 to 1250 and from 20 to 1000 ppm. The amount of chitosan added to CAC particles was based on the MIC from previous studies. The concentration of chitosan on CAC was not in excess and therefore, excess chitosan was not showing antimicrobial properties.

The starting bacteria concentration was 10^4 CFU/mL. Figure 8 shows the average concentration of *S. aureus* and *E. coli* in the presence of a variety of CAC particles and of chitosan alone after 24 hours. Bacterial concentration lower than $10^{3.5}$ CFU/mL showed that CAC5 killed 90% of the bacteria. The lower the concentration of chitosan in CAC, the poorer the antibacterial ability was.

With increasing concentration of chitosan, the optical density decreased indicating that antibacterial activity increased. The optical density values of CAC4 and CAC5 were relatively close to the optical density value of pure chitosan. This similarity in optical densities is due to the increased amount of chitosan on these particles and may also have been due to the smaller particle size and larger specific surface areas of CAC4 and CAC5. Smaller particle size and larger surface area would increase the chance of CAC interacting with the bacteria. It is notable that the surface of CAC4 and CAC5 particles were

oppositely charged (see Table 1), even though they had similar antibacterial activity. This may be due to the the fact that the antibacterial activity of chitosan is pH sensitive (*37*). To fully display chitosan's antibacterial activity, an acidic medium is necessary (*37*). In addition, chitosan displays poor solubility above pH 6.5 (*38*). At pH 6.5, the pH at which these experiments were conducted, the amino group, NH_2, of CAC would be partially protonated to NH_3^+ by adipic acid causing disruption of the phospholipid layers of bacterial membranes (*36*), even if the overall surface charge of CAC was negative.

Table 3. Average optical density (O.D.) of *S. aureus* and *E. coli* in the presence of a variety of CAC particles and of chitosan alone

Samples	*O.D. (S. aureus)*	*O.D. (E. coli)*
Blank medium	0.245±0.011	0.205±0.014
$CaCO_3$	0.255±0.005	0.215±0.014
CAC1	0.238±0.004	0.193±0.015
CAC2	0.205±0.014	0.168±0.006
CAC3	0.172±0.005	0.113±0.013
CAC4	0.129±0.017	0.105±0.017
CAC5	0.115±0.011	0.093±0.007
Chitosan	0.104±0.008	0.089±0.009

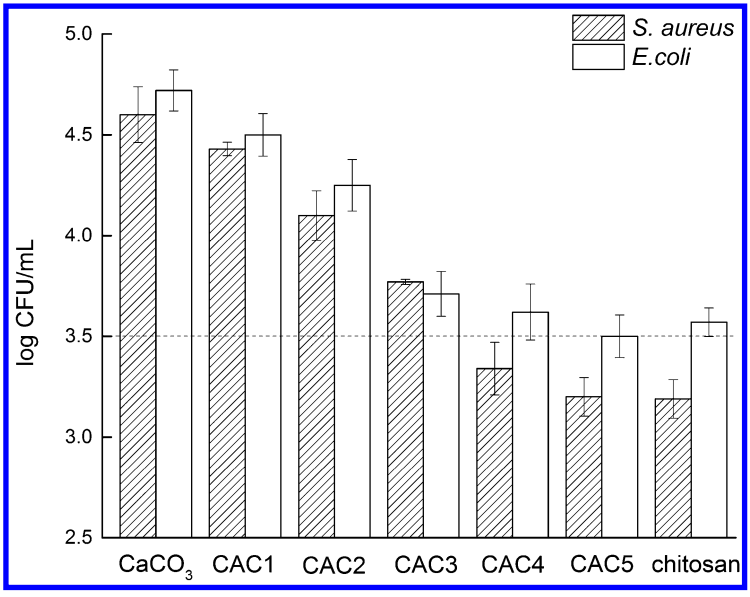

Figure 8. Average concentration of S. aureus and E. coli in the presence of a variety of CAC particles and of chitosan alone after 24 hours.

In The Science and Function of Nanomaterials: From Synthesis to Application; Harper-Leatherman, et al.;

The antibacterial activity of CAC5 particles after destroying the surface is shown in Table 4. After stirring and ultrasonication, the CAC5 coating was reduced slightly and the antibacterial activity is decreased slightly. Under grinding treatment, CAC5 displayed poor antibacterial activity.

Table 4. Average optical density (O.D.) of *S. aureus* and *E. coli* in the presence of a CAC5 particles after surface destruction

Samples	*O.D. (S. aureus)*	*O.D. (E. coli)*
CAC5	0.115±0.011	0.093±0.007
$CaCO_3$	0.255±0.005	0.215±0.014
CAC5 stirring for 50 min	0.118±0.013	0.099±0.017
CAC5 ultrasonic for 50 min	0.135±0.007	0.121±0.008
CAC5 grinding for 10 min	0.211±0.008	0.178±0.004
CAC5 grinding for 20 min	0.239±0.018	0.210±0.015
CAC5 grinding for 30 min	0.245±0.014	0.212±0.018

Conclusion

In this study, $CaCO_3$ double-coated with chitosan-adipic acid (CAC) was developed, the structure was characterized, and the antibacterial activity was measured. The structure analysis shows that chitosan is effectively coated on the surface of $CaCO_3$ through an electrostatic attraction with adipic acid. The FT-IR studies indicated that the 2 site amino group of chitosan reacted with the carboxyl group of adipic acid. The CAC has a core-shell structure and is quite spherical in shape. The result from zeta potential, specific surface area, particle size and contact angle measurements proved that after coating, the particles are smaller in size, higher in specific surface area, and have altered ζ-potential and water contact angle. The double-layer coating was shown to have antibacterial activity against *E. coli* and *S. aureus*. Based on our studies, CAC has potential to be employed as a low-cost chitosan agent and a functional filler.

Acknowledgments

We are grateful for financial support of this research from National Natural Science Foundation of China: Grant No. 51263001

References

1. Saba, N.; Tahir, P.; Jawaid, M. A review on potentiality of nano filler/natural fiber filled polymer hybrid composites. *Polymers* **2014**, *6*, 2247–2273.

2. Rothon, R. N. Mineral Fillers in Thermoplastics: Filler Manufacture and Characterisation. In *Mineral Fillers in Thermoplastics I*; Springer: Berlin, Heidelberg, 1999; pp 67−107.
3. Li, Z.; Gao, Y.; Moon, K.-S.; Tannenbaum, A.; Wong, C. P. Nano Filler Dispersion in Polymer Composites for Electronic Packaging; Electronic Components and Technology Conference (ECTC), 2012 IEEE 62nd, pp 1752−1757, 2012.
4. Bedanokov, A.; Mikitaev, A. K.; Borisov, V.A.; Mikitaev, M.A. *Polymer Nanocomposites: The Current State of the Issue (in Russia)*. **2008**, *26*.
5. Kiehl, J.; Ben-Azzouz, C.; Dentel, D.; Derivaz, M.; Bischoff, J. L.; Delaite, C.; Bistac, S. Grafting process of ethyltrimethoxysilane and polyphosphoric acid on calcium carbonate surface. *Appl. Surf. Sci.* **2013**, *264*, 864–871.
6. Kim, D. S.; Lee, C. K. Surface modification of precipitated calcium carbonate using aqueous fluosilicic acid. *Appl. Surf. Sci.* **2002**, *202*, 15–23.
7. Morel, F.; Bounor-Legaré, V.; Espuche, E.; Persyn, O.; Lacroix, M. Surface modification of calcium carbonate nanofillers by fluoro- and alkyl-alkoxysilane: Consequences on the morphology, thermal stability and gas barrier properties of polyvinylidene fluoride nanocomposites. *Eur. Polym. J.* **2012**, *48*, 919–929.
8. Tran, H. V.; Tran, L. D.; Vu, H. D.; Thai, H. Facile surface modification of nanoprecipitated calcium carbonate by adsorption of sodium stearate in aqueous solution. *Colloids Surf., A* **2010**, *366*, 95–103.
9. Abdolmohammadi, S.; Siyamak, S.; Ibrahim, N. A.; Yunus, W. M.; Rahman, M. Z.; Azizi, S.; Fatehi, A. Enhancement of mechanical and thermal properties of polycaprolactone/chitosan blend by calcium carbonate nanoparticles. *Int. J. Mol. Sci.* **2012**, *13*, 4508–4522.
10. Shi, X.; Bertoti, I.; Pukanszky, B.; Rosa, R.; Lazzeri, A. Structure and surface coverage of water-based stearate coatings on calcium carbonate nanoparticles. *J. Colloid Interface Sci.* **2011**, *362*, 67–73.
11. Novais, V. R.; Júnior, S.; Cézar, P.; Rontani, R. M. P.; Correr-Sobrinho, L.; Soares, C. J. Bond strength between fiber posts and composite resin core: Influence of temperature on silane coupling agents. *Braz. Dent. J.* **2012**, *23*, 8–14.
12. Kohan, M. I.; Mestemacher, S. A.; Pagilagan, R. U.; Redmond, K. Polyamides. In *Ullmann's Encyclopedia of Industrial Chemistry*; Wiley-VCH Verlag: Weinheim, 2000.
13. Wei, D. W.; Sun, W. Y.; Qian, W. P.; Ye, Y. Z.; Ma, X. Y. The synthesis of chitosan-based silver nanoparticles and their antibacterial activity. *Carbohydr. Res.* **2009**, *344*, 2375–2382.
14. Rabea, E. I.; Badawy, M. E.; Stevens, C. V.; Smagghe, G.; Steurbaut, W. Chitosan as antimicrobial agent: Applications and mode of action. *Biomacromolecules* **2003**, *4*, 1457–1465.
15. Qi, L.; Xu, Z.; Jiang, X.; Hu, C.; Zou, X. Preparation and antibacterial activity of chitosan nanoparticles. *Carbohydr. Res.* **2004**, *339*, 2693–2700.

16. Nicu, R.; Lupei, M.; Balan, T.; Bobu, E. Alkyl–chitosan as paper coating material to improve water barrier properties. *Cellul. Chem. Technol.* **2013**, *47*, 623–630.
17. PalDey, S. D.; Deevi, S. C. Single layer and multilayer wear resistant coatings of (Ti, Al) N: A review. *Mater. Sci. Eng., A* **2003**, *342*, 58–79.
18. Zeng, L.; Yang, S.; Zhang, W.; Guo, Y.; Yan, C. Preparation and characterization of a double-layer coating on magnesium alloy AZ91D. *Electrochim. Acta* **2010**, *55*, 3376–3383.
19. Liu, B.; Qiu, S.; Chen, N.; Du, G.; Sun, J. Double-layered silicon nitride antireflection coatings for multicrystalline silicon solar cells. *Mater. Sci. Semicond. Process.* **2013**, *16*, 1014–1021.
20. Du, C.; Shi, J.; Shi, J.; Zhang, L.; Cao, S. PUA/PSS multilayer coated $CaCO_3$ microparticles as smart drug delivery vehicles. *Mater. Sci. Eng., C* **2013**, *33*, 3745–3752.
21. Genovese, D. B.; Lozano, J. E. Particle size determination of food suspensions: Application to cloudy apple juice. *J. Food Process Eng.* **2000**, *23*, 437–452.
22. Vancauwenberghe, V.; Di Marco, P.; Brutina, D. Wetting and evaporation of a sessile drop under an external electrical field: A review. *Colloids Surf., A* **2013**, *432*, 50–56.
23. Kalyani, S.; Krishnaiah, A.; Boddu, V. M. Adsorption of divalent cobalt from aqueous solution onto chitosan–coated perlite beads as biosorbent. *Sep. Sci. Technol.* **2007**, *42*, 2767–2786.
24. Liu, J. H.; Wang, A. Q. Study on superabsorbent composites. XXI. Synthesis, characterization and swelling behaviors of chitosan-g-poly(acrylic acid)/organo-rectorite nanocomposite superabsorbents. *J. Appl. Polym. Sci.* **2008**, *110*, 678–686.
25. Goy, R. C.; de Britto, D.; Assis, O. B. G. A review of the antimicrobial activity of chitosan. *Polímeros* **2009**, *19*, 241–247.
26. Chen, J.; Huang, L.; Lai, H.; Lu, C.; Fang, M.; Zhang, Q.; Luo, X. Methotrexate-loaded pegylated chitosan nanoparticles: Synthesis, characterization, and in vitro and in vivo antitumoral activity. *Mol. Pharmaceutics* **2014**, *11*, 2213–2223.
27. Angadi, S. C.; Manjeshwar, L. S.; Aminabhavi, T. M. Stearic acid-coated chitosan-based interpenetrating polymer network microspheres: Controlled release characteristics. *Ind. Eng. Chem. Res.* **2011**, *50*, 4504–4514.
28. Andersen, F. A.; Brečević, L.; Beuter, G.; Dell'Amico, D. B.; Calderazzo, F.; Bjerrum, N. J.; Underhill, A. E. Infrared spectra of amorphous and crystalline calcium carbonate. *Acta Chem. Scand.* **1991**, *45*, 1018–1024.
29. Lorenzo-Lamosa, M. L.; Remuñán-López, C.; Vila-Jato, J. L.; Alonso, M. J. Design of microencapsulated chitosan microspheres for colonic drug delivery. *J. Controlled Release* **1998**, *52*, 109–118.
30. Orienti, I.; Cerchiara, T.; Luppi, B.; Bigucci, F.; Zuccari, G.; Zecchi, V. Influence of different chitosan salts on the release of sodium diclofenac in colon-specific delivery. *Int. J. Pharm.* **2002**, *238*, 51–59.

31. Li, X.-G.; Lv, Y.; Ma, B.-G.; Wang, W.-Q.; Jian, S.-W. Decomposition kinetic characteristics of calcium carbonate containing organic acids by TGA. *Arabian J. Chem.*DOI:10.1016/j.arabjc.2013.09.026.
32. Wright, S. F.; Dollimore, D.; Dunn, J. G.; Alexander, K. Determination of the vapor pressure curves of adipic acid and triethanolamine using thermogravimetric analysis. *Thermochim. Acta* **2004**, *421*, 25–30.
33. Kalkan, N. A.; Aksoy, S.; Aksoy, E. A.; Hasirci, N. Adsorption of reactive yellow 145 onto chitosan coated magnetite nanoparticles. *J. Appl. Polym. Sci.* **2012**, *124*, 576–584.
34. Kim, B. S.; Kim, C. S.; Lee, K. M. The intracellular uptake ability of chitosan-coated Poly (D,L-lactide-co-glycolide) nanoparticles. *Arch. Pharmacal Res.* **2008**, *31*, 1050–1054.
35. Atakan, A.; Atalay-Oral, C.; Tatlier, M.; Erciyes, T.; Erdem-Senatalar, A. Post-synthesis treatment for improving zeolite coating stability. *Microporous Mesoporous Mater.* **2012**, *156*, 262–269.
36. Pavinatto, F. J.; Pavinatto, A.; Caseli, L.; Santos, D. S., Jr.; Nobre, T. M.; Zaniquelli, M. E.; Oliveira, O. N., Jr. Interaction of chitosan with cell membrane models at the air-water interface. *Biomacromolecules* **2007**, *8*, 1633–1640.
37. Fujimoto, T.; Tsuchiya, Y.; Terao, M.; Nakamura, K.; Yamamoto, M. Antibacterial effects of chitosan solution against *Legionella pneumophila*, *Escherichia coli*, and *Staphylococcus aureus*. *Int. J. Food Microbiol.* **2006**, *112*, 96–101.
38. Li, Z.; Zhuang, X. P.; Liu, X. F.; Guan, Y. L.; De Yao, K. Study on antibacterial O-carboxymethylated chitosan/cellulose blend film from LiCl/N, N-dimethylacetamide solution. *Polymer* **2002**, *43*, 1541–1547.

Chapter 8

Electrospun Silica Nanofiber Mats

Effects of Sol Viscosity and Application to Thin Layer Chromatography

Abigail Freyer* and Nancy Ortins Savage

Department of Chemistry and Chemical Engineering, University of New Haven, 300 Boston Post Road, West Haven, Connecticut 06516, United States
***E-mail: afreyer@UR.Rochester.edu**

Electrospun nanofiber mats were prepared from low-viscosity sol-gel silica without the addition of a carrier polymer. Silica sols synthesized from tetraethyl orthosilicate (TEOS) under acidic conditions were electrospun into nanofibers in the viscosity range of 2 to 4 mPa·s. The influence of ethanol and water concentrations on the viscosity of as-synthesized and aged silica sols was also determined. Nanofibers produced from as-synthesized sols with a TEOS:H_2O ratio of 1:2 ranged in diameter from 50 nm to 200 nm. Increases in viscosity, whether due to aging or increased water concentration in the sol resulted in fragmented nanofibers. Nanofiber mats used as the stationary phase for thin layer chromatography (TLC) were able to separate components of a test dye mixture.

Introduction

Over the last twenty years electrospinning has become an important technique in preparing both organic and inorganic materials with nanofiber morphologies (*1–5*). In electrospinning a viscous solution is ejected through an orifice, such as a syringe needle, under an applied electric field. Initially, charge collects on the hemispherical droplets that form at the tip of an orifice. As the charge increases, the drop elongates to a conical shape called the Taylor cone (*4*). Eventually, the

In The Science and Function of Nanomaterials: From Synthesis to Application; Harper-Leatherman, et al.;

electrostatic force overcomes the surface tension of the liquid solution and liquid jets emerge from the Taylor cone, whipping through the air before depositing on a grounded collector plate as a solid non-woven mat of nanofibers as the solvent dries. The magnitude of the applied voltage and distance between the syringe tip and collector plate are parameters of the apparatus that can be varied to affect nanofiber morphology (*6–9*). In addition, properties of the electrospinning precursor solution, such as viscosity, carrier polymer and solvent-type, can impact the final structure of fibers. Common morphological changes include variations to nanofiber dimensions (length and diameter) and nanofiber mat density as well as the formation of hollow nanofibers (*6–9*). Porous and textured nanofibers as well as beaded nanofibers can be produced by incorporating particles in the electrospinning solution (*3*, *10–12*) or varying the electrospinning solution viscosity (*9*, *13*). In addition, specially designed collector plate electrodes (*2*) and rotating collector drums (*14*) can be used to prepare oriented nanofiber mats. Electrospun fibers have found application in a number of fields, from catalysis (*15–18*), chemical sensing (*16*, *19*), separations (*14*, *20–24*) to biomaterials (*6*, *10*, *25*, *26*). In each case, the morphology of the electrospun fibers have played an important role in the material's ultimate utility in its application.

Silica is among the many materials that have been prepared as nanofibers by the electrospinning technique (*6*, *7*, *10*, *27*). Most syntheses of electrospun silica nanofibers begin with the preparation of sol-gel silica from tetraethyl ortho silicate (TEOS) (*6*, *7*, *10*, *27*). The sol-gel process is a wet-chemical synthesis technique for preparing gels, often starting with metal alkoxides that undergo hydrolysis and condensation polymerization reactions to give oxide gels (*27*, *28*). Typical sol compositions used to make polymeric gels consist of TEOS, ethanol, water and an acid or base catalyst. The hydrolysis reaction is slow under acidic conditions, leading to linear molecules with some branching and crosslinking. The eventual result is a gel of entangled polymeric chains. When the synthesis is conducted with a basic catalyst, the hydrolysis reaction is fast and shorter, highly-branched silica particles form. A prepared silica sol is then mixed with a carrier polymer such as polyvinyl alcohol (PVA), polyvinyl pyrrolidone (PVP) or polyethylene oxide (PEO) before being electrospun. TEOS concentration, polymer identity and concentration, solution viscosity and post-electrospinning heat treatments all play a role in the morphology and other properties of the electrospun silica nanofibers (*6*, *10*). Porous and surface roughened silica fibers are possible through the inclusion of silica nanoparticles, in addition to the TEOS-based sol, to the electrospining solution (*10*). Alternatively, monodisperse solutions of silica particles can be electrospun in the presence of a carrier polymer and thereby assemble into high-surface-area fibers (*11*). Other groups have prepared hollow silica fibers by adding TEOS to ethanolic PVP solutions and carefully controlling the TEOS:ethanol ratio (*7*, *8*).

Because carrier polymers are used in the electrospinning process, a pyrolysis step to decompose the added polymer, is necessary to obtain pure silica fibers. This pyrolysis step requires high temperature, which is not attractive for all applications. In 2003, Choi et al. demonstrated that silica could be electrospun without the addition of a carrier polymer (*27*). Further work by Iimura, et al. demonstrated that the TEOS:water ratio was crucial in these carrier polymer-free films; if it was

too high the sols were too viscous for the electrospinning process (*29*). In both works, an acidic catalyst was used during sol synthesis because it promoted the formation of linearized silica chains which Choi et al. contend is advantageous for electrospinning (*27*).

The potential applications of electrospun silica nanofibers are numerous. Recent investigations have explored the suitability of electrospun silica nanofibers, as an alternative to glass beads, for reinforcing dental composites (*6*, *10*, *25*). The amorphous structure of SiO_2, coupled with the fibrous morphology, provide dental resins with improved mechanical strength (*25*). In the field of catalysis, electrospun silica nanofibers are used as a catalyst support, providing a high surface area on which the catalyst can be effectively dispersed. Zinc oxide quantum dots on electrospun silica nanofiber mats are effective photocatalysts (*15*). Silver (*16*, *17*) and gold (*18*) catalysts on electrospun silica nanofibers are thermally stable and active for various catalytic reduction reactions. The high surface area of electrospun nanosilica mats also makes them promising as membranes for the adsorption of toxic contaminants (*30*). Electrospun silica nanofibers have also been investigated for sensing applications. Yoon et al. exploited the solvatochromic behavior of polydiacetylenes to make "litmus-type" membranes composed of electrospun silica and the polymer for the detection of volatile organic compounds (*19*). Silica fibers electrospun with the addition of horseradish peroxidase show potential for biosensing applications (*16*). Finally, electrospun silica has been explored as a biocompatible scaffold for cell adhesion and growth (*26*). The material is attractive for its properties; cells adhere to it, it is stable in a biosystem, and it has high surface area and porosity.

A number of researchers have begun to investigate the use of electrospun fibers in chromatographic applications, such as solid phase microextraction (SPME) and TLC. For SPME applications, electrospun coatings can be formed directly on the extraction fibers. Incorporation of silica nanoparticles in electrospun polyamide nanofibers used as a SPME coating helped to increase the surface area of the polymer (*20*). Electrospun polyetherimide fibers (*21*) and carbon nanofibers formed from the decompostion of photoresist (*22*) were effective in the extraction of organics from the headspace of aqueous solutions. They were also stable at elevated gas chromatography inlet temperatures (*21*, *22*).

In 2009, Olesik and coworkers began to explore electrospun nanofibers as stationary phase materials in ultrathin layer chromatography (*23*). Working primarily with polyacrylonitrile (PAN), they demonstrated that these electrospun stationary phases have faster analysis times and efficiencies 10 times higher than commercial TLC plates. When the electrospun fibers are aligned, by collecting fibers on a rotating drum (*14*), the performance of the electrospun plate improves further, with efficiencies 100 times greater then the unaligned PAN stationary phase and faster separations. Furthermore, the R_f values were more consistent (lower % relative standard deviation) for aligned vs. non-aligned electrospun TLC plates (*14*). Other researchers have continued to explore this material's preparation route for stationary phases, incorporating additives in PAN films to create TLC plates with photoluminescent detection (*24*).

Most TLC plates are made with stationary phases of alumina, cellulose or silica but, despite the ubiquity of these materials, their electrospun preparations

have not yet been pursued for TLC applications. Other investigators may have chosen to study electrospun stationary phases composed of organic polymers rather than materials like silica in an effort to minimize the number of processing variables to study. Optimization of electrospinning for TLC requires the investigation of numerous parameters, such as solution viscosity and applied voltage (*6–8*). Electrospinning TLC stationary phase from solutions prepared by the sol-gel process adds a layer of complexity due to the additional variables (such as humidity or reactant concentration) of the synthetic process.

This work demonstrates that it is possible to electrospin low-viscosity silica sols without the use of carrier polymers. The effects of sol aging and ethanol and water concentrations on the final morphology of the nanofibers is also presented. Finally, the electrospun silica fiber mats are examined as a potential stationary phase in thin layer chromatography.

Experimental Section

Silica precursor solutions were prepared by the hydrolysis of tetraethyl orthosilicate (TEOS) with a method adapted from Choi et al. (*27*) The TEOS (99+%) was obtained from Alfa Aesar. All other reagants were obtained from Fisher Scientific and used as received, with the exception of hydrochloric acid which was diluted into deionized water to form a 1 M solution. Under nitrogen, TEOS was dissolved in ethanol. Hydrochloric acid solution and water were then added dropwise while the solution was stirred. The solution was then stirred at 80 °C for 30 minutes under nitrogen. Five milliliters of five different solutions were prepared; the molar ratios of the reagants are summarized in Table 1. Each solution was aged for four weeks, prior to electrospinning.

The viscosity of each solution was measured immediately after synthesis and after aging for between 1 and 4 weeks. The viscosity measurements were made with an Ostwald viscometer that was calibrated with ethanol. Flow times of the silica solutions between the fiducial marks were measured, then converted to viscosities using a simplified form Pouiselle's equation $\eta=\kappa\rho t$, where η = viscosity, κ = a constant representing the physical dimensions of the viscometer, ρ = solution density and t =time) (*31*). Each measurement was made in triplicate. Solution densities were measured by determining the mass of silica solution that filed a 1.00 mL volumetric flask. The pH of each solution, as synthesized, and after aging was measured with colorpHast pH indicator strips from EMD Chemicals, Inc. Sol pH's were between 2.0 and 2.5, regardless of aging time.

A schematic diagram of the electrospinning apparatus is shown in Figure 1. Solutions were dispensed from 1 mL disposable syringes with 22G blunt tip needles using a syringe pump (Cole Parmer #78-0100C, Vernon Hills, IL). A voltage between 5 and 15 kV was supplied by a high voltage power supply (Gamma Applied Research High Voltage, ES30P-5W/DAM, Ormond Beach, FL). The tip to collector distance was held constant at 10 cm. The environmental humidity was not controlled during the electrospinning, but was monitored with a digital barometer. Humidity fell between ~20% and 40% for all samples. Solutions were electrospun onto polished silicon chip specimen supports (for

In The Science and Function of Nanomaterials: From Synthesis to Application; Harper-Leatherman, et al.;

scanning electron microscopy measurements, from Ted Pella) and aluminum foil-wrapped microscope slides (for thin later chromatography). Scanning Electron Microscopy (SEM) was done with a Hitachi SU-70 SEM.

Table 1. Molar ratios of reagants used in synthesis of silica precursor solutions

Method	*TEOS*	*Ethanol*	*Water*	*HCl*
1	1	2	2	0.01
2	1	2	1	0.01
3	1	1	1	0.01
4	1	3	2	0.01
5	1	3	3	0.01

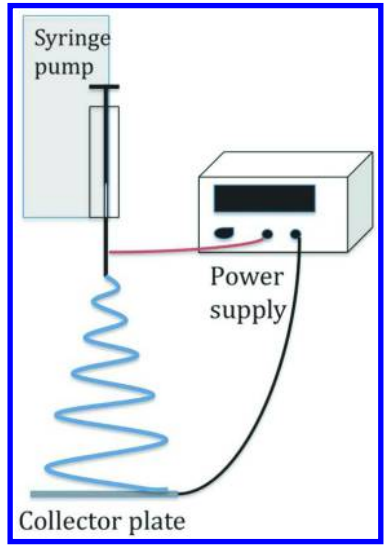

Figure 1. Schematic of the apparatus used for electrospinning.

For chromatography, silica was electrospun onto aluminum foil-wrapped microscope slides at a potential of 10 kV and flow rate of 0.01 mL/hr for between 1 and 4 hours. Collection of nanofiber mats on the silicon chip supports was conducted simultaneously by mounting the supports adjacent to the foil-wrapped slides on the collector plate. The slides were then allowed to dry at room temperature or in a 200 °C oven for four hours. The electrospun, silica-coated, aluminum foil-wrapped glass slides were used as TLC plates to separate the components of two test dye mixtures (Analtech). Test dye 1 (Catalog #30-01),

was comprised of Sudan IV, Bismark Brown Y, Rhodamine B and Fast Green FCF. Test dye mixture 2 (Catalog # 30-02) contained Rhodamine 6G, Orange II and Fast Green FCF. Dyes were spotted onto plates using a capillary and developed in a standard, screw-top jar using the mobile phase 60:10:10 ethyl acetate:methanol:water. Retention factors (R_f) were calculated by dividing the distance traveled by the dye spot by the distance traveled by the mobile phase up the TLC plate. Commercial TLC plates (Whatman Flexible Plates for TLC, 250 micron layer silica gel on polyester backing) were used for comparative measurements.

Results and Discussion

The viscosity of each silica sol solution prepared was measured immediately following synthesis and after 1, 2, 3 and 4 weeks of aging. The data are summarized in Table 2. The amount of water in the synthesis had the most pronounced effect on the viscosity of the solutions. As the TEOS:H_2O molar ratio increased from 1:1 to 1:2 to 1:3, the as-synthesized viscosity of the sol increased as well. Furthermore, the viscosity of the aged samples increased most dramatically for samples with more water, as summarized in Table 1. For example, the Method 5 sample, which has 3 times as much water as TEOS (by mole) had a viscosity greater than 14 mPa·s after 2 weeks of aging, which is beyond the measuring capacity of the viscometer. For samples with TEOS:H_2O ratios of 1:1 (Method 2 and 3), there was no significant change in the viscosity after aging. Changes in TEOS:ethanol molar ratio did not have a significant impact on the sol viscosities. There are no significant differences in the viscosities of the samples, when measured immediately following synthesis, if comparing samples prepared by Methods 1 and 4 or comparing Methods 2 and 3, which have the same TEOS:H_2O ratio but varied molar ratios of TEOS:ethanol. Additionally, similar aging profiles were found for the pairs when comparing Methods 1 and 4 (increasing viscosity over time) and for Methods 2 and 3 (relatively stable viscosity over time). Holowacz et al. followed the viscosity of silica sols as a function of ethanol content and found that increased ethanol led to a decrease in sol viscosity (*28*). However, they followed viscosity changes from a 1:5 (h = 1.926 mPa·s) to 1:50 (1.634 mPa·s) TEOS:ethanol ratio. Given the small change in viscosity over a larger change in sol concentration in this past study, it is reasonable that we did not observe a measurable viscosity change as the TEOS:ethanol changed from 1:1 to 1:3 (*28*). In six replicate syntheses of silica sols following Method 1, the solution viscosity ranged from 2.45 mPa·s to 2.96 mPa·s, when measured immediately following synthesis.

Attempts to electrospin each solution were made immediately after synthesis and after 1, 2, 3 and 4 weeks of aging. For each solution, the electrospinning conditions were adjusted (0.01-0.1 mL/hr flow rate, 5-15 kV applied voltage) until fiber formation was observed. Electrospun fibers were only produced from a subset of the solutions prepared. The solutions that produced fibers have their viscosity values shown in bold in Table 2. Fibers were generally produced from solutions with viscosities in the range of 2 to 4 mPa·s. The exceptions were the

In The Science and Function of Nanomaterials: From Synthesis to Application; Harper-Leatherman, et al.;

aged solutions prepared by Method 4. This solution has a higher ethanol content as compared to the Method 1 solution. Differences in the evaporation rates of solvent during the electrospinning process may be a contributing factor to the lack of fiber formation for these Method 4 samples.

Table 2. Viscosities of electrospun silica precursor solutions. Data is reported as the average of three replicate measurements (+/- standard deviation) in units of mPa·s. Bold values indicate that sample was successfully electrospun.

Week	*Method 1*	*Method 2*	*Method 3*	*Method 4*	*Method 5*
0	**2.45 (±0.05)**	1.78 (±0.04)	1.87 (±0.04)	**2.34 (±0.05)**	**3.67±0.07**
1	**2.66 (±0.05)**	1.74 (±0.04)	1.81(±0.04)	**2.71 (±0.05)**	5.85±0.12
2	**3.18 (±0.07)**	1.66 (±0.03)	1.78 (±0.04)	2.83 (±0.06)	14.4±0.32
3	**3.40 (±0.07)**	1.76 (±0.04)	1.81 (±0.04)	3.44 (±0.07)	---------
4	4.31 (±0.09)	1.60 (±0.03)	1.79 (±0.04)	3.94 (±0.08)	----------

SEM was used to characterize the fiber mats produced. As shown in Figure 2, the fibers produced from solutions 1 and 4, which both have a TEOS:H_2O ratio of 1:2 and and similar viscosities, produce fibers of similar quality. The fibers produced from Method 1 range in diameter from 50 nm to 200 nm, while fibers produced from Method 4 range from 100 nm to 300 nm in diameter. Fibers produced from solution 5, which has a TEOS:H_2O ratio of 1:3 and higher viscosity, are between 75 nm and 250 nm and appear fragmented.

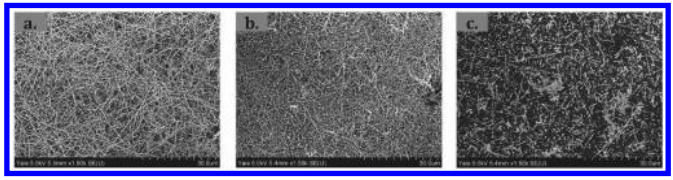

Figure 2. SEM images of electrospun silica mats prepared with different TEOS:H_2O ratios. a.) Method 1, 15 kV, 0.02 mL/hour. b.) Method 4, 15 kV, 0.02 mL/hr c.) Method 5, 10 kV, 0.03 mL/hr.

Figure 3 presents SEM images of Method 1 nanofiber mats when electrospun immediately after synthesis and with 1, 2 and 3 weeks of aging. As the solution was aged for longer periods of time, the fibers produced were increasingly fragmented and there was a higher density of drops. The images of the electrospun fibers produced by Method 1 after three weeks of aging are similar in appearance to the morphology of fibers obtained from Method 5 immediately following synthesis (Figure 3d vs. Figure 2c). This is attributed to the similarities of the viscosities of the two samples and indicates that the solution viscosity plays an important role in fiber morphology.

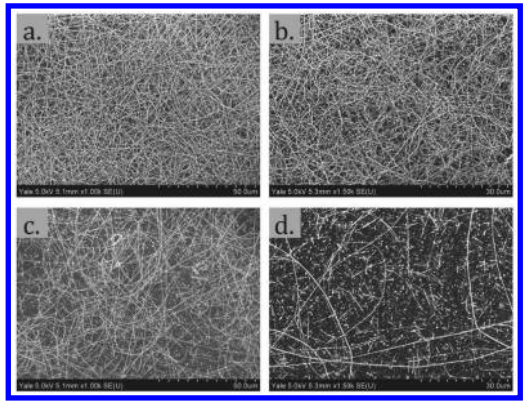

Figure 3. SEM images of electrospun silica mats prepared by Method 1, with electrospinning conditions. a.) as-synthesized, 10 kV, 0.01 mL/hr b.) 1 week of aging, 15 kV, 0.02 mL/hr c.) 2 weeks of aging,7 kV, 0.02 mL/hr d.) 3 weeks of aging, 8 kV, 0.02 mL/hr.

Our results indicate that the optimal viscosity for electrospinning polymer-free silica is in the range of 2 to 4 mPa·s. This is significantly lower that the optimal viscosity range (200-800 mPa·s) for electrospinning reported (*29*) for carrier-polymer-free silica sols. This is also different than the optimal electrospinning viscosity range reported for polymeric solutions. Deitzel et al. report that electrospinning occurs at viscosities between 100 mPa·s and 2000 mPa·s, with a higher likelihood of observing mixtures of fibers and droplets at the lower end of that range for solutions of PEO (*9*). This is echoed somewhat by the Reneker group, which illustrated that beaded nanofibers of PEO were obtained by electrospinning at low viscosity (~13-300 mPa·s), while fibers were prevelant at higher viscosities (up to 1800 mPa·s) (*13*). These investigators attribute the propensity for low viscosity solutions to electrospray, forming droplets, rather than electrospin, forming nanofibers, to the competition between a solution's surface tension and the viscoelastic force (*9*, *13*, *29*). While lower viscosity (and higher surface tension) solutions will typically form droplets, these are not the only two properties involved. It is also demonstrated that a high net charge density on the liquid emerging from the orifice will favor fiber formation, as the electrostatic charge on the liquid surface can overcome the surface tension. It is our belief that, at the slow flow rates used in our study to dispense liquid from the syringe needle (on the order of mL/hr), charge accumulates on the emerging liquid and the net charge becomes high enough to promote fiber formation even at low viscosity. It is also likely that the sol condensation reaction, the route to polymerization of the silica, is continuing as the solution emerges from the syringe needle. Further condensation of the silica sol will increase its viscosity and make it more likely to form nanofibers during the electrospinning.

Using sythesis Method 1, electrospun films were prepared on foil-wrapped glass slides and used as TLC plates. Table 3 summarizes the R_f values obtained for three different plates prepared with electrospinning compared to those

obtained with a commercially available TLC plate. All three electrospun silica plates were largely successful in separating the components of the dye mixture but there are notable differences in the separations that occurred on both plates. First, the electrospun silica did a poorer job in separating the dye molecules in dye mixture 1. The R_f values for Rhodamine B and Bismark Brown are high, and there is no spot observed for Sudan(IV). The separation is better for dye mixture 2, though both Orange II and Rhodamine 6G have higher R_f values on the electrospun silica plates as compared to the commercial plate. Because the R_f values for the faster moving dyes are much larger on the electrospun silica plate as compared to the commercial plate, it is likely that the missing dye, Sudan (IV), is simply unresolved and that the interactions between the stationary phase and dye molecules are not sufficient for full separation.

Table 3. Comparison of retention factors of dye molecules when separated on commercial thin layer chromatography plates and electrospun silica plates

	Commercial Plate	*Electrospun Silica*		
Preparation Conditions	*N/A*	*1 h*	*2 h*	*4 h*
Dye Mixture 30-01				
Fast Green FCF	0.01	0.12	0.01	0.08
Rhodamine B	0.18	0.79	0.87	0.90
Bismark Brown	0.23	0.71	0.80	0.84
Sudan (IV)	0.76	--	--	--
Dye Mixture 30-02				
Fast Green FCF (Dye 2)	0.01	0.01	0.03	0.09
Orange II	0.38	0.71	0.85	0.84
Rhodamine 6G	0.47	0.83	0.92	0.91

Additionally, there appears to be significant band broadening with the electrospun silica plates. Figure 4 shows an optical image of an electrospun thin layer chromatography plate (4 hour deposition, 4 hour heating at 200 °C) after the separations were completed. Band broadening is a normal occurance in separations, but is more pronounced on these electrospun stationary phases as compared to commercial silica plates. There are two possible reasons for the observed band broadening. Longitudinal diffusion, in which molecules diffuse from areas of high concentration to areas of low concentration definitely plays a role in the band broadening. As shown in Figure 3, the electrospun silica films have a low density per unit area, so the dye molecules may diffuse to a greater extent while in the mobile phase in between adsorption events on the stationary phase, as compared to commercial plates composed of close packed silica particles. Beilke et al. reports that low nanofiber mat density (as determined

in their work by mass differences of mats with the same thickness) results in band broadening and overall poor chromatographic performance (*14*). Another possible explanation is that the dye molecules follow the trajectory of the electrospun fibers as they adsorb and desorb from the silica during the separation. This potential band broadening mechanism is illustrated in Figure 5. As different fibers follow different trajectories, dye molecules that are initially adsorbed on neighboring, but distinct fibers will be much further apart at the end of the separation.

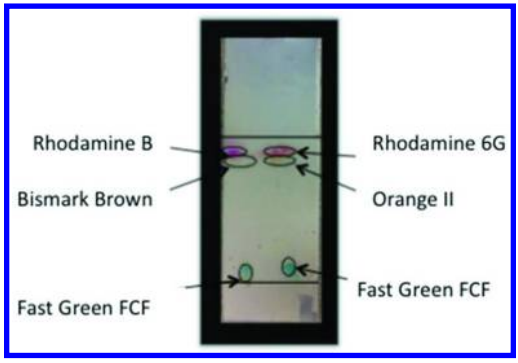

Figure 4. Optical image of electrospun silica thin layer chromatography plate after separation. Dye Mixture 1 is on the left and Dye Mixture 2 is on the right.

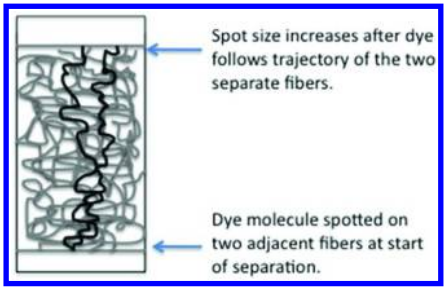

Figure 5. Illustration of proposed mechanism for band broadening in electrospun TLC.

Optimization of electrospun silica films, through modifications of electrospinning parameters, sol and electrospinning solution properties and post-electrospinning treatment, will lead to improved separations and decreased band-broadening. Preparation of aligned, electrospun TLC plates as well as electrospun TLC plates that include indicators to enhance the visualization of spots, will further improve this technology.

Conclusions

This work has demonstrated that silica sols can be electrospun from carrier-polymer-free solutions with viscosities well-below those reported in the literature. Furthermore, the fibers hold potential as stationary phase material for thin layer chromatography. Future studies will focus on reliably reproducing mats by control of the humidity during the electrospinning process. Additionally, processing parameters will be modified to optimize the electrospun silica mats for chromatographic applications, with the goal of preparing dense, uniform, electrospun nanofiber mats that separate mixtures with speed, with good resolution and with little band broadening.

Acknowledgments

Facilities use was supported by YINQE and NSF MRSEC DMR 1119826. A.F. would like to thank the University of New Haven Summer Undergraduate Research Program and the University of New Haven Honor's program for funding.

References

1. Li, D.; Xia, Y. *Adv. Mater.* **2004**, *16*, 1151–1170.
2. Li, D.; Wang, Y.; Xia, Y. *Nano Lett.* **2003**, *8*, 1167–1171.
3. Wessel, C.; Ostermann, R.; Dersch, R.; Smarsly, B. M. *J. Phys. Chem. C* **2011**, *115*, 362–372.
4. Doshi, J.; Reneker, D. H. *J. Electrost.* **1995**, *35*, 151–160.
5. Greiner, A.; Wendorff, J. H. *Angew. Chem., Int. Ed.* **2007**, *46*, 5670–5703.
6. Liu, Y.; Sagi, S.; Chandrasekar, R.; Zhang, L.; Hedin, N. E.; Fong, H. *J. Nanosci. Nanotechnol.* **2008**, *8*, 1528–1536.
7. An, G.-H.; Jeong, S.-Y.; Seong, T.-Y.; Ahn, H.-J. *Mater. Lett.* **2011**, *65*, 2377–2380.
8. Li, X. H.; Shao, C. L.; Liu, Y. C. *Langmuir* **2007**, *23*, 10920–10923.
9. Deitzel, J. M.; Kleinmeyer, J.; Harris, D.; Beck Tan, N. C. *Polymer* **2001**, *42*, 261–272.
10. Wen, S.; Liu, L.; Zhang, L.; Chen, Q.; Zhang, L.; Fong, H. *Mater. Lett.* **2010**, *64*, 1517–1520.
11. Kanehata, M.; Ding, B.; Shiraori, S. *Nanotechnology* **2007**, *18*, 315602–315609.
12. Casper, C. L.; Stephens, J. S.; Tassi, N. G.; Chase, B.; Rabolt, J. F. *Macromolec.* **2004**, *37*, 573–578.
13. Fong, H.; Chun, I.; Reneker, D. H. *Polymer* **1999**, *40*, 4585–4592.
14. Beilke, M. C.; Zewe, J. W.; Clark, J. E.; Olesik, S. V. *Anal. Chim. Acta* **2013**, *761*, 201–208.
15. Zhang, X.; Shao, C.; Zhang, Z.; Li, J.; Zhang, P.; Zhang, M.; Mu, J.; Guo, Z.; Liang, P.; Liu, Y. *ACS Appl. Mater. Interfaces* **2012**, *4*, 785–790.
16. Patel, A. C.; Li, S.; Wang, C.; Zhang, W.; Wei, Y. *Chem. Mater.* **2007**, *19*, 1231–1238.

17. Zhang, Z.; Shao, C.; Sun, Y.; Mu, J.; Zhang, M.; Zhang, P.; Guo, Z.; Lian, P.; Wang, C.; Liu, Y. *J. Mater. Chem.* **2012**, *22*, 1387–1395.
18. Zhang, Z.; Shao, C.; Zou, P.; Zhang, P.; Zhang, M.; Mu, J.; Guo, Z.; Li, X.; Wang, C.; Liu, Y. *Chem. Commun.* **2011**, *47*, 3906–3908.
19. Yoon, J.; Chae, S. K.; Kim, J.-M. *J. Am. Chem. Soc.* **2007**, *129*, 3038–3039.
20. Bagheri, H.; Roostaie, A. *J. Chromatogr. A* **2013**, *1324*, 11–20.
21. Bagheri, H.; Akbarinejad, A.; Aghakhani, A. *Anal. Bioanal. Chem.* **2014**, *406*, 2141–2149.
22. Zewe, J. W.; Steach, J. K.; Olesik, S. V. *Anal. Chem.* **2010**, *82*, 5341–5348.
23. Clark, J. E.; Olesik, S. V. *Anal. Chem.* **2009**, *81*, 4121–4129.
24. Kampalanonwat, P.; Supaphol, P.; Murlock, G. E. *J. Chromatogr. A* **2013**, *1299*, 110–117.
25. Gao, Y.; Sagi, S.; Zhang, L.; Liao, Y.; Cowles, D.; Sun, Y.; Fong, H. *J. Appl. Polym. Sci.* **2008**, *110*, 2063–2070.
26. Yamaguchi, T.; Sakai, S.; Watanabe, R.; Tarao, T.; Kawakami, K. *J. Biosci. Bioeng.* **2010**, *109*, 304–306.
27. Choi, S.-S.; Lee, S. G.; Im, S. S.; Kim, S. H.; Joo, Y. L. *J. Mater. Sci. Lett.* **2003**, *22*, 891–893.
28. Holowacz, I.; Podbielska, H.; Bauer, J.; Ulatowska-Jarza, A. *Opt. Appl.* **2005**, *35*, 691–699.
29. Iimura, K.; Oi, T.; Suzuki, M.; Hirota, M. *Adv. Powder Technol.* **2010**, *21*, 64–68.
30. Wu, Y.; Li, F.; Wu, Y.; Jia, W.; Hannam, P.; Qiao, J.; Li, G. *Colloids Polym. Sci.* **2011**, *289*, 1253–1260.
31. Halpern, A. M.; McBane, G. C. *Experimental Physical Chemistry*, 3rd ed.; W.H. Freeman and Company: New York, 2006; p 17-5.

Subject Index

In The Science and Function of Nanomaterials: From Synthesis to Application; Harper-Leatherman, et al.;

In The Science and Function of Nanomaterials: From Synthesis to Application; Harper-Leatherman, et al.;

P

R

S

U

V